d'Collection

공학박사학위논문

SYNTHESIS AND APPLICATION OF INORGANIC FUNCTIONAL ADSORBENTS AND POLYMER COMPOSITES FOR ANIONIC CONTAMINANT REMOVAL FROM WATER

수중 음이온 오염물질 제거를 위한
기능성 무기소재 및 고분자 복합체의
합성과 적용

2017년 2월

서울대학교 대학원

생태조경·지역시스템공학부

지역시스템공학전공

김　재　현

SYNTHESIS AND APPLICATION OF INORGANIC FUNCTIONAL ADSORBENTS AND POLYMER COMPOSITES FOR ANIONIC CONTAMINANT REMOVAL FROM WATER

수중 음이온 오염물질 제거를 위한 기능성 무기소재 및 고분자 복합체의 합성과 적용

지도교수 김 성 배

이 논문을 공학박사 학위논문으로 제출함

2016년 12월

서울대학교 대학원
생태조경·지역시스템공학부 지역시스템공학전공

김 재 현

김재현의 공학박사 학위논문을 인준함

2017년 1월

위 원 장 _____이 인 복_____ (인)

부위원장 _____김 성 배_____ (인)

위   원 _____박 성 직_____ (인)

위   원 _____최 재 우_____ (인)

위   원 _____송 인 홍_____ (인)

I certify that I have read this dissertation and that in my opinion it is fully adequate, in scope and quality, as dissertation for the degree of Doctor of Philosophy.

In-Bok Lee

Chairman

I certify that I have read this dissertation and that in my opinion it is fully adequate, in scope and quality, as dissertation for the degree of Doctor of Philosophy.

Song Bai Li

Vice-Chairman

I certify that I have read this dissertation and that in my opinion it is fully adequate, in scope and quality, as dissertation for the degree of Doctor of Philosophy.

Seong-Jik Park

I certify that I have read this dissertation and that in my opinion it is fully adequate, in scope and quality, as dissertation for the degree of Doctor of Philosophy.

Jae-Woo Choi

I certify that I have read this dissertation and that in my opinion it is fully adequate, in scope and quality, as dissertation for the degree of Doctor of Philosophy.

Inhong SONG

ABSTRACT

This thesis deals with the synthesis, characterization, and application of an inorganic functional materials as adsorbents for phosphorous, chromium, and fluorine removal from aqueous solutions. The inorganic functional materials presented in this study include iron oxide nanoparticle-chitosan composite, triamine-functionalized mesoporous silica-polymer composite, calcined Mg-Fe layered double hydroxide-PVDF/PVA composite, and quintinite.

Iron oxide nanoparticle(ION)-chitosan composites were prepared using acidified chitosan, an environmentally friendly polymer, suspension to blend iron oxide nanoparticles by a cross-linking method. The removal of phosphate by ION-chitosan composites was verified by batch experiments, column experiments and pilot-scale adsorption tower experiment. The adsorption properties were analyzed and quantified using kinetic and equilibrium models and thermodynamic analysis. ION-chitosan composites successfully removed phosphate from aqueous solution and showed good reversibility, multicycle stability. It is a good candidate for environmentally friendly inorganic composites as adsorbents.

The characterization of triamine-functionalized mesoporous silica-polymer composites for Cr(VI) removal was also studied. The mesoporous material with various amounts of functional group had high surface area. The kinetics of the functionalized mesoporous silica were found to be sufficiently fast and it was observed that maximum sorption capacity was 330.88 mg/g. The composites showed good performance of chromate removal from real industrial wastewater.

The calcined Mg-Fe layered double hydroxide(LDH) was prepared through a co-precipitation and calcination at 300 ^{o}C. The calcined LDH could be used repeatedly for phosphate removal through desorption with 0.1 M NaOH solution. MgFe calcined LDH-PVDF/PVA composites also could be used for phosphate removal from aqueous solutions with regeneration and repeated use. The phosphate removal was relatively constant at an acidic and alkaline pHs.

Quintinite was applied as adsorbents for removal of phosphate and fluoride. The maximum phosphate adsorption capacity was 4.77 mgP/g. The phosphate adsorption to quintinite was not varied at pH 3.0 – 7.1 (1.50 –1.55 mgP/g) but decreased considerably at a highly alkaline solution (0.70 mgP/g at pH 11.0). Experimental results showed that the maximum adsorption capacity of fluoride to quintinite was 7.71 mg/g.

The adsorption of fluoride to quintinite was not changed at pH $5-9$ but decreased considerably at the highly acidic (pH < 3) and alkaline (pH > 11) solution conditions.

Therefore, this study elucidated that the inorganic functional materials removed phosphorous, chromium, and fluorine from aqueous solutions, effectively. These results also demonstrate that the functional polymer composites developed in this study can be applied to water treatment system.

CONTENTS

Chapter 4 Preparation and characterization of triamine-functionalized mesoporous silica-polymer composites for Cr(VI) removal from industrial plating wastewater 75

Chapter 5 Characterization of calcined Mg-Fe layered double hydroxide for phosphate removal from aqueous solutions 120

Chapter 6 Preparation and characterization of calcined Mg-Fe layered double hydroxide PVDF/PVA composites for phosphate removal from aqueous solutions 153

List of Tables

xi

List of Figures

Chapter 1 Introduction

1.1. Background

Phosphorus is known as a key limiting nutrient in freshwater systems (Carey and Rydin, 2011). Phosphorus is one of the most severe environmental problems contributing to the eutrophication of both aquatic and terrestrial natural ecosystems and reducing the quality of drinking water in many regions (Herzog *et al*., 2008). Phosphate is an essential macronutrient in aquatic environments, but in excessive amounts, it causes eutrophication of reservoirs, lakes and coastal areas (Colney *et al*., 2009). It has been considered that T-P concentration of 0.035 mg/L is eutrophic critical value (OECD, 1982). Effluent concentration of phosphate from wastewater treatment facilities and industrial plants must be controlled through chemical and biological techniques to meet the discharge limits (Xiong *et al*., 2008; Wang *et al*., 2005). Various treatment technologies such as chemical, biological, and membrane techniques have been applied to reduce the phosphate concentration in wastewater before its discharge (Morse *et al*., 1998). Among these techniques, adsorption is widely used as a phosphate treatment method mainly because of cost-effectiveness and simplicity of operation. Various adsorbents including metal (Fe, Al, Zr) (hydr)oxides, industrial by-products (slags, fly ash), and calcium/magnesium carbonates (hydroxides) have been applied for phosphate adsorption (Loganathan *et al*., 2014).

Chromium and its compounds are widely used in electroplating, leather tanning, cement, dyeing, metal processing, wood preservatives, paint and pigments, textile, steel fabrication and canning industries. These industries produce large quantities of toxic wastewater effluents

(Nomanbhay and Palanisamy, 2005). Chromium pollution is one of typical problem related to industrial wastewater treatments. Chromium contamination of drinking water resources is a serious environmental problem around the globe. In many countries such as China, USA, Canada, Mexico, India, and Italy, chromium is present in groundwater at concentrations exceeding the guidelines of the World Health Organization (0.05 mg/L), causing serious health problems (Richard and Bourg, 1991). Chromium can exist in oxidation states ranging from -2 to + 6. In aquatic environments, however, trivalent Cr(III) and hexavalent Cr(VI) are the major forms of chromium, and Cr(VI) is more toxic and cancerous (Richard and Bourg, 1991; Sharma *et al*., 2011). Various adsorbents such as activated carbon, iron oxide, aluminum oxide, layered double hydroxide, clays and coal/bone charcoal have been used for chromium removal (Sharma *et al*., 2008).

Fluoride is an essential micronutrient for human health preventing dental caries and helping dental enamel calcification. At concentrations greater than 1.5 mg/L, however, fluoride can cause dental/skeletal fluorosis and neurological damage. The contamination of fluoride in drinking water resources is a serious environmental problem around the world. Fluoride contamination in surface and groundwater can come from natural geological sources (fluorite, biotites, granite, basalt, etc) and from industrial wastewaters (semiconductor manufacturing, electroplating, glass and ceramic production, etc) (Cai *et al*., 2012). In many countries, fluoride occurs naturally in groundwater at concentrations exceeding the guidelines of the World Health Organization (1.5 mg/L), causing serious health problems (Ayoob and

Gupta, 2006). Fluoride management is considered one of the most important issue for groundwater quality. Various adsorbents have been applied for fluoride removal, including activated alumina, activated carbon, granular ferric hydroxide, limestone, fly ash, and clay (Mohapatra *et al*., 2009; Bhatnagar *et al*., 2011).

Various adsorbents have been used alone and in their powder form. However, the use of adsorbents in powdered form has some problems, such as difficulty in the separation of adsorbents after adsorption, mass loss after regeneration and low strength and small particle size, which make it difficult to use in column applications (Aksu *et al*., 2002). To overcome these problems, the powdered adsorbents can be immobilized in a supporting materials.

There are some reports on immobilization of modifiers like chelate forming organic reagents, polymers, metal salts, natural compounds and some microorganisms on solid matrices like ion-exchange resins, cellulose, fibers, activated carbon, sand, clay, zeolites, polymers, metal oxides and highly dispersed silica (Jal *et al*., 2004). The immobilization of functional materials into polymer is widely applied for contaminants removal from aqueous solutions because it is simple and cost-effective.

A number of studies proposed a variety of polymer composites for adsorbent materials. Chitosan is the N-deacetylated product of chitin and an attractive material because of its properties such as hydrophilicity, low cost, non-toxicity, and biodegradability (Kumar, 2000). Wang and Wang (2007) reported the use of montmorillonite in forming chitosan composites for the removal of ionic dye. Baroni *et al*. (2008) used the cross-linked chitosan membranes to remove chromium ions from

aqueous solution. Sun *et al*. (2009) produced chitosan/cellulose composite for the removal of Cr(VI).

Sodium alginate is also a nontoxic and biodegradable natural polymer. However, mechanical strength and chemical stability of alginate hydrogels are poor. It is, therefore, necessary to improve their properties through blending with polymers such as polyvinyl alcohol (PVA). Polyvinyl alcohol (PVA) is non-toxic, biocompatible, cheap and chemically stable (Lee *et al*., 2013). Zouboulis and Katsoyiannis (2002) investigated arsenic removal using iron oxide loaded alginate composites. Lv *et al*. (2013) synthesized Fe^0-Fe_3O_4 containing PVA/alginate composite for Cr(VI) removal.

Poly(vinylidene) fluoride (PVDF) has excellent chemical resistance and good thermal stability. The addition of hydrophilic materials such as PMMA, PMA, PVAC to PVDF increase the hydrophilicity of a composite. Zheng *et al*. (2011) studied adsorption of arsenic by a PVDF/zirconia membrane. Liu *et al*. (2007) produced PA/PVDF composite membrane.

However, the high cost fabrication process, complex steps for the incorporation of nanocomponent, and lack of specific functional groups in the hydrogels for binding might limit the application of the polymer composites as adsorbent (Kim *et al*., 2015). In this study, one of the main focuses is to easily synthesize efficient and environmentally friendly (nontoxic and reusable) polymer composites incorporated with an inorganic functional materials and polymers.

1.2. Objective

The objective of this thesis is to synthesize inorganic functional materials and their polymer composites, and to apply as adsorbents for anionic contaminant removal in water. The specific objectives of the dissertation are to:

■ Synthesize iron oxide nanoparticle(ION)–chitosan composites as an eco-friendly adsorbent and evaluate the phosphate removal capacity by batch experiments, column experiments and pilot-scale adsorption tower experiment. (Chapter 3).

■ Investigate chromate removal using triamine-functionalized mesoporous silica-polymer composites from industrial plating wastewater and examine the effects of adsorbent dose, solution pH, reaction time, initial concentration, and temperature with model analyses. (Chapter 4).

■ Characterize Mg-Fe calcined layered double hydroxide (CLDH) and examine the potential as an adsorbent for phosphate removal from synthetic aqueous solution and real stream water. (Chapter 5).

■ Evaluate phosphate removal capacity of MgFe CLDH-PVDF/PVA composites and investigate the reusability by batch experiments and column experiments using real stream water.

(Chapter 6).

■ Evaluate the sorption capacities of phosphorous and fluorine by quintinite and examine the effects of adsorbent dose, solution pH, reaction time, initial concentration, and temperature with model analyses. (Chapter 7).

The flow chart of this thesis is shown in Figure 1.1.
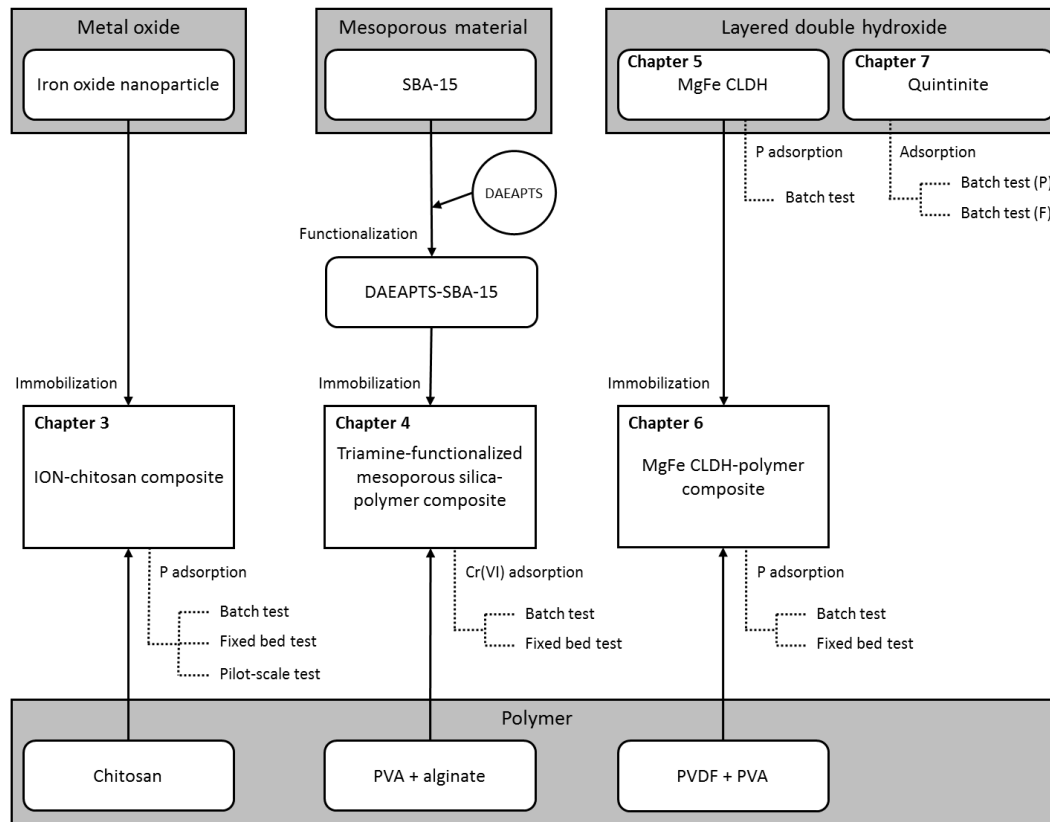
Figure 1.1 Flow chart of the study.

Chapter 2 Literature Review

2.1. Inorganic adsorbents for anionic contaminants removal

There have been many attempts to develop an adsorbent demonstrating a high adsorption capacity and low cost for anioninc contaminant removal from water. Inorganic adsorbents have been studied widely, aiming at providing an alternative to the commercial adsorbents in the treatment of surface and ground water and industrial effluents (Jiang and Ashekuzzaman, 2012).

Iron oxides exist in many forms in nature. Magnetite (Fe_3O_4), maghemite (γ-Fe_2O_3), and hematite (α-Fe_2O_3) are the most common forms (Xu *et al*., 2012). Due to their size in nano-range, high surface area to volume ratios, low toxicity, chemical inertness, easy synthesis, coating or modification iron oxide nanoparticles have been widely studied (McHenry and Laughlin, 2000; Boyer *et al*., 2010; Dias *et al*., 2011). Several researchers applied iron oxide nanoparticles to remove contaminants from water. de Vicente *et al*. (2010) removed phosphate from lake water by iron, magnetite nanoparticles. Magnetite adsorbed more phosphate (27.15 mgP/g) than iron particles (18.83 mgP/g). A slight decrease in phosphate adsorption capacity of reused particles was observed for iron particles (from 18.83 to 15.80 mgP/g) and for magnetite (from 27.15 to 23.83 mgP/g). They maintained that iron and magnetite had biocompatibility and low toxicity. Chowdhury and Yanful (2010) investigated arsenic and chromium removal from different water samples using nano-size magnetite and mixture of magnetite and maghemite. The results showed that the removal of arsenic and chromium from water depended on pH, contact time, initial

concentration, phosphate concentration in water, and adsorbent dosage. They compared different nanoscale iron-based adsorbents. The costs of iron oxides, such as hematite, magnetite, maghemite were lower than zeovalent iron and iron hydroxide. Daou *et al*. (2007) used iron oxide nanoparticles to remove the phosphate and investigated the adsorption mechanisms via infrared spectra, X-ray photoelectron spectroscopy and Mössbauer spectrometry analyses. Characterization of magnetite which adsorbed phosphate had demonstrated that phosphate adsorption occurred by interaction with Fe^{3+} in octahedral sites with formation of monoprotonated binuclear species.

Layered double hydroxides (LDHs) are a class of nanostructured anionic clays. Because LDHs have high surface area, large anion exchange capacity, and good thermal stability (Cavani *et al*., 1991), they have been widely tested for the removal of inorganic contaminants, including arsenic, borate, chromate, nitrate, and selenium, from contaminated waters (del Arco *et al*., 2000; Das *et al*., 2004; Gillman, 2006; Islam and Patel, 2009).

Parallel to these studies, numerous researchers have examined the possibility of phosphate adsorption by various types of LDHs and their composites (Seida and Nakano, 2002; Cheng *et al*., 2009; Chitrakar *et al*., 2010; Triantafyllidis *et al*., 2010; Han *et al*., 2011; Han *et al*., 2012; Zhang *et al*., 2013; Yang *et al*., 2014). Kuzawa *et al*. (2006) performed batch and column experiments using powder- and granular-type Mg-Al LDHs as adsorbents for phosphate removal from aqueous solutions. The maximum adsorption capacity (47.3 mgP/g) of the granular LDH obtained experimentally was about 90% of that of the powdered LDH.

The LDH could be reused after desorption of phosphate with alkaline NaCl solutions followed by regeneration with 25 w/v% $MgCl_2$ solution.

He *et al*. (2010) investigated the selective adsorption of phosphate on CO_3^{2-}, Cl^-, and NO_3^- -type ZnAl LDHs and the calcined CO_3^{2-} -type LDH at 200, 400, 600, and 800 °C, respectively. The calcined LDHs and NO_3^- -type LDH exhibited high selectivity toward phosphate ions only, while the Cl^- -type LDH showed selectivity toward both SO_4^{2-} and phosphate ions. The calcined LDHs showed good stability and reusability, with the maximum phosphate removal capacity of about 16 mgP/g. Das *et al*. (2006) have prepared Al-based (Mg-Al, Zn-Al, Ni-Al, Co-Al) and Fe-based (Mg-Fe, Zn-Fe, Ni-Fe, Co-Fe) LDHs and calcined these at 500 °C to compare their sorption capacities for phosphate. The results showed that calcined Mg–Al LDH with Mg–Al molar ratio of 2.0 had higher adsorption capacity compared to other calcined LDHs as it possessed higher Al^{3+} content. Chitrakar *et al*. (2005) characterized the sorption of phosphate from seawater to Mg-Mn LDHs calcined at 300 °C using batch experiments. Mg-Mn LDHs calcined at 300 °C showed the highest phosphate uptake from the seawater among the inorganic adsorbents studied (Mg-Mn LDH, Mg-Mn LDH calcined at 300 °C, activated magnesia, hydrous aluminum oxide, manganese oxide(δ-MnO_2)). The calcined Mg-Mn LDH had high chemical stability against the adsorption/desorption cycle.

Batistella *et al*. (2011) evaluated the effect of acid activation on the removal of fluoride by Mg-Al-CO_3 LDHs. The enhancement in adsorption capacity was verified at pH 3.5 (compared to pH 5.0) and temperature of 50 °C (compared to 10 °C), indicating the endothermic

nature of the process. Mandal and Mayadevi (2009) performed the kinetic, equilibrium, and thermodynamic studies for the fluoride removal by Zn/Al/Cl anionic clay. The LDH was regenerated up to five cycles and a decrease in 28% adsorption capacity was observed after five cycles of regeneration.

Others used calcined LDHs (CLDHs) derived from the various LDH particles via calcination for fluoride removal (Kim *et al*., 2013; Lv, 2007; Wang *et al*., 2007; Lv *et al*., 2006; Das *et al*., 2003; Díaz-Nava *et al*., 2003). Cai *et al*. (2012) examined the competitive adsorption of fluoride and phosphate by Mg-Al-CO$_3$ CLDH. The results showed that the optimal pH was around 6 and it took 24 h to attain equilibrium when fluoride and phosphate were simultaneous added. Zhou *et al*. (2011) investigated the adsorption properties of fluoride in water by Li/Al CLDHs. It was found that near neutral solution pH was more favorable for adsorption of fluoride in Li/Al CLDHs. These studies showed that LDHs are effective adsorbents for the removal of phosphate and fluoride from water.

Mesoporous silicas, like SBA-15, have showed many attractive characteristics, including large surface area, highly ordered structure, controlled pore diameter, and incorporation of specific bonding materials (Wu *et al*., 2014). The high density of surface silanol groups (SiOH), which are responsible for ion exchange and postmodification is beneficial to introducing functional groups with high coverage (Zhao *et al*., 1997). It is expected that functionalized mesoporous silica has well-defined meso-framework structure with a high adsorption capacity (Yoshitake *et al*., 2003).

Many researchers have examined the functionalization of mesoporous silica using different materials for the adsorption of heavy metals from aqueous solution, such as alumina (He *et al*., 2015), barium titanate (Kumari *et al*., 2015), iron (Li, 2013), polyamidoamine (Jiang *et al*., 2007), diethylenetriamine (Dey *et al*., 2008), and imidazole (Marschall *et al*., 2009). Among these materials, amino functionalization has been widely and thoroughly studied and it has exhibited high affinity to heavy metal ions, such as copper, lead, cadmium, and zinc (Wu *et al*., 2014). The aminosilanes are considered to interact with oxyanions as the cationated amino groups (Yoshitake *et al*., 2002a).

Dindar *et al*. (2015) modified mesoporous materials with aminopropyl and N-propylsalicylaldimine groups and used for removal of Cr(VI), As(V) and Hg(II). The adsorption kinetics were very rapid and the processes were controlled by enthalpy changes. Adsorption-desorption experiments revealed multiuse of the adsorbents for removal of Cr(VI), As(V) and Hg(II) ions from water. Idris *et al*. (2013) synthesized 3-aminopropy-functionalized silica nanoparticles to be evaluated for Cr(VI) uptake and the adsorption behaviors were analyzed using adsorption isotherms, kinetic models. The results demonstrated that pores size distribution, not the surface area or the average pore size, was central to ensure optimum adsorbent performance for removal of Cr(VI). Li *et al*. (2008 and 2007) functionalized mesoporous silica with aminopropyl, imidazole and triazole groups and employed as and adsorbent of Cr(VI). It was found that the combination of mesoporous silica supports possessed cylindrical mesopore channels with covalently anchored organic groups could create efficient capabilities for Cr(VI)

adsorbents. Yoshitake *et al.* (2003) investigated the arsenate adsorption properties of cation-anchored functionalized mesoporous silicas. The difference between the meso-framework structures appeared in their adsorption capacity.

2.2. Composite adsorbents

Composites can be defined as natural or synthesized materials made from two or more materials with significantly different physical and chemical properties which remain separate and distinct at the microscopic or macroscopic scale within the material. Composites are synthesized to combine the desired properties of the materials in the composite (Srinivasan, 2011).

Jing *et al.* (2012) synthesized bifunctional adsorbent with titanium, lanthanum and granular activated carbon. The composite could be used as adsorbent for simultaneous removal of As(V) and F. Saleh and Gupta (2012) synthesized manganese dioxide-coated multiwall carbon nanotube nanocomposite. In the fixed bed system, it was found that the higher the layer thickness of the nanocomposite, the more Pb(II) removal. Ren *et al.* (2011) synthesized graphene nanosheet/δ-MnO_2 composite by a microwave-assisted method. The adsorption capacity of Ni (II) for the composite (46.6 mg/g) was 1.5 and 15 times higher than those for δ-MnO_2 and graphene nanosheet, respectively. Shi *et al.* (2011) prepared

the composite by loading iron oxide onto activated carbon. The composite showed fast adsorption rates and high adsorption capacities and its adsorptive performance for phosphate ions was dependent on the pH value. The adsorption capacity of phosphate ions at pH 3.0 were 98.39 mg/g for the composite.

Yao *et al*. (2009) prepared iron oxide/fly ash composite employing municipal solid waste fly ash and iron nitrate to remove phosphate ions from water. The phosphate removal decreased dramatically with increasing pH over the pH range 3–5 and then decreased slowly with further increase in the pH value. Chen *et al*. (2008) synthesized the composite composed of silica gel, calcium silicate hydrate gel and calcite. The composite adsorbent appeared to be suitable for the removal of heavy metal ions from wastewater over a wide range of concentrations and pH conditions. Fan and Anderson (2005) prepared Mn oxide-coated granular activated carbon. The Cd(II) and Cu(II) adsorption capacities of the composite were greatly improved by Mn oxide coating.

2.3. Polymer composites

The immobilization of functional materials into polymer is widely applied for contaminants removal from aqueous solutions because it is a simple and cost-effective (Lazaridis and Charalambous, 2005; Nayak *et al*., 2007).

Hui *et al*. (2014) prepared poly(vinyl alcohol) (PVA) hydrogel beads and investigated adsorption mechanism of the beads for phosphate

removal. The acidic environment was favorable for phosphate adsorption by the composite. The formed network structure of the composite after one cycle would not change any more in the following four-time adsorption-desorption processes, resulting in the stable phosphate adsorption capacity. Lee (2014) synthesized magnetic alginate-LDH composite employing calcined Mg-Al LDH, magnetic iron oxide, and alginate. The sorption capacity of magnetic composites was 4.99 mg/g for phosphate and 1.61 mg/g for chromate. The composites could be easily separated by magnetic separation and reused. Lee *et al*. (2013) synthesized alginate/PVA composites containing hematite and investigated the removal of Cr(VI) from aqueous solution. The results demonstrated that Cr(VI) removal was very sensitive to solution pH between 2.0 and 9.0 with the highest removal capacity at the highly acidic solution pH.

Kumar *et al*. (2011) reported the adsorption of Cr(VI) from industrial wastewater using cellulose-montmorillonite. The composite could be reused with quantitative recovery for 10 adsorption-desorption cycles. Taha *et al*. (2012) fabricated amino functionalized mesoporous polyvinyl pyrrolidone (PVP)/SiO_2 composite nanofiber membranes. The composite nanofiber had large surface areas per unit volume to mass, and amino groups were highly effective in removing of specific materials by adsorption based on chemical or physical affinity. Bleiman and Mishael (2010) prepared chitosan-montmorillonite composites and examined the adsorption of selenium by the composites. The column experiment demonstrated that selenium adsorption by the composite was higher than by Al-oxide due to high adsorption of sulfur by the Al-oxide.

Viswanathan *et al*. (2009) used protonated chitosan composites to removal of fluoride. The composite showed a maximum defluoridation capacity of 1.66 mg/g. Filed trial results also indicated that the composite could be employed as an adsorbent for fluoride removal.

Gupta *et al*. (2009) studied removal of As(III) and As(V) from groundwater using iron-chitosan composites. The composite was successfully applied for the removal of both As(III) and As(V) from real life groundwater. Sorption-desorption studies by column experiment for two cycles using arsenic spiked groundwater demonstrated the reusability of the composite. Boddu *et al*. (2008) reported the removal of As(III) and As(V) by chitosan coated alumina. The results showed that As(V) more adsorbed on the composite than As(III), which was explained on the basis of speciation of arsenic at pH 4.0. Column experiment results indicated that no arsenic was found in the effluent solution up to about 40 and 120 bed volumes of As(III) and As(V), respectively. Ansari (2006) investigated Cr(VI) adsorption from aqueous solutions using sawdust coated by polyaniline (SD/PANI) polyaniline composites with nylon 66 and polyurethane. It was found that polyaniline in the acid doped form, can be used for Cr(VI) ion removal below pH 2.

Most of the studies indicated that polymer composite could be synthesized easily and remove anionic contaminants efficiently from water. In most studies, the polymer composite also revealed good reversibility and multicycle stability. It is considered that polymer composite is a good candidate for an adsorbent towards anionic contaminants.

2.4. Data analyses

In order to investigate the adsorption processes, nonlinear forms of pseudo first-order (eq. 1), pseudo second-order (eq. 2), and Elovich (eq. 3) kinetic models (Gupta and Bhattacharyya, 2011) have been commonly used to determine the best fitted model:

$$q_t = q_e(1 - e^{-k_1 t}) \tag{1}$$

$$q_t = \frac{k_2 q_e^2 t}{1 + k_2 q_e t} \tag{2}$$

$$q_t = \frac{1}{\beta} ln(\alpha\beta) + \frac{1}{\beta} ln\, t \tag{3}$$

where q_e is the adsorption capacity at equilibrium, q_t is the adsorption capacity at time t, k_1 is the pseudo first-order rate constant, k_2 is the pseudo second-order rate constant, α is the initial adsorption rate constant, and β is the Elovich adsorption constant. Weber-Morris intraparticle diffusion model also has been used to fit adsorption data and to investigate the mechanism of adsorption (Bajpai *et al*., 2009):

$$q_t = k_i\, t^{1/2} + I \tag{4}$$

where k_i is the intra-particle diffusion rate constant and I is the intercept related to the thickness of the boundary layer.

Equilibrium data, commonly known as adsorption isotherms, are

important for the design of adsorption systems (Aksu and Kabasakal, 2004). Various isotherm equations such as Freundlich (eq. 5), Langmuir (eq. 6), and Redlich-Peterson (eq. 7) isotherm models have been used to describe the equilibrium characteristics of adsorption (Foo and Hameed, 2010):

$$q_e = K_F C_e^{1/n} \tag{5}$$

$$q_e = \frac{Q_m K_L C_e}{1 + K_L C_e} \tag{6}$$

$$q_e = \frac{K_R C_e}{1 + a_R C_e^g} \tag{7}$$

where C_e is the equilibrium concentration of adsorbate in the aqueous solution, K_F is the Freundlich constant related to the adsorption capacity, $1/n$ is the Freundlich constant related to the adsorption intensity, Q_m is the maximum adsorption capacity, K_L is the Langmuir constant related to the affinity of the binding sites, K_R is the Redlich-Peterson constant related to the adsorption capacity, a_R is the Redlich-Peterson constant related to the affinity of the binding sites, and g is the Redlich-Peterson constant related to the adsorption intensity.

The concept of thermodynamics assumes that in an isolated system without energy gain or lost, the entropy change is the driving force. Gibbs free energy is the chemical potential that is minimized when the system reaches equilibrium at constant temperature and pressure (Stavropoulos *et al*., 2016). Thermodynamic parameters were obtained

from the following equations (Goswami and Purkait, 2011):

$$\Delta G^o = \Delta H^o - T\Delta S^o \tag{8}$$

$$ln(K_e) = \frac{\Delta S^o}{R} - \frac{\Delta H^o}{RT}; \; K_e = \frac{aq_e}{C_e} \tag{9}$$

where ΔG^o is the change in Gibb's free energy, ΔS^o is the change in entropy, ΔH^o is the change in enthalpy, K_e is the equilibrium constant (dimensionless), and *a* is the adsorbent dose (g/L). Values of ΔS^o and ΔH^o were determined by plotting *ln (K_e)* versus 1/*T* using Eq. (9), and then value of ΔG^0 was calculated from Eq. (8).

The total mass of adsorbate injected into the column (m_{total}, mg) during column experiment was calculated as follows:

$$m_{total} = \frac{C_0 Q t_{total}}{1000} \tag{10}$$

where C_0 is the influent concentration of adsorbate; Q is the volumetric flow rate; and t_{total} is the total flow time. The removal capacity of the column for adsorbate (q_{total}, mg) at a given flow rate and influent concentration was quantified as follows:

$$q_{total} = \frac{Q}{1000} \int_{t=0}^{t=total} (C_0 - C)dt \tag{11}$$

where *C* is the effluent concentration of adsorbate. The total removal

percentage of adsorbate during the experiment (Re, %) was determined as follows:

$$Re = \left(\frac{q_{total}}{m_{total}}\right) \times 100 \qquad (12)$$

The mass of removed adsorbate unit mass of filter medium (q_{eq}, mg/g) was calculated as follows:

$$q_{eq} = \frac{q_{total}}{M_f} \qquad (13)$$

where M_f is the mass of the filter medium in the column.

All of the parameters of the models were determined by non-linear regression using MS Excel 2010 (Microsoft corp.) with the solver add-in function incorporated into the program. Coefficient of determination (R^2), chi-squared coefficient (χ^2), and sum of the absolute errors (SAE) were used to evaluate the optimum isotherm and kinetic model parameters for the experimental data. The expressions of R^2, χ^2, and SAE were given below:

$$R^2 = \frac{\sum_{i=1}^{m}(y_c - \overline{y_e})_i^2}{\sum_{i=1}^{m}(y_c - \overline{y_e})_i^2 + \sum_{i=1}^{m}(y_c - y_e)_i^2} \qquad (14)$$

$$\chi^2 = \sum_{i=1}^{m}\left\{\frac{(y_e - y_c)^2}{y_c}\right\}_i \qquad (15)$$

$$\text{SAE} = \sum_{i=1}^{m} |q_c - q_e|_j \qquad (16)$$

where y_c is the calculated removal capacity from the model, y_e is the measured removal capacity from experiment, and $\overline{y_e}$ is the average of the measured removal capacity.

Nomenclature

$1/n$	Freundlich constant related to the adsorption intensity
a	Adsorbent dose (g/L)
a_R	Redlich-Peterson constant related to the affinity of the binding sites
C	Effluent concentration of adsorbate (mg/L)
C_0	Influent concentration of adsorbate (mg/L)
C_e	Equilibrium concentration of adsorbate in the aqueous solution (mg/L)
g	Redlich-Peterson constant related to the adsorption intensity
I	Intercept related to the thickness of the boundary layer
k_1	Pseudo first-order rate constant
k_2	Pseudo second-order rate constant
K_e	Equilibrium constant (dimensionless)
K_F	Freundlich constant related to the adsorption capacity
k_i	Intra-particle diffusion rate constant
K_L	Langmuir constant related to the affinity of the binding sites
K_R	Redlich-Peterson constant related to the adsorption capacity
M_f	Mass of the filter medium in the column
m_{total}	Total mass of adsorbate injected into the column
Q	Volumetric flow rate
q_e	Adsorption capacity at equilibrium (mg/g)
q_{eq}	Mass of removed adsorbate unit mass of filter medium (mg/g)
Q_m	Maximum adsorption capacity
q_t	Adsorption capacity at time t (mg/g)
q_{total}	Removal capacity of the column for adsorbate

R^2	Coefficient of determination
Re	Total removal percentage of adsorbate during the experiment (%)
SAE	Sum of the absolute errors
t	Time
t_{total}	Total flow time
y_c	Calculated removal capacity from the model
y_e	Measured removal capacity from experiment
$\overline{y_e}$	Average of the measured removal capacity
α	Initial adsorption rate constant
β	Elovich adsorption constant
ΔG^o	Change in Gibb's free energy
ΔH^o	Change in enthalpy
ΔS^o	Change in entropy
χ^2	Chi-squared coefficient

Chapter 3 Phosphate removal from aqueous solution by using iron oxide nanoparticle-chitosan composites

Iron oxide nanoparticles are well known as useful adsorbents (Yoon *et al*., 2014) and can be easily synthesized. Meanwhile, chitosan has a high potential for phosphate anions sorption due to the presence of amino functional groups (Bozorgpour *et al*., 2016). Additionally, chitosan is normally insoluble in water at near at neutral pH and the biodegradability of chitosan could decrease the second contamination to environment (Miretzky and Cirelli, 2009). The aims of this chapter were synthesis of eco-friendly adsorbent and evaluation of its field applicability. To examine the phosphate removal capacity, batch and column experiments were conducted using real stream water. Long-term pilot-scale experiment was also carried out for 33 days.

3.1. Materials and Methods

3.1.1. Synthesis of ION-chitosan composites

All chemicals used for the experiments were purchased from Sigma Aldrich. A powder form of iron oxide nanoparticle (ION) was synthesized by a co-precipitation method. An alkali solution of 6 M sodium hydroxide (NaOH) was added drop-wise with intensive stirring at room temperature into a 500 mL solution of ferrous sulfate heptahydrate ($FeSO_4 \cdot 7H_2O$, 0.25 M) and ferric chloride hexahydrate ($FeCl_3 \cdot 6H_2O$, 0.5 M) to obtain a pH of 7.6. The resulting precipitates were aged at 60 °C for 18 h and then washed thoroughly with deionized water to remove any excess sodium. The washed precipitates were oven-dried at 150 °C for 6 h in an electric muffle furnace (C-FMA, Vision Lab,

Korea) and then pulverized in a ball mill.

The preparation of iron oxide nanoparticle-chitosan composites (ION-chitosan composites) was as follows. Chitosan solution was prepared by dissolving chitosan flakes (3% w/w) in 70 mL of dilute acetic acid solution (2% w/w). The chitosan solution was stirred with a magnetic bar for 18 h at 60 °C to dissolve chitosan completely. Under magnetic stirring, 30 mL of deionized water containing ION (6% w/w) was added to the chitosan solution, followed by 2 h of sonication. The solution was stirred for 12 h at 60 °C to obtain a homogeneous suspension.

The suspension was filled in plastic syringe and then dropped into NaOH-methanol solution (0.2 mol NaOH per liter methanol) using a syringe pump (78-1100I, Fisher Scientific) at 4 mL/min. The suspension droplets formed beads instantaneous in the solution, and were remained in the aqueous solution for 12 h. Then ION-chitosan composites were thoroughly rinsed with deionized water to remove residual NaOH and stored in deionized water. Before used for experiments, the composites were air-dried for 20 min.

3.1.2. Characterization of ION-chitosan composites

The powder form of ION was characterized by powder X-ray diffractometry (XRD, D8 Advance, Bruker, Germany) with a Cu Kα radiation of 1.5406 Å at a scanning speed of 0.6 °/sec.

To characterize the ION-chitosan composites, Field emission scanning electron microscopy (FESEM) analysis and energy dispersive

X-ray spectrometry (EDS) analysis were performed using a field emission scanning electron microscope (Supra 55VP; Carl Zeiss, Oberkochen, Germany). From the N_2 adsorption-desorption isotherms, the specific surface area, average pore diameter, total pore volume, and mesopore volume were determined using Brunauer-Emmett-Teller (BET), Barrett-Joyner-Halenda (BJH), and Horvath-Kawazoe (HK) analyses with an ASAP 2010 instrument (Micromeritics, Nocross, Georgia, USA).

3.1.3. Stream water samples

The stream water samples were collected from the Seoho stream located in Suwon, Korea. The ionic composition of the stream water was analyzed using ion chromatograph (ICS-3000; Dionex, USA), and chemical oxygen demand (COD_{cr}) was measured according to standard method (APHA, 1995).

The stream water had the following composition: $NaCl = 2.41$ mM, $NaHCO_3 = 0.38$ mM, $Ca(HCO_3)_2 = 0.67$ mM, $CaSO_4 = 0.17$ mM, $MgSO_4 = 0.20$ mM, $Mg(NO_3)_2 = 0.03$ mM, $KNO_3 = 0.32$ mM, $K_2HPO_4 = 1.77 \times 10^{-4}$ mM, COD = 4.2 mg/L, pH = 6.9, IS = 613 μS/cm. The stream water was passed through a 0.45 μm filter prior to the experiments in order to remove microorganisms and suspended particles. For the stream water sample, which was very low in phosphate concentration (0.017 mgP/L), potassium dihydrogen orthophosphate (KH_2PO_4) was added to meet the initial P concentration of 100 mgP/L. The desired phosphate solution was prepared by diluting the stock solution.

Table 3.1 Characteristics of stream water samples.

Components	Values
NaCl (mM)	2.41
NaHCO$_3$ (mM)	0.38
Ca(HCO$_3$)$_2$ (mM)	0.67
CaSO$_4$ (mM)	0.17
MgSO$_4$ (mM)	0.20
Mg(NO$_3$)$_2$ (mM)	0.03
KNO$_3$ (mM)	0.32
K$_2$HPO$_4$ (mM)	1.77×10^{-4}
COD (mg/L)	4.2
pH	6.9
IS (μS/cm)	613

3.1.4. Batch experiments

Phosphate removal by ION-chitosan composites was conducted under batch conditions. The phosphate solution was prepared using real stream water. The batch experiments were performed at 30 °C using 50 mL polypropylene conical tubes, unless otherwise stated. All of the batch experiments were performed in triplicate.

To investigate dose effect of adsorbent, specific quantities of ION-chitosan composites were added into each 30 mL solution to make 5, 10, 20, 30, 40, 50 g/L. The experiments were conducted at an initial phosphate concentration of 1, 2, 4, 8 mgP/L. The tubes were shaken at 30 °C and 100 rpm using a shaking incubator (Daihan Science, Seoul, Korea). After 12 h, the samples were collected and filtered through a 0.45 µm membrane filter. The phosphate was analyzed by the ascorbic acid method (APHA, 1995). The phosphate concentrations were measured at a wavelength of 880 nm using a UV-vis spectrophotometer (Helios, Thermo Scientific, Waltham, MA, USA).

For the pH experiments (adsorbent dose = 30 g/L; initial phosphate concentration = 2 mgP/L; temperature = 30 °C), 0.1 M NaOH and 0.1 M HCl solutions were used to adjust the pH of the reaction solution from 5.02 to 9.03. The pH was measured with a pH probe (9107BN, Thermo Scientific, USA).

To determine the effect of reaction time on the removal of phosphate, 30 g/L of adsorbents were added to 30 mL solution (initial phosphate concentration = 1, 2, 4, 8 mgP/L). In the experiments, samples were collected after various reaction times ranging from 15 min to 12 h. The additional experiments were performed at 15 and 45 °C to examine the

effect of temperature on phosphate removal.

Further batch experiments were conducted at different initial concentration of phosphate solution. ION-chitosan composites (dose = 5, 10, 20, 30 g/L) were added 30 mL of solution (initial phosphate concentration = 1 − 20 mgP/L). The sample were collected 12 h post-reaction.

The batch experiments were conducted to examined the repeated use of ION-chitosan composite for phosphate sorption (adsorbent dose = 30 g/L; initial phosphate concentration = 2 mgP/L). For each round of the sorption experiments, desorption of the phosphate from ION-chitosan composite was performed by dispersing the adsorbents in 5 mM NaOH solution for 24 h. Then, adsorbents were air-dried for 20 min. After regeneration of the used adsorbent, ION-chitosan composite was reused for the sorption experiments.

Table 3.2 Batch experimental conditions for the phosphate sorption to ION-chitosan composite.

	Dose (g/L)	Reaction Time (h)	Initial conc. (mgP/L)	Solution pH	Temperature (°C)	Solution volume (mL)
Effect of dosage	5 – 50	12	1 - 8		30	30
Effect of solution pH	30	12	2	5.02 – 9.03	30	30
Effect of reaction time	30	0.25 – 12	1 – 8		15 – 45	30
Effect of initial concentration	5 – 30	12	1 – 20		30	30
Effect of repeated use	30	12	2		30	30

3.1.5. Fixed-bed column experiment

Column experiments were performed using a Plexiglas column (inner diameter = 2.5 cm; column length = 10, 20 cm) packed with ION-chitosan composites. For column experiments, a column was packed for each experiment with ION-chitosan composites by the tap-fill method. Prior to the experiments, the packed column was flushed upward using a connected peristaltic pump (QG400, Fluid Metering Inc., Syosset, NY, USA) for 20 pore volumes of deionized water until steady state flow conditions were established. Then, the phosphate solution (initial concentration = 2 mgP/L) was introduced downward into the packed column at the same flow rate in a step injection mode. Portions of the effluent were collected using an autocollector (Retriever 500, Teledyne, City of Industry, CA, USA) at regular intervals.

The effluent pH was measured with a pH probe (9107BN, Thermo Scientific, Waltham, MA, USA) and the electrical conductivity (EC) was measured with an EC probe (815PDL, Istek, Korea). After the column reached exhaustion, ION-chitosan composites were dispersed in 5 mM NaOH solution for 24 h to desorb the phosphate from the composites. The experimental conditions are provided in Table 3.3.

Table 3.3 Fixed-bed column experimental conditions for the phosphate sorption to ION-chitosan composite.

Ex.	Phosphate solution	Adsorbent	Initial conc. (mgP/L)	Linear velocity (cm/min)	Flow rate (mL/min)	Bed depth (cm)	Bed volume (cm^3)	EBCT (min)	Pore volume (cm^3)	Mass of adsorbent (g)	pH$_{effluent}$	EC$_{effluent}$
1	Stream water	Pristine	2	3.33	16.36	10	49.09	3	16.36	48.5	8.30±0.07	554.05±34.65
2	Stream water	Pristine	2	1.67	8.18	10	49.09	6	16.36	48.5	8.29±0.08	547.14±60.60
3	Stream water	Regenerated	2	1.67	8.18	10	49.09	6	16.36	48.5	8.30±0.11	558.23±44.16
4	Synthetic water	Pristine	2	1.67	8.18	10	49.09	6	16.36	48.5	8.26±0.07	539.72±20.17
5	Stream water	Pristine	2	1.67	8.18	20	98.17	6	32.72	97.0	8.19±0.09	534.06±24.54
6	Stream water	Regenerated	2	1.67	8.18	20	98.17	6	32.72	97.0	8.29±0.08	542.44±51.01

3.1.6. Long-term pilot-scale experiment

Based on the results of the lab-scale column experiments, a pilot-scale adsorption tower experiment (Figure 3.1) was performed for 33 days at Seoho pilot plant located in Suwon, Korea. The pilot plant was comprised of equalization tank, chemical reactor, dissolved air flotation, and adsorption tower. Poly aluminum chloride (PAC) was dosed to the chemical reactor from coagulant tank.

The adsorption tower was filled with a 70 cm layer with ION-chitosan composites (Figure 3.2). The total volume of the composites filled in the adsorption tower was approximately 80 L. The source water was pumped from Seoho lake and then flowed upstream through the adsorption tower at a flow rate of 7.05±0.18 L/min, which was equivalent to 4.4 cm/min of linear velocity and 15.8 min of empty bed contact time (Table 3.4).

Raw water samples taken at the inlet of adsorption tower and the concentration of coexisted ions was analyzed by ion chromatograph (ICS-3000, Dionex. USA). The solution pH and dissolved oxygen (DO) were measured on-situ using pH probe (YK-2001PH, Lutron Electronic Enterprise Co., LTD., Taiwan) and DO probe (YK-200PDO, Lutron Electronic Enterprise Co., LTD., Taiwan) (Table 3.5).

The T-P concentrations of influent and effluent were measured by the persulfate digestion method (APHA, 1967) and ascorbic acid method (APHA, 1995).
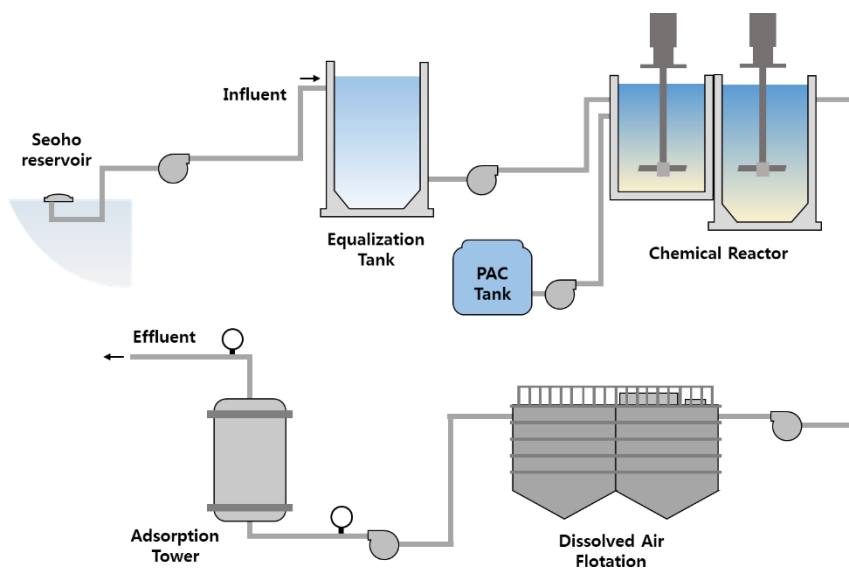
Figure 3.1 Schematic diagram of the pilot plant.
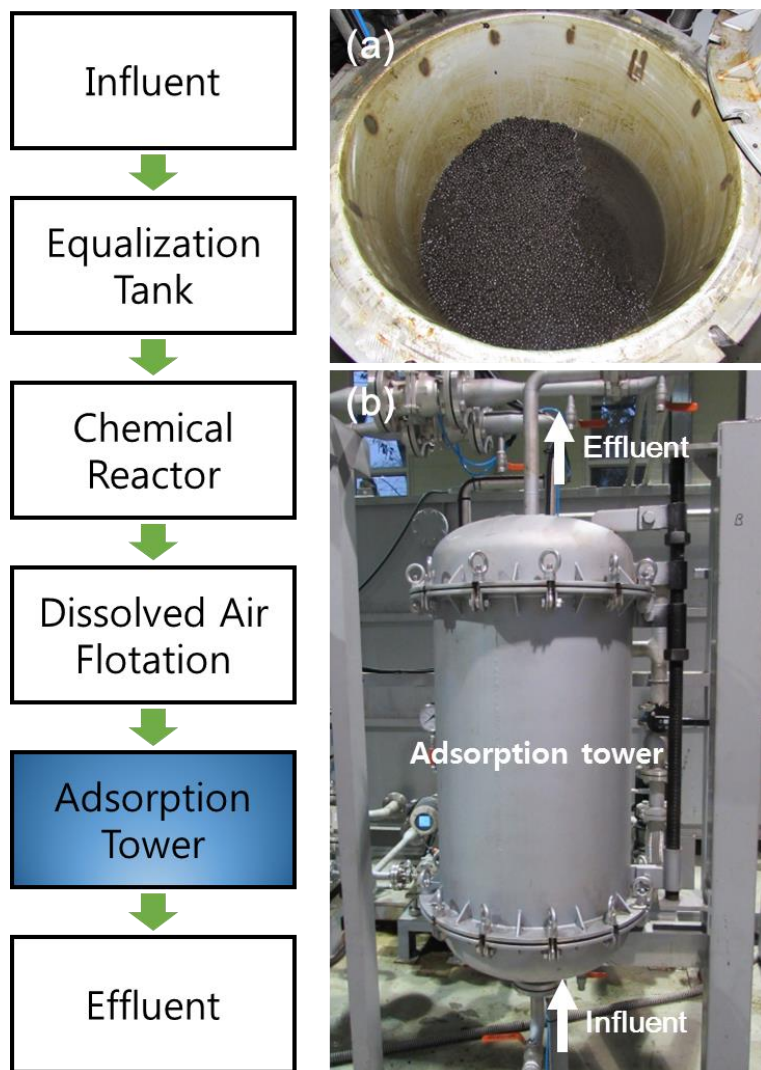
Figure 3.2 Digital images of adsorption tower in the pilot plant: (a) top view of the adsorption tower packed with ION-chitosan composites; (b) side view of the adsorption tower.

Table 3.4 Experimental conditions for long-term pilot-scale adsorption tower experiment.

Parameters	Values
Filter media	ION-chitosan composite
Height of column	100 cm
Height of filter media	70 cm
Inner diameter	45 cm
Flow rate	7.05 ± 0.18 L/min
Linear velocity	4.4 cm/min
EBCT	15.8 min

Table 3.5 Characteristics of influent samples.

Components	Concentration
F	0.04±0.01 mg/L
Cl	82.55±6.25 mg/L
NO_2	0.38±0.11 mg/L
SO_4	29.84±3.04 mg/L
Br	0.04±0.05 mg/L
NO_3	23.22±1.73 mg/L
Na	62.17±3.50 mg/L
NH_4	0.94±0.19 mg/L
K	12.17±1.00 mg/L
Mg	5.72±0.40 mg/L
Ca	28.53±2.14 mg/L
T-P	0.04±0.01 mg/L
pH	7.17±0.23
DO	8.2±1.1 mg/L

3.2. Results and Discussion

3.2.1. Characteristics of ION-chitosan composites

The digital image of ION-chitosan composites are presented in Figure 3.3. The composites had a sphere shape with a particle size of 3.4±0.1 mm.

The FESEM images of ION-chitosan composite are presented in Figure 3.4. It demonstrated that the cross-sectional surface of ION-chitosan composite was heterogeneous in surface topography. The EDS pattern demonstrated that iron (Fe), oxygen (O), and nitrogen (N) were the major elements of the ION-chitosan composite. Iron was found on the ION-chitosan composite at the peak positions of 0.71 and 6.40 keV as L alpha, K alpha signals, respectively. In addition oxygen and nitrogen were evident at the peak position of 0.53 keV as K alpha signal and of 0.39 keV as K alpha signal, respectively in Figure 3.5.

The physical properties of ION-chitosan composites from the N_2 adsorption-desorption data are summarized in Table 3.6. The ION-chitosan composites had the BET specific surface area of 2.395 m^2/g, total pore volume of 0.012 cm^3/g, mesopore volume of 0.012 cm^3/g and micropore volume of 0.001 cm^3/g.
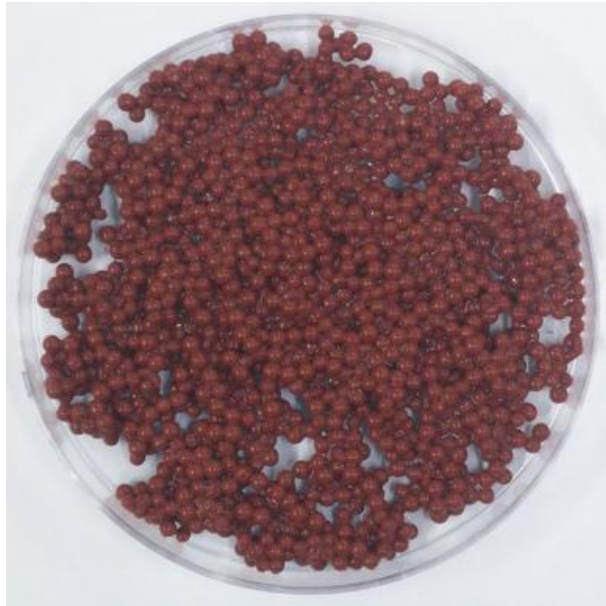
Figure 3.3 Digital image of ION-chitosan composites.

(a)

SE MAG: 109 x HV: 10.0 kV WD: 8.1 mm   600 µm

(b)

SE MAG: 149 x HV: 10.0 kV WD: 8.1 mm   400 µm
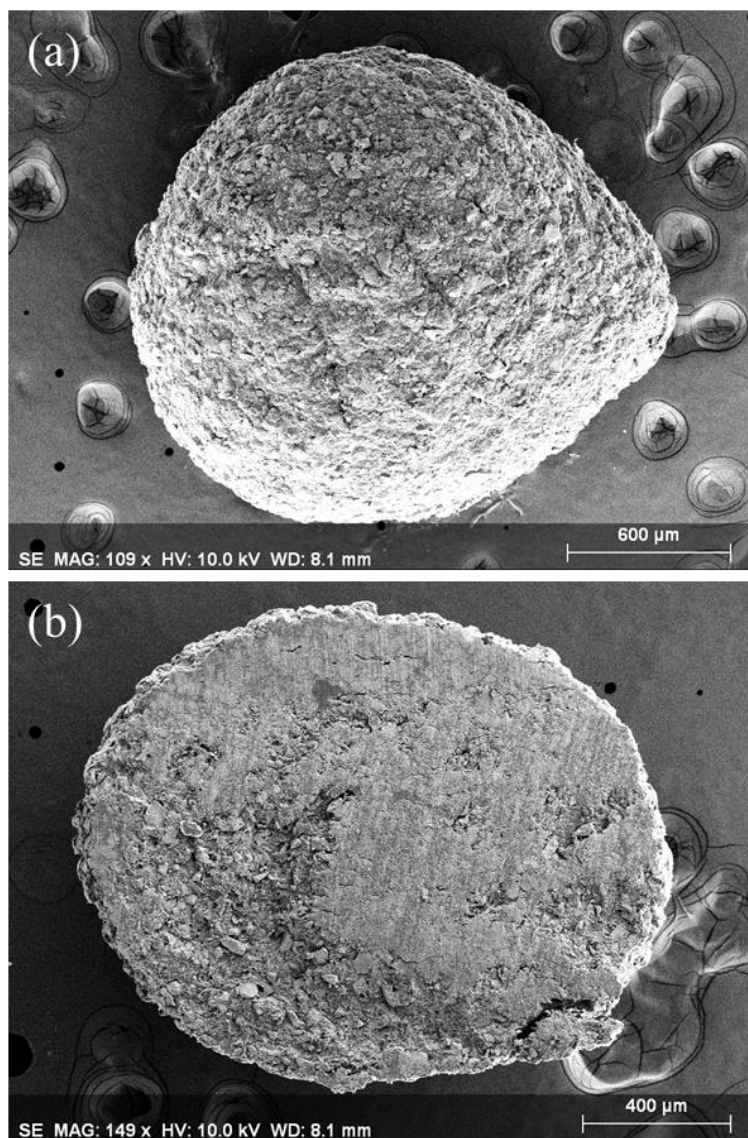
Figure 3.4 Field emission scanning electron microscope (FESEM)
images of ION-chitosan composite: (a) surface area; (b) cross section
area.

Element	C norm. [wt.%]	C Atom. [wt.%]
Iron	41.76	15.26
Oxygen	33.52	42.76
Nitrogen	24.72	41.99
Total:	100.00	100.00
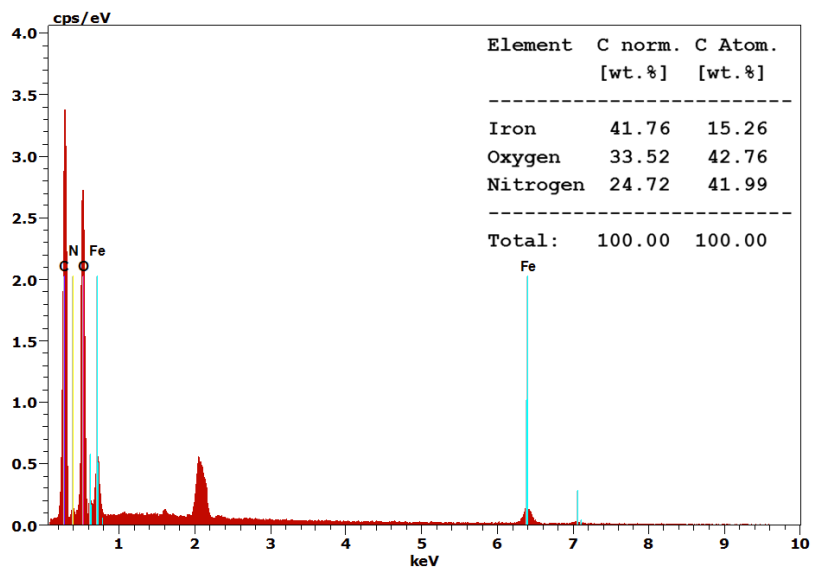
Figure 3.5 Energy dispersive X-ray spectrometer (EDS) pattern of ION-chitosan composite.

Table 3.6 Physical characteristics of ION-chitosan composite obtained from the N_2 adsorption–desorption data.

Characteristics	Value	Unit
Brunauer–Emmett–Teller (BET) analysis		
Monolayer volume (V_m)	0.6	cm^3/g
BET specific surface area ($a_{s,BET}$)	2.4	m^2/g
BET constant	51.1	-
Total pore volume (V_p)	0.012	cm^3/g
Average pore diameter ($d_{p,ave}$)	19.3	nm
Barrett–Joyner–Halenda (BJH) analysis		
Mesopore volume ($V_{p,me}$)	0.012	cm^3/g
Peak diameter of mesopore ($d_{p,me}$)	32.3	nm
Horvath–Kawazoe (HK) analysis		
Micropore volume ($V_{p,mi}$)	0.001	cm^3/g
Peak diameter of micropore ($d_{p,mi}$)	1.2	nm

3.2.2. Batch adsorption of phosphate

The phosphate removal by the ION-chitosan composites as a function of adsorbent dose (initial P concentration = 1, 2, 4, 8 mgP/L; adsorbent dose = 5 – 50 g/L; reaction time = 12 h) is shown in Figure 3.6. The percent removal increased with a rise in the adsorbent dose from 5 to 50 g/L. When the initial P concentration was 2 mgP/L, the percent removal was 48.9% at the ION-chitosan composites dose of 5 g/L and 100% at a dose of 50 g/L. The sorption capacity decreased with increasing adsorbent dose from 5 to 50 g/L. When the initial P concentration was 2 mgP/L, the sorption capacity was 0.18 mgP/g at 5 g/L, and then decreased to 0.09 mgP/g at 20 g/L. The sorption capacity decreased to 0.05 mgP/g at 40 g/L, decreasing further to 0.04 mgP/g at 50 g/L.

The effect of the initial solution pH on phosphate removal by ION-chitosan composites (initial phosphate concentration = 2 mgP/L; adsorbent dose = 30 g/L; reaction time = 12 h) is shown in Figure 3.7. The sorption capacity at pH 5.02 was 0.046 mgP/g and remained at 0.044 – 0.046 mgP/g up to pH 9.03. The results indicate that phosphate removal was relatively stable over acidic and alkaline pHs.

The effect of the reaction time on phosphate removal by ION-chitosan composites (initial P concentration = 1, 2, 4, 8 mgP/L; adsorbent dose = 30 g/L) is shown in Figure 3.8. At an initial P concentration of 1 mgP/L, the sorption capacity gradually increased, reaching 0.03 mgP/g after a reaction time of 12 h. As the initial P concentration was increased from 1 to 8 mgP/L, the sorption capacity at 12 h increased from 0.03 to 0.15 mgP/g.

46
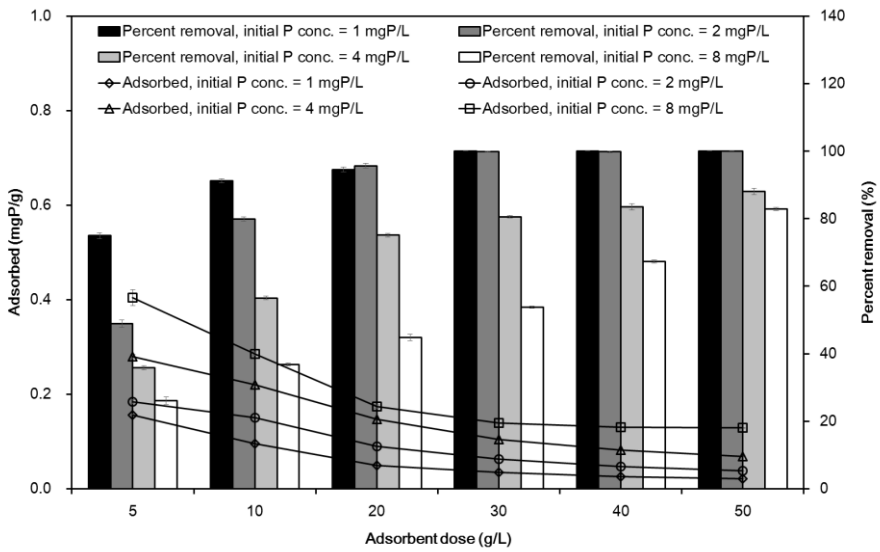
Figure 3.6 Effect of ION-chitosan composite dose on removal of phosphate.
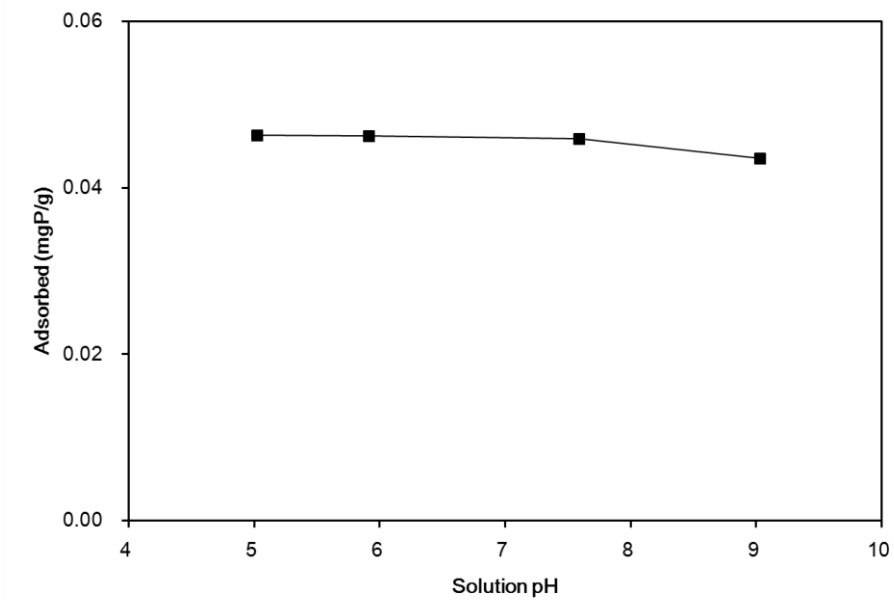
Figure 3.7 Effect of solution pH on phosphate removal by ION-chitosan composites (adsorbent dose = 30 g/L; initial concentration = 2 mgP/L).
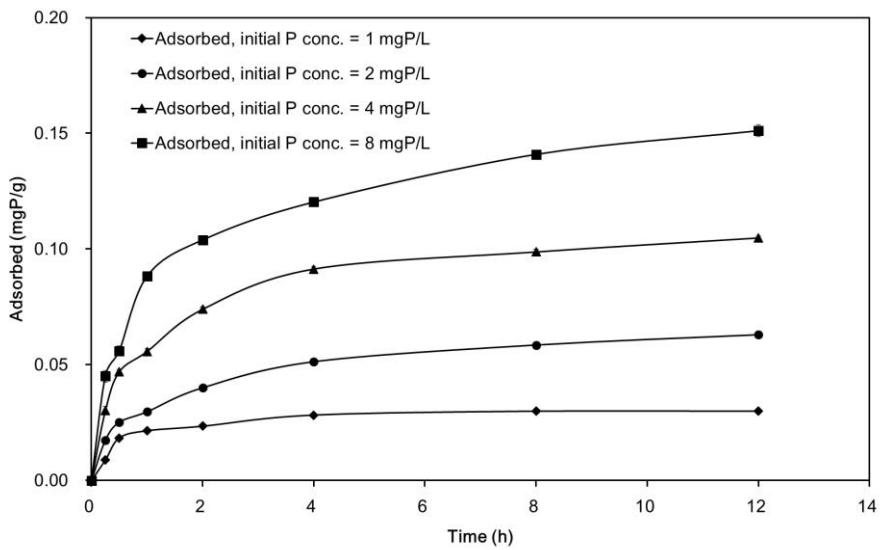
Figure 3.8 Phosphate removal by ION-chitosan composite as a function of reaction time (adsorbent dose = 30 g/L).

The effect of reaction temperature on the removal of phosphate by ION-chitosan composites (initial P concentration = 2 mgP/L; adsorbent dose = 30 g/L) is presented in Figure 3.9. The sorption capacity was increased with increasing reaction temperature. At 15°C, the sorption capacity was 0.057 mgP/g with a percent removal of 88.1%. When the temperature was raised to 30°C, the sorption capacity increased to 0.063 mgP/g with an increase in the percent removal to 99.8%. At 45°C, the sorption capacity slightly increased to 0.064 mgP/g with the percent removal reaching 100%. These results demonstrated that the phosphate removal process was endothermic.

The effect of the initial phosphate concentration on phosphate removal by ION-chitosan composites (adsorbent dose = 5, 10, 20, 30 g/L; reaction time = 12 h) is presented in Figure 3.10. The percent removal decreased with a rise in the initial phosphate concentration at all ION-chitosan composites dosages. At a dose of 5 g/L, the percent removal decreased from 71.3 to 18.8% with an increase in the initial phosphate concentration from 1 to 20 mgP/L. For a 20 g/L dose, the percent removal decreased from 94.3 to 26.2% over the same phosphate concentration range. In the case of a 30 g/L dose, the percent removal was 99.8% at initial phosphate concentration of 1 mgP/L, but decreased 32.8% at initial phosphate concentration of 20 mgP/L. Meanwhile, the sorption capacity increased with a rise in the initial phosphate concentration at all dosages. For example, the sorption capacity at 30 g/L increased from 0.03 to 0.22 mgP/g as the initial phosphate concentration was increased from 1 to 20 mgP/L.
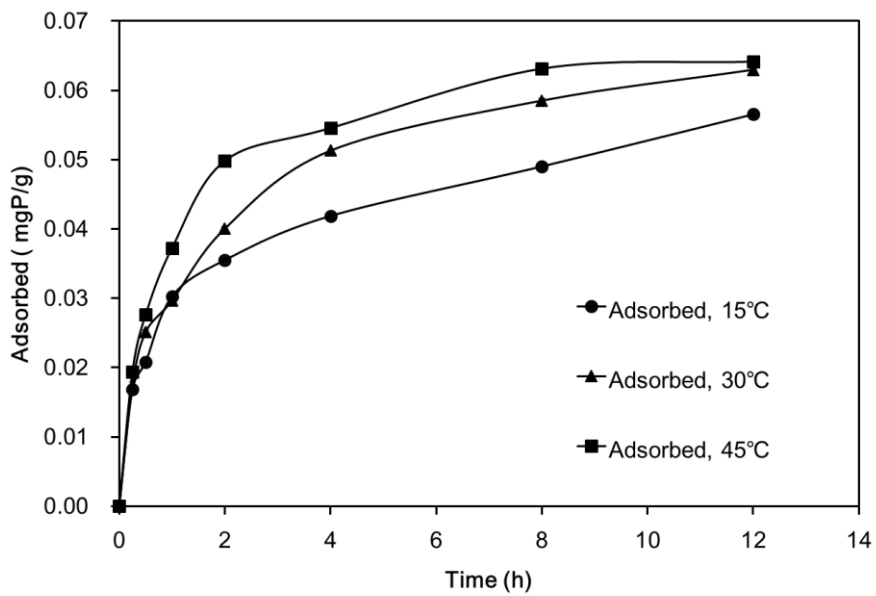
Figure 3.9 Effect of reaction temperature on phosphate removal by ION-chitosan composite (adsorbent dose = 30 g/L; initial concentration = 2 mgP/L).
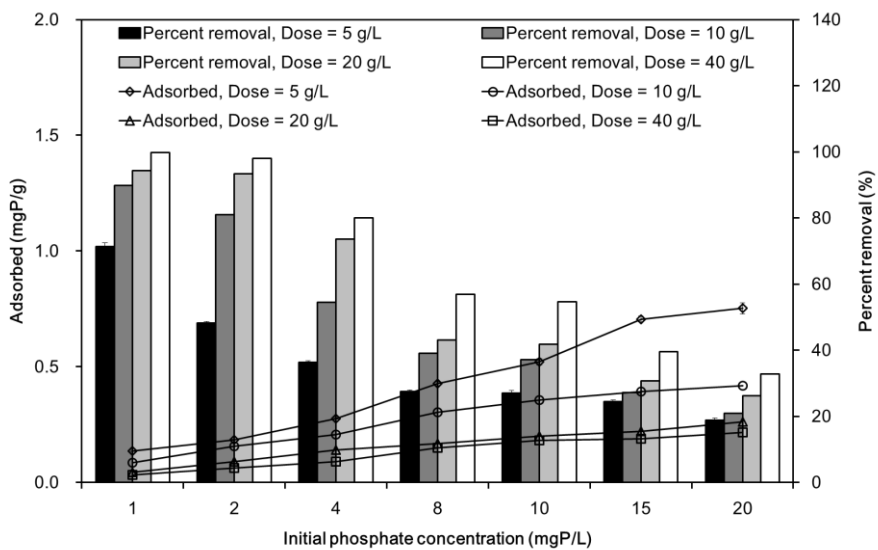
Figure 3.10 Phosphate removal by ION-chitosan composite as a function of initial concentration (reaction time = 12 h).

Effect of desorption and reuse on phosphate removal by ION-chitosan composites (initial P concentration = 2 mgP/L; adsorbent dose = 30 g/L; reaction time = 12 h) is presented Figure 3.11. In the first adsorption, the sorption capacity was determined to be 0.057 mgP/g and remained constant or slightly decreased at $0.056 - 0.057$ mgP/g for six cycles. The recovery rate was reduced from 70.3 to 49.3% with increasing the number of repeated use from 1 to 6.
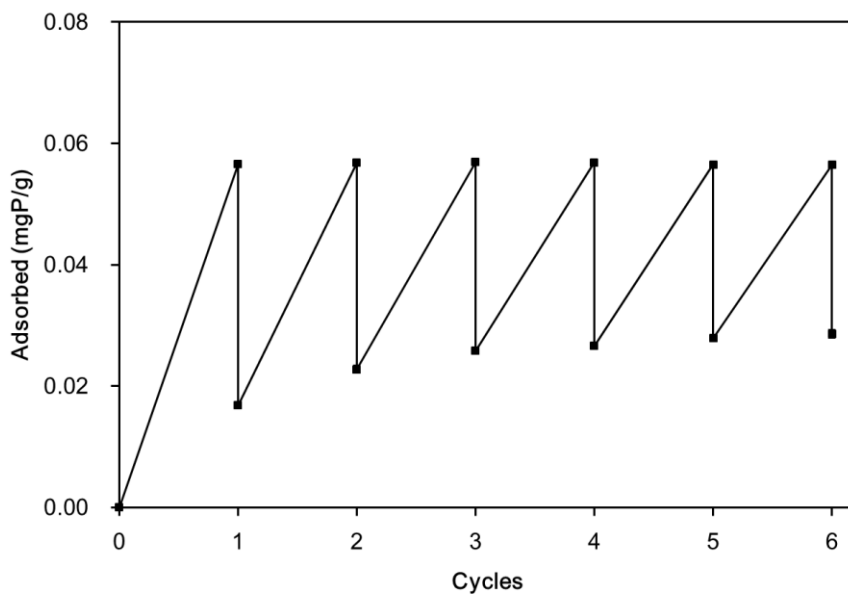
Figure 3.11 Effect of desorption and reuse on phosphate removal by ION-chitosan composites (adsorbent dose = 30 g/L; initial concentration = 2 mgP/L).

3.2.3. Kinetic, isotherm and thermodynamic model analyses

The results from the kinetic model analyses are presented in Figure 3.12, while the kinetic model parameters are provided in Table 3.7. From the obtained values of R^2, χ^2, and SAE, it was concluded that the Elovich model was most suitable for describing the kinetic data (Figure 3.12(c)), except when the initial P concentration was 1 mgP/L (pseudo second-order model). This finding indicates that chemisorption is involved in the adsorption of phosphate to ION-chitosan composites. The Elovich model has been applied in the adsorption of surfactant, organic acids, and dyes onto loofah fiber embedded chitosan beads (Chang and Juang, 2005), in the adsorption of Pb(II) and methylene blue onto chitosan/Fe-hydroxyapatite beads (Saber-Samandari *et al.*, 2014), and in the adsorption of fluoride onto the Fe_3O_4-chitosan composite (Mohseni-Bandpi *et al.*, 2015).

The Elovich equation describes predominantly chemical adsorption on highly heterogeneous adsorbents, but the equation does not propose definite diffusion mechanism for the interaction between adsorbate and adsorbent (Aksakal and Ucun, 2010). Thus the intra-particle diffusion model proposed by Weber and Morris (1963) is used to investigate the mechanism of adsorption.

The intra-particle diffusion model applied to the data is shown in Figure 3.13, indicating that the plots were composed of three line segments. The first line in the plot indicates the diffusion of solute through the solution to the external surface of adsorbent, or the boundary layer diffusion of solute molecules. The second portion described the

gradual adsorption stage, where in intra-particle diffusion was rate limiting. In some cases, the third line exists, which is the final equilibrium stage for which the intra-particle diffusion started to slow down due to the extremely low solute concentration left in the solution (Cheung *et al*., 2007; Tan *et al*., 2007).

The intra-particle diffusion model parameters are provided in Table 3.8. Weber and Morris reported that if the plot of q_t as a function of $t^{0.5}$ exhibits linearity and passes through the origin, the only rate-limiting process is the intra-particle diffusion. In Figure 3.13 and Table 3.8, the plots do not pass through the origin and exhibited multi-linearity, which indicated that intra-particle diffusion was not the only rate controlling step, and the mechanism involves simultaneous adsorption and intra-particle diffusion (Jiang *et al*., 2013).
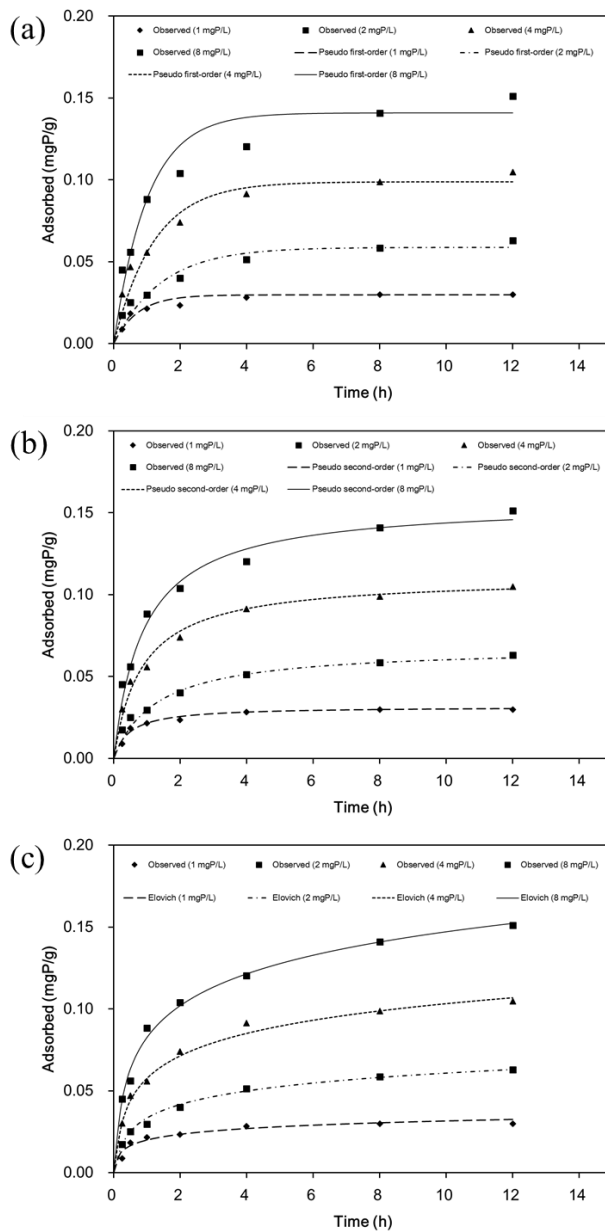
Figure 3.12 Kinetic model fits for phosphate removal to ION composites: (a) pseudo first-order model; (b) pseudo second-order model; (c) Elovich model.

Table 3.7 Kinetic model parameters obtained from model fitting to ION-chitosan composites experimental data.

Initial conc. (mgP/L)	Pseudo first-order model				
	q_e (mgP/g)	k_1 (1/h)	R^2	χ^2	SAE
1	0.030	1.397	0.925	0.002	0.011
2	0.059	0.703	0.951	0.011	0.028
4	0.099	0.829	0.964	0.014	0.041
8	0.141	0.983	0.930	0.012	0.061

Initial conc. (mgP/L)	Pseudo second-order model				
	q_e (mgP/g)	k_2 (g/mgP/h)	R^2	χ^2	SAE
1	0.032	67.622	0.964	0.001	0.007
2	0.068	11.405	0.985	0.006	0.015
4	0.111	10.665	0.986	0.002	0.022
8	0.157	7.094	0.981	0.005	0.034

Initial conc. (mgP/L)	Elovich model				
	α (mgP/g/h)	β (g/mgP)	R^2	χ^2	SAE
1	0.260	197.597	0.912	0.002	0.012
2	0.196	83.910	0.991	0.001	0.008
4	0.362	50.513	0.989	0.001	0.016
8	0.532	35.635	0.991	0.001	0.018
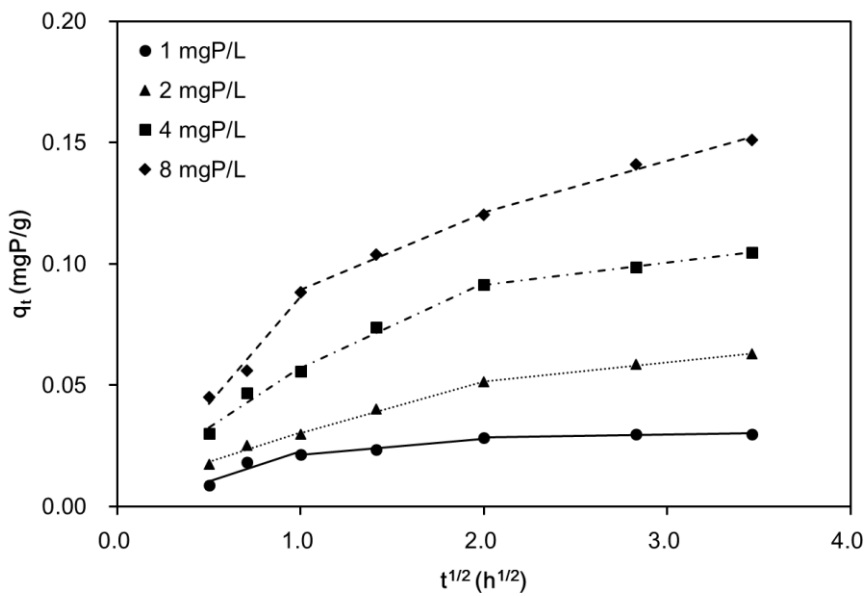
Figure 3.13 Intra-particle diffusion model for phosphate removal to ION-chitosan composites.

Table 3.8 Intra-particle diffusion model parameters obtained from model fitting to ION-chitosan composites experimental data.

Initial P concentration	1 mgP/L	2 mgP/L	4 mgP/L	8 mgP/L
$k_{i,\ 1}$ (mg/g/h$^{0.5}$)	0.024	0.024	0.050	0.088
I	0.000	0.006	0.008	0.000
R^2	0.860	0.940	0.925	0.968
$k_{i,\ 2}$ (mg/g/h$^{0.5}$)	0.007	0.021	0.035	0.032
I	0.014	0.009	0.022	0.057
R^2	0.981	0.994	0.988	0.992
$k_{i,\ 3}$ (mg/g/h$^{0.5}$)	0.001	0.008	0.009	0.021
I	0.026	0.035	0.073	0.079
R^2	0.813	0.996	1.000	0.987

The results of thermodynamic analysis are shown in Figure 3.14, and thermodynamic parameters are provided in Table 3.9. The positive value of $\Delta H°$ (487.30 kJ/mol) indicates that phosphate removal by ION-chitosan composites is an endothermic process, while the positive value of $\Delta S°$ (1692.35 J/K/mol) suggests that the degree of randomness increased at the interface between the solid and solution during the removal process. The negative values of $\Delta G°$ (-0.37 to -51.14 kJ/mol) indicate that the phosphate removal process was spontaneous.

The equilibrium isotherm model analyses are presented in Figure 3.15, while the corresponding equilibrium model parameters are provided in Table 3.10. The values of R^2, χ^2, and *SAE* indicated that both the Redlich–Peterson isotherms and the Freundlich isotherms were more suitable at describing the equilibrium data than Langmuir isotherm. The Redlich–Peterson model can be reduced to the Freundlich model when the first term in the denominator(=1) was negligible except for small values of $a_R C_e{}^g$. In the Redlich–Peterson model, parameter values of K_R/a_R (0.120 – 0.188) corresponded well to the values of K_F (0.119 – 0.186) in Freundlich model. In addition, the values of (1 - g) (0.212 – 0.499) in the Redlich-Peterson model are almost equivalent to the values of $1/n$ (0.216 – 0.502) in Freundlich model.

From the Langmuir model, the maximum adsorption capacity was 1.08 mgP/g under the given experimental conditions (adsorbent dose = 5 g/L; initial P concentration = 1 – 20 mgP/L; reaction time = 12 h). This value was within the range of the phosphate removal capacity of iron oxides (0.42 – 4.18 mgP/g) reported in the literature (Table 3.11) (Zhu *et al*., 2013; Huang, 2004; Barber, 2002).
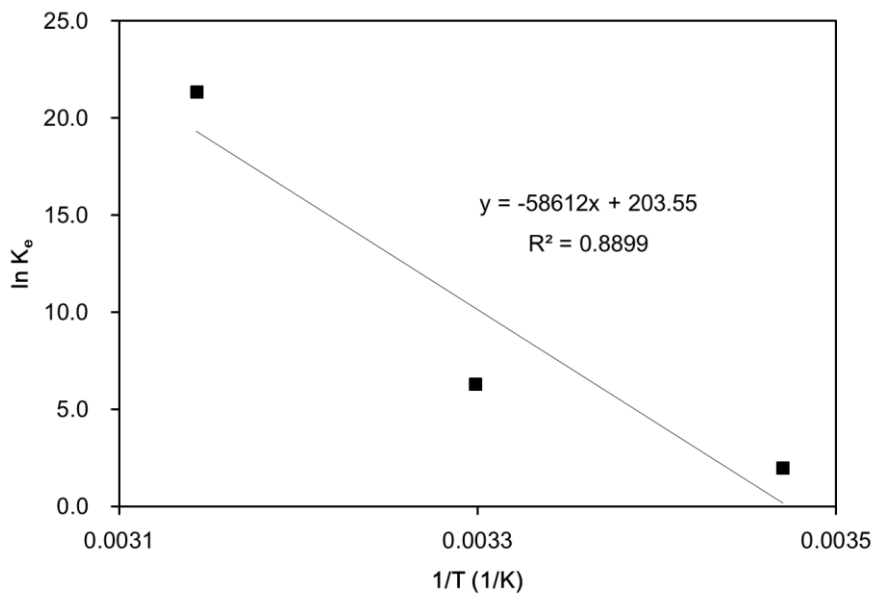
Figure 3.14 Thermodynamic analysis for phosphate adsorption to ION-chitosan composites.

Table 3.9 Thermodynamic parameters for phosphate adsorption to ION-chitosan composites.

Temp. (°C)	$\Delta H°$ (kJ/mol)	$\Delta S°$ (J/K/mol)	$\Delta G°$ (kJ/mol)
15	487.30	1692.35	-0.37
30			-25.76
45			-51.14
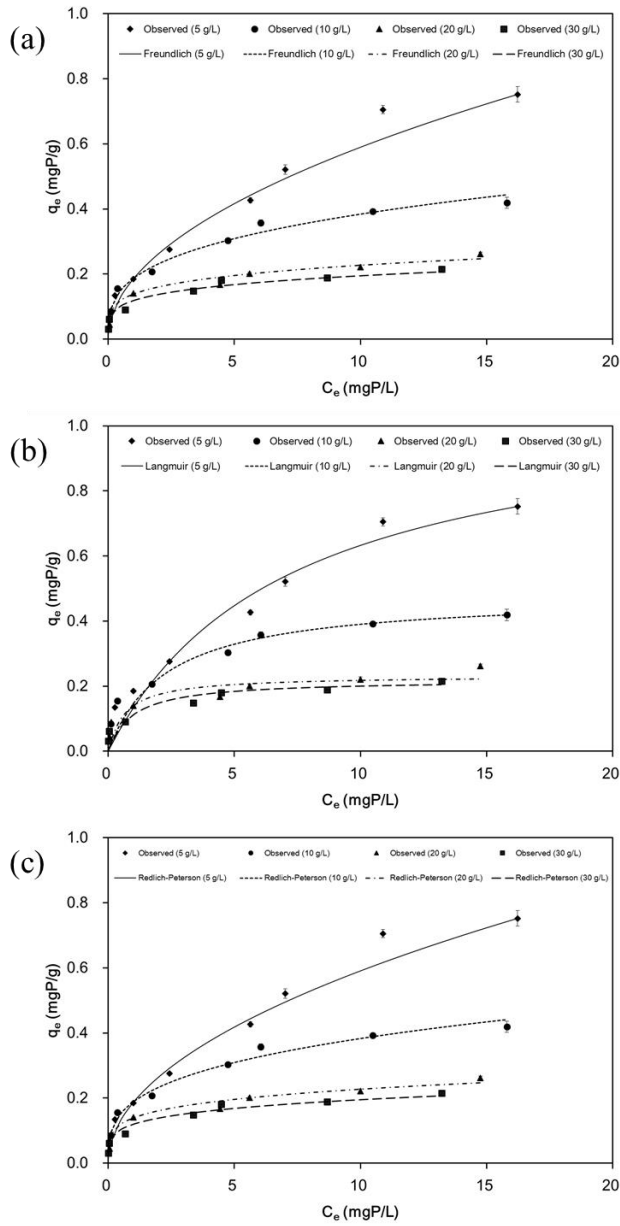
Figure 3.15 Equilibrium isotherm model fits for phosphate removal to ION-chitosan composites: (a) Freundlich model; (b) Langmuir model; (c) Redlich-Peterson model.

Table 3.10 Equilibrium isotherm model parameters obtained from model fitting to ION-chitosan composites experimental data.

Dose (g/L)	Freundlich model				
	K_F (L/g)	1/n	R^2	χ^2	SAE
5	0.186	0.502	0.977	0.031	0.184
10	0.186	0.315	0.980	0.688	0.095
20	0.138	0.216	0.968	3.127	0.076
40	0.119	0.216	0.977	4.984	0.053

Dose (g/L)	Langmuir model				
	Q_m (mgP/g)	K_L (L/mgP)	R^2	χ^2	SAE
5	1.079	0.142	0.970	0.256	0.267
10	0.480	0.438	0.971	1.548	0.185
20	0.233	1.506	0.891	4.563	0.163
40	0.220	1.035	0.950	48.463	0.126

Dose (g/L)	Redlich-Peterson model					
	K_R (L/g)	a_R (L/mgP)	g	R^2	χ^2	SAE
5	273.509	1459.002	0.501	0.977	0.030	0.186
10	399.378	2127.299	0.691	0.980	0.694	0.095
20	534.167	3848.731	0.786	0.968	3.129	0.076
40	1008.582	8423.473	0.788	0.976	4.944	0.053

Table 3.11 Comparison of adsorption capacity of various iron oxides for phosphate removal.

Adsorbent	Concentration (mgP/L)	Capacity (mgP/g)	Reference
α-Fe_2O_3/Fe_3O_4/C composite	2 – 50	1.81	Zhu *et al*., 2013
Magnetite (natural)	0.3 – 46.5	0.42	Barber, 2002
Magnetite (synthetic)	0.3 – 46.5	1.06	Barber, 2002
Hematite	3 – 20	0.57	Huang, 2004
ION-chitosan composite	1 – 20	1.08	This study

3.2.4. Fixed-bed adsorption of phosphate

Breakthrough curves (BTCs) obtained from the fixed-bed experiments are shown in Figure 3.16. The results of the column experiments are provided in Table 3.12. To investigate the effect of flow rate on BTC of phosphate adsorption, 2 mgP/L of phosphate was fixed as the influent concentration, and the flow rates were 8.18 and 16.36 mL/min. With increasing flow rate from 8.18 mL/min (experiment 2) to 16.36 mL/min (experiment 1), Steeper BTC was observed. As the flow rate increases, the contact time between the phosphate and the filter medium decreases. EBCT decreased from 6 min (experiment 2) to 3 min (experiment 1) as the flow rate was increased (column length = 10 cm). As the flow rate increases, the BTC becomes steeper because the driving forces increase, leading to a decrease in the adsorption zone length (Han *et al*., 2008). The adsorption of phosphate is given more time to contact with filter medium at a lower flow rate which may result in the higher adsorption efficiency of phosphate in the column (Xu *et al*., 2009). Increasing the flow rate decreased the phosphate adsorption capacity from 0.124 mgP/g (experiment 2) to 0.049 mgP/g (experiment 1).

The phosphate removal in the synthetic solution (experiment 4) was higher than that in the stream water (experiment 2). The phosphate adsorption capacity in the synthetic solution was 0.184 mgP/g, whereas the phosphate adsorption capacity in the stream water was 0.124 mgP/g. The commonly occurring anions, including Cl^-, NO_3^-, HCO_3^-, and SO_4^{2-}, are present with phosphate in stream water (Table 3.1). They are supposed to compete with phosphate for active sites of adsorbent (Chen *et al*., 2015).

To investigate the effect of bed height on phosphate removal BTCs obtained by varying the bed heights from 10 to 20 cm at 8.18 mL/min of flow rate and 2 mgP/L of influent concentration. With increasing column length from 10 cm (experiment 2) to 20 cm (experiment 5), phosphate adsorption capacity and exhaustion time increased. The longer column length leads to more dispersed BTCs, that is, increasing the column length broadens the mass-transfer zone, resulting in a decrease of the BTC slope (Han *et al.*, 2008). With increasing column length, the phosphate adsorption capacity increased from 0.124 mgP/g (experiment 2) to 0.143 mgP/g (experiment 5).

The regenerated ION-chitosan composites were examined for phosphate adsorption to compare their performances with those of the pristine ones. When the column length is 10cm, phosphate adsorption capacity of pristine ION-chitosan composites was 0.124 mgP/g (experiment 2) and regenerated composites had 0.113 mgP/g (experiment 3) of adsorption capacity. In addition, when the column length is 20cm, phosphate adsorption capacity of pristine composites was 0.143 mgP/g (experiment 5) and regenerated composites had 0.113 mgP/g (experiment 6) of adsorption capacity. There were loss of 9 and 6% in the phosphate adsorption capacity of ION-chitosan composites after regeneration for 10 and 20 cm column, respectively.
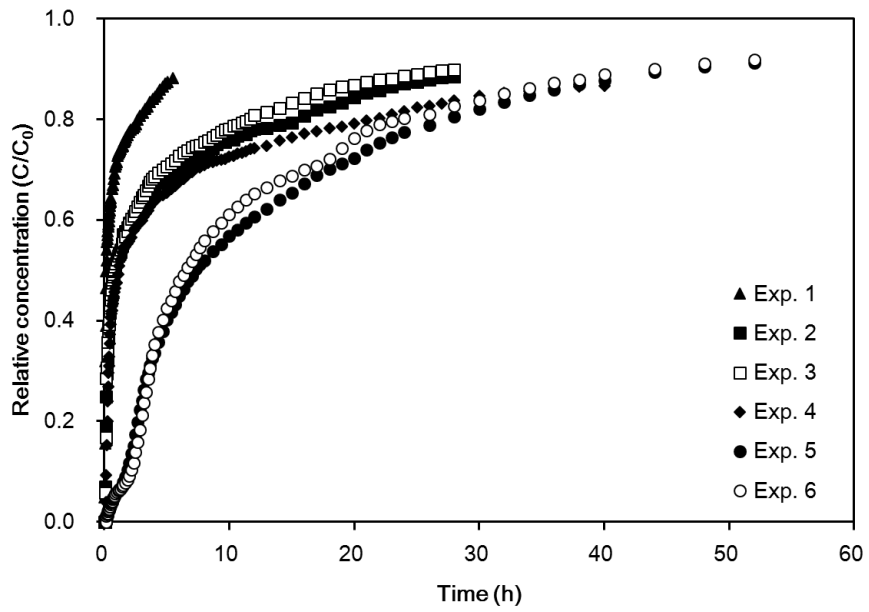
Figure 3.16 Breakthrough curves of phosphate obtained from the fixed-bed experiments.

Table 3.12 Results from column experiments for the phosphate sorption to ION-chitosan composites.

Ex.	m_{total} (mgP)	q_{total} (mgP)	Re (%)	q_{eq} (mgP/g)
1	10.51	2.40	22.83	0.049
2	25.56	5.99	23.45	0.124
3	25.72	5.46	21.22	0.113
4	38.05	8.94	23.50	0.184
5	48.19	13.84	28.72	0.143
6	48.44	13.01	26.87	0.134

3.2.5. Pilot test

The results from long-term pilot-scale adsorption tower experiment are shown in Figure 3.17. Flow rate, inlet tower pressure, T-P concentration, pH, and DO was monitored at influent and effluent during overall pilot-scale experiment (Table 3.13). The inlet tower pressure gradually increased for 33 days (Figure 3.17(a)). On the first day , the tower inlet pressure was 0.19 kg/cm^2 and increased to 0.30 kg/cm^2 on 6 days later. The inlet tower pressure was 0.45 kg/cm^2 on 20 days later and further increased to 0.60 kg/cm^2 on 33 days later. Increased column pressure might cause reduction in the solute average velocity. However, the flow rate remained at 6.56 – 7.58 L/min during the same period.

On 15 days later, T-P removal efficient was 60.0% and T-P concentration of effluent was 0.01 mgP/L. On 30 days later, T-P removal efficient was 70.9% and remained 72.4% on 33 days later. T-P concentration of effluent remained under 0.035 mP/L which can cause eutrophication (Figure 3.17(b)). During that time period, removal efficient of T-P was 51.79±16.74%.

Both of influent and effluent pH values remained constantly neutral (pH 6.7 – 7.7) (Figure 3.17(c)). DO concentration of effluent was 8.4 mg/L on the 1st day and decreased to 3.6 mg/L on the 7th. It increased to 9.0 mg/L on 13rd day and remained 5.8 – 9.9 mg/L until 33 days later.
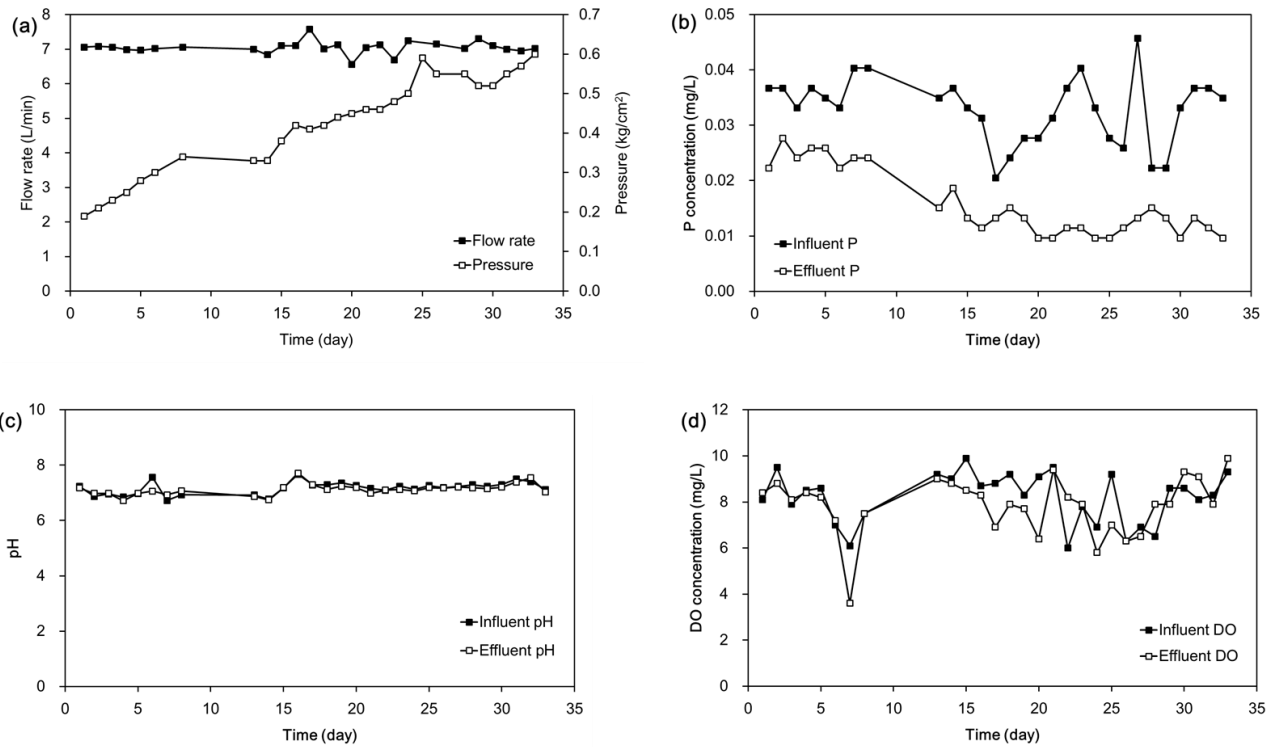
Figure 3.17 Experimental results from long-term pilot-scale column experiment for the phosphate sorption to ION-chitosan composites: (a) flow rate and pressure; (b) T-P concentration; (c) pH; (d) DO.

Table 3.13 Experimental results for long-term pilot-scale adsorption tower experiment.

	DO (mg/L)	pH	T-P (mg/L)	Flow rate (L/min)	Pressure (kg/cm^2)
Influent	6.0 – 9.9	6.7 – 7.7	0.020 – 0.046		
				6.6 – 7.6	0.19 – 0.60
Effluent	3.6 – 9.9	6.7 – 7.7	0.010 – 0.028		

3.2.6. Conclusions

The removal of phosphate by ION-chitosan composites was examined in this chapter. Kinetic experiment indicated that phosphate adsorption by the composite reached equilibrium at 12 h. The results demonstrated that the ION-chitosan composites were effectively remove phosphate with the maximum capacity of 1.08 mgP/g. The phosphate removal was relatively stable over acidic and alkaline pHs. The composites were regenerated six cycles and sorption capacity was remained almost constant. Whereas recovery rate was decreased to 49.3% after six cycles of regeneration.

The column experiments showed that the adsorption capacities of ION-chitosan composites were in the range of 0.05 – 0.18 mgP/g in the given experimental conditions. Cl^-, NO_3^-, HCO_3^-, SO_4^{2-} in stream water prevented phosphate adsorption onto ION-chitosan composites. The regenerated ION-chitosan composites showed slight decrease in phosphate uptake.

In pilot test, T-P concentration of effluent in adsorption tower experiment remained under 0.035 mgP/L for 33 days. ION-chitosan composites were stable under natural environmental conditions. Furthermore, solution pH did not change significantly after adsorption.

These results demonstrated that ION-chitosan composites could be applied as efficient and eco-friendly adsorbents for phosphate adsorption from water.

Chapter 4 Preparation and characterization of triamine-functionalized mesoporous silica-polymer composites for Cr(VI) removal from industrial plating wastewater

Several researchers have reported some amine functionalized mesoporous silicas for removal of heavy metal cations and organic pollutants from wastewater (Shahbazi *et al*., 2011; Aguado *et al*., 2009; Heidari *et al*., 2009; Sayari *et al*., 2005). By dispersion of amine-functionalized mesoporous silica in strong acid, amino groups can be converted ammonium salts (Yoshitake *et al*., 2002b). Protonated amine molecules can act as strong anion adsorption sites. In previous studies amine functionalized mesoporous silica was usually used for adsorbents as powdered form. A few studies have reported protonated amine functionalized mesoporous silica for removal of anions from water (Yoshitake *et al*., 2002b). The aims of this chapter were development of the adsorbent had a high adsorption density and good stability. In this study, amine functionalized mesoporous silica was protonated by strong acid solution. In addition, granular type of composite containing amine functionalized mesoporous silica was synthesized for removal of Cr(VI) from industrial plating wastewater.

4.1. Materials and Methods

4.1.1. Synthesis of DAEAPTS-SBA-15 PVA/alginate composites

All chemicals used for the experiments were purchased from Sigma Aldrich. Mesoporous silica SBA-15 was prepared according to Zhao *et al*. (1998). At first, 6 g of Pluronic P123 and 1 g of cetyltrimethyl-ammonium bromide (CTAB, ≥99%) were dissolved in mixed solution

of 80 mL of deionized water(Direct-Q, Millopore), 50 mL of ethanol (≥94%), and 100 mL of 2 M HCl (37%). After stirring at 30 ℃ for 1 h, 20 mL of tetraethylorthosilicate (TEOS, ≥99%) was added into the solution, and stirred for 45 min at 40 ℃. Then, the solution was aged at 80 ℃ for 24 h under refluxing condition. The resultants were filtered and washed with deionized water, and dried under ambient conditions. Finally, the dried powder was calcined at 550 ℃ for 6 h using an electric muffle furnace (C-FMA, Vision Lab, Seoul, Korea) to remove the surfactant.

DAEAPTS grafted SBA-15 was prepared according to Mittal *et al.* (2015). At first, 0.5 g of calcined SBA-15 was dissolved and dispersed in 150 mL of anhydrous toluene and stirred for 30 min at room temperature. Then, 0.2 mL of deionized water was added to the above mixture and continuously stirred at room temperature for 2 h. The temperature of the mixture was then increased and maintained at 100 ℃ and 4 g of N'-(3-trimethoxysilylpropyl)diethylenetriamine (DAEAPTS) was added to it. The mixture was kept under vigorous stirring and reflux for 24 h. The resultant slurry was washed first with toluene and then hexane and finally dried at 70 ℃ overnight. The obtained material was dispersed in 0.1 M HCl solution for 6 h and dried at 70 ℃ for overnight.

DAEAPTS-SBA-15 PVA/alginate composites were prepared according to Han *et al.* (2012). 20 g of polyvinyl alcohol (PVA) and 2 g of sodium alginate were dissolved in 200 mL of deionized water and agitated on a magnetic stirrer at 70 ℃ for 5 h. Then, 16 g of DAEAPTS grafted SBA-15 was added to the above mixture under intensive stirring

to obtain the homogeneous suspension. was filled in plastic syringe and then dropped into mixed solution of 5% boric acid and 1% $CaCl_2$ using a syringe pump (78-1100I, Fisher Scientific) at 4 mL/min. The suspension droplets formed beads instantaneous in the solution, and were remained in the aqueous solution for 24 h. Then, the composites were oven-dried at 70 °C for 18 h in an electric muffle furnace (C-FMA, Vision Lab, Korea).

4.1.2. Characterization of DAEAPTS-SBA-15 PVA/alginate composites

Field emission scanning electron microscopy (FESEM) analysis and energy dispersive X-ray spectrometry (EDS) analysis were performed using a field emission scanning electron microscope (Supra 55VP; Carl Zeiss, Oberkochen, Germany). TEM (JEM-1010, JEOL, Tokyo, Japan) was used to take images of the particles. The particle size was determined by the analysis of the TEM image (number of particle = 100) using ImageJ 1.43u software (National Institutes of Health, Bethesda, MD, USA). N_2 adsorption-desorption experiments were performed using a surface area analyzer (BELSORP-max, BEL Japan Inc., Japan) after the sample was pretreated at 120 ºC. From the N_2 adsorption-desorption isotherms, the specific surface area, average pore diameter, total pore volume, and mesopore volume were determined using Brunauer-Emmett-Teller (BET), Barrett-Joyner-Halenda (BJH), and Horvath-Kawazoe (HK) analyses with an ASAP 2010 instrument (Micromeritics,

Nocross, Georgia, USA).XPS (XPS Sigma Probe, Thermo VG, UK) measurement was performed with monochromatic Al Kα radiation.

4.1.3. Industrial plating wastewaters

The industrial plating wastewaters were collected from two wastewater treatment plants located in the Banwol Jungang Plating Industry Cooperative (Ansan, Korea). The plating wastewater was passed through a 0.45 μm filter prior to the experiments in order to remove suspended particles. The ionic composition of the plating wastewaters were analyzed using ion chromatograph (ICS-3000; Dionex, USA), and inductively coupled plasma-atomic emission spectroscopy (ICP-AES) (Optima-4300, Perkin-Elmer, Waltham, Massachusetts, USA). Table 4.1 was shows the characteristics of the plating wastewater samples.
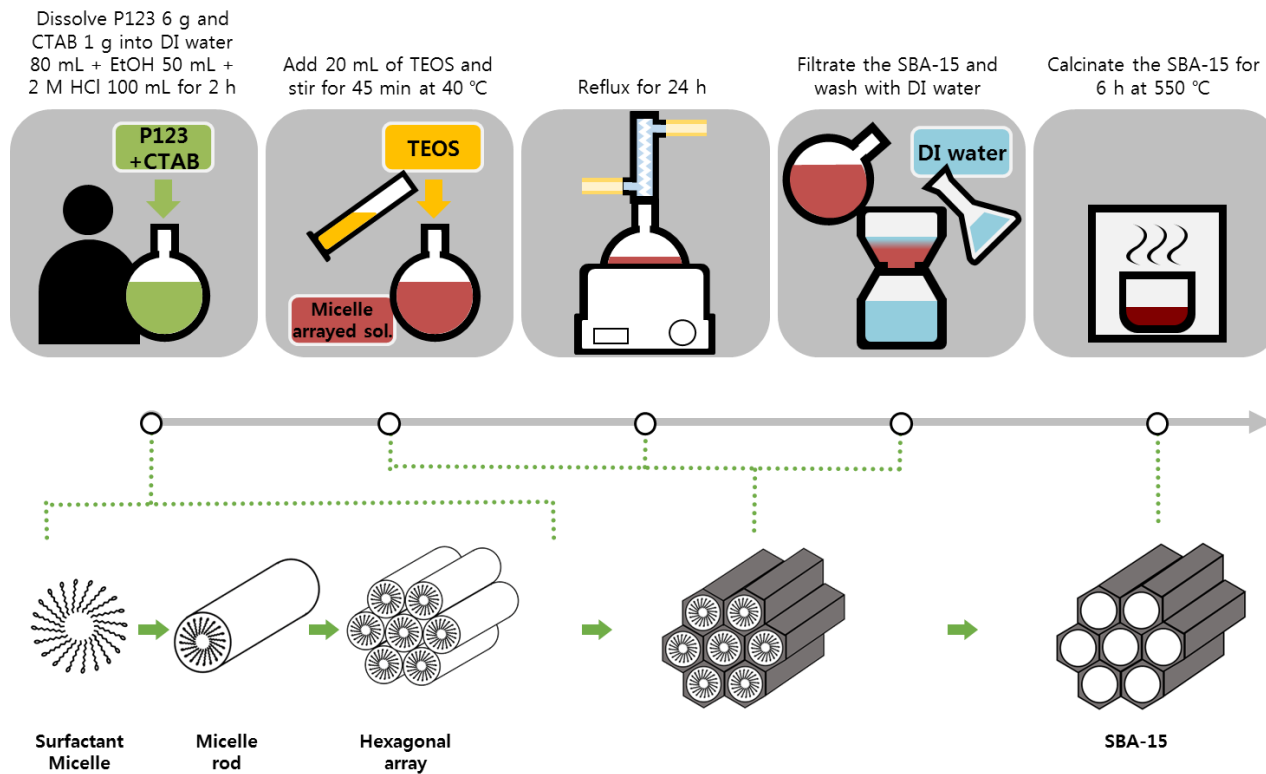
Figure 4.1 Schematic diagram for synthesis of mesoporous silica.
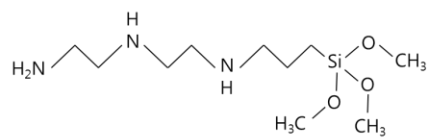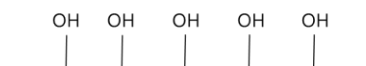
80
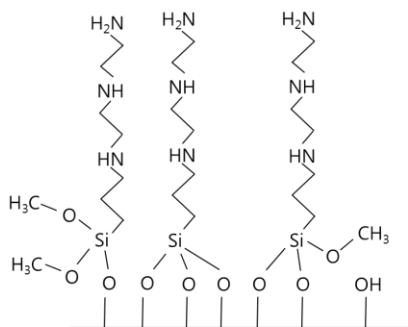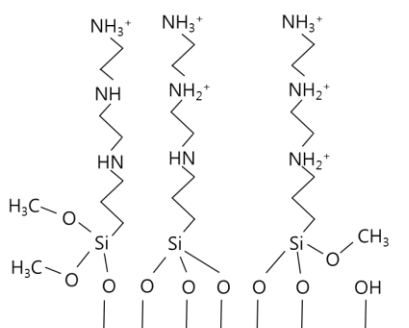
Figure 4.2 Schematic diagram for synthesis of DAEAPTS-SBA-15
(Mittal *et al*., 2015).

Table 4.1 Characteristics of industrial plating wastewater samples.

	Wastewater 1	Wastewater 2
Cr (mg/L)	2692.8	412.4
Cd (mg/L)	N.D	N.D
Cu (mg/L)	185.6	42.9
Pb (mg/L)	0.129	0.496
Zn (mg/L)	1.3	1.1
Ni (mg/L)	0.8	68.8
As (mg/L)	N.D	N.D
Mn (mg/L)	1.195	0.095
Fe (mg/L)	166.1	2.1
F (mg/L)	N.D	53.4
Cl (mg/L)	N.D	263.8
NO_3 (mg/L)	N.D	62.3
SO_4 (mg/L)	211.14	6575.6
pH	1.72	1.13
IS (mS/cm)	11.8	29.5

4.1.4. Batch experiments

Chromate removal by DAEAPTS-SBA-15 was conducted under batch conditions. The desired chromate (Cr(VI)) solution was prepared by diluting the stock solution (1,000 mg/L) that had been made from potassium dichromate ($K_2Cr_2O_7$). The batch experiments were performed at 30 ^{o}C using 50 mL polypropylene conical tubes, unless otherwise stated. All of the batch experiments were performed in triplicate.

The first set of experiments were examined Cr(VI) removal as a function of initial solution pH (adsorbent dose = 1 g/L; initial Cr(VI) concentration = 100 mg/L); 0.1 M NaOH and 0.1 M HCl solutions were used to adjust the pH of the reaction solution from 2.0 to 12.0, and the pH was measured by a pH probe (9107BN, Thermo Scientific, USA). The tubes were shaken at 100 rpm using a shaking incubator (Daihan Science, Seoul, Korea). After 24 h, the samples were collected and filtered through a 0.45 µm membrane filter. The chromate concentration was analyzed using the 1,5-diphenyl carbazide method(US EPA 7196A, 1992). The chromate concentrations were measured at a wavelength of 540 nm using a UV–vis spectrophotometer (Helios, Thermo Scientific, Waltham, MA, USA).

The second set of experiments performed at the different dosages of adsorbent ranging from 0.1 to 3.0 g/L in 30 mL solution (initial Cr(VI) concentration = 100 mg/L; solution pH = 3).

The third set of experiments was performed as a function of reaction time (adsorbent dose = 1 g/L; initial Cr(VI) concentration = 100 mg/L ; solution pH = 3). The additional experiments were performed at 15 and

45 ^{o}C to examine the effect of temperature on Cr(VI) removal.

The fourth set of experiments was conducted as a function of the initial Cr(VI) concentration. DAEAPTS-SBA-15 were added to 30 mL of chromate solution (adsorbent dose = 1 g/L; initial concentration = 10 – 1,000 mg/L ; solution pH = 3), and the samples were collected 4 h later.

Table 4.2 Batch experimental conditions for the chromate sorption to DAEAPTS-SBA-15.

	Dose (g/L)	Reaction Time (h)	Initial conc. (mg/L)	Solution pH	Temperature (°C)	Solution volume (mL)
Effect of solution pH	1	24	100	2.0 – 12.0	30	30
Effect of dosage	0.1 – 3.0	24	100	3	30	30
Effect of reaction time	1	4	100	3	15 – 45	30
Effect of initial concentration	1	4	10 – 1,000	3	30	30

4.1.5. Fixed-bed column experiments

Column experiments were performed using a plexiglas column (inner diameter = 2.5 cm; column length = 10 cm) packed with DAEAPTS-SBA-15 PVA/alginate composites. For column experiments, a column was packed for each experiment with DAEAPTS-SBA-15 PVA/alginate composites by the tap-fill method. Prior to the experiments, the packed column was flushed upward using a connected peristaltic pump (QG400, Fluid Metering Inc., Syosset, NY, USA) for 20 pore volumes of deionized water until steady state flow conditions were established. Then, the industrial plating wastewaters were introduced downward into the packed column at the same flow rate in a step injection mode. Portions of the effluent were collected using an autocollector (Retriever 500, Teledyne, City of Industry, CA, USA) at regular intervals.

The effluent pH was measured with a pH probe (9107BN, Thermo Scientific, Waltham, MA, USA) and the electrical conductivity (EC) was measured with an EC probe (815PDL, Istek, Korea). After the column reached exhaustion, DAEAPTS-SBA-15 PVA/alginate composites were dispersed in 0.1 M NaOH solution for 20 min to desorb the chromium from the composites. The experimental conditions are provided in Table 4.3.

Table 4.3 Fixed-bed column experimental conditions for the chromium sorption to DAEAPTS-SBA-15 PVA/alginate composite.

Ex.	Plating wastewater	Adsorbent	Initial conc. (mg/L)	Linear velocity (cm/min)	Flow rate (mL/min)	Bed depth (cm)	Bed volume (cm^3)	EBCT (min)	Pore volume (cm^3)	Mass of adsorbent (g)	pH$_{effluent}$	EC$_{effluent}$ (mS/cm)
1	Wastewater 1	Pristine	2692.8	0.1	0.5	10	49.09	98.17	13.25	25.07	3.04±0.28	2.96±0.81
2	Wastewater 2	Pristine	412.4	0.1	0.5	10	49.09	98.17	13.25	25.07	1.69±0.10	19.10±3.55
3	Wastewater 1	Regenerated	2692.8	0.1	0.5	10	49.09	98.17	13.25	25.07	3.12±0.30	3.13±0.40

4.2. Results and Discussion

4.2.1. Characteristics of DAEAPTS-SBA-15

Figure 4.1 shows TEM images of SBA-15 and DAEAPTS-SBA-15. Nano-sized pores were observed regardless of surface functionalization. However, since acidic treatment pores were partly blocked by oxygen and nitrogen (Figure 4.3(b)). The EDS pattern of DAEAPTS-SBA-15 (Figure 4.4) demonstrates that silicon (Si) was the major element. In the EDS pattern, nitrogen (N) appeared due to the surface functionalization. In the EDS analysis, Si was evident at the peak position of 1.740 keV as K alpha X-ray signal, while N was found at the peak position of 0.392 keV as K alpha X-ray signal.

N_2 adsorption and desorption isotherms are presented in Table 4.4. The pore volume and the surface area of the DAEAPTS-SBA-15 significantly decrease as compared with those of SBA-15. This indicates the successful binding of the organic silane on the pore surface of SBA-15. According to the BET analysis the particles had the specific surface areas of SBA-15 and DAEAPTS-SBA-15 are 891.3 m^2/g and 14.1 m^2/g respectively. The average pore diameters of SBA-15 decreased from 5.9 nm to 3.1 nm after grafting of DAEAPTS.

Figure 4.5 – 4.7 shows XPS analyses of SBA-15 and DAEAPTS-SBA-15. In the Si2p spectrum, the peak around 101.9 and 103.6 eV was assigned from SiO2 from SBA-15 (He *et al*., 1992; Mirji *et al*., 2007) (Figure 4.5(b)). In the O1s spectrum, the peak at 531.20 and 533.16 eV was contributed from Si-O-Si and Si-OH of SBA-15 (Mohai *et al*., 1990; Police *et al*., 2015) (Figure 4.5(c)). The N1s peak at 399.7 eV (main peak)

and 401.9 eV (small shoulder) were contributed from protonated and H-bonded amines (Stegall *et al*., 2016) (Figure 4.6(b)). The peaks at 587.4 and 577.8 eV are correspond to Cr 2p1/2 and Cr 2p3/2 of Cr(III) which means that adsorbed Cr(VI) has been transformed into Cr(III) state (Kim *et al*., 2013) (Figure 4.7(c)). After adsorbed onto adsorption, Cr(VI) interacted with electron on the mesoporous silica surface, resulting in the reduction and partly release of Cr(III). Due to oxidative treatment for amino-group was coated onto mesoporous silica surface. The negatively charged Cr(VI) was adsorbed onto the surface rapidly by electron attraction. Then, the reduction reaction occurred (Sun *et al*., 2013).
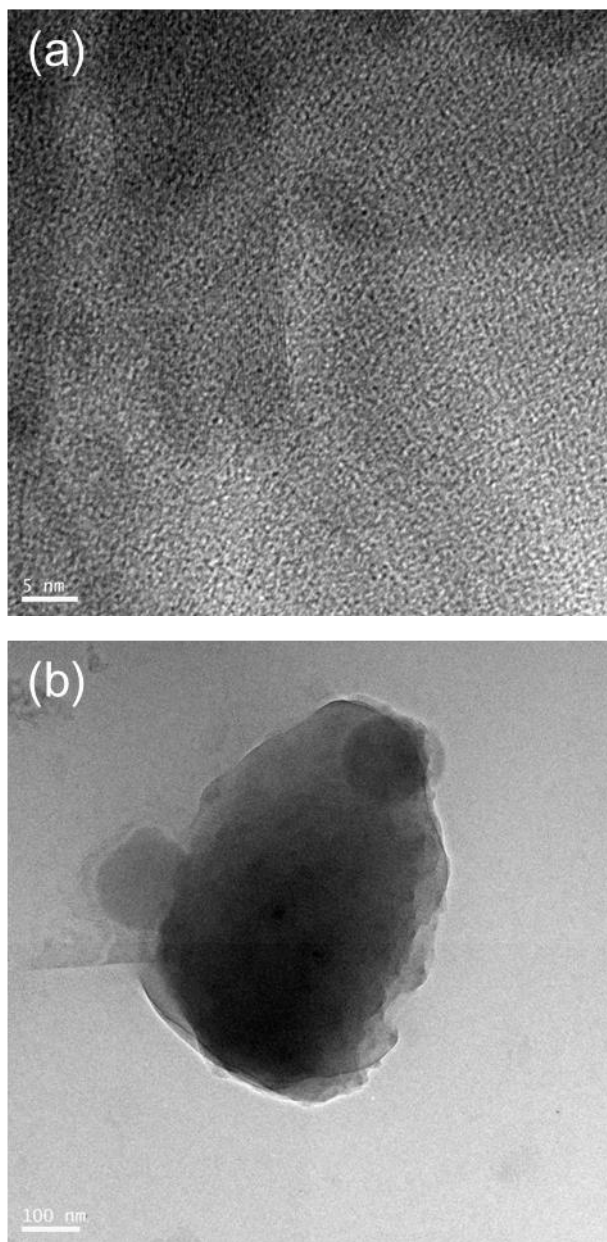
Figure 4.3 Transmission electron microscopy (TEM) images: (a) SBA-15 (bar = 5 nm); (b) DAEAPTS-SBA-15 (bar = 100 nm).
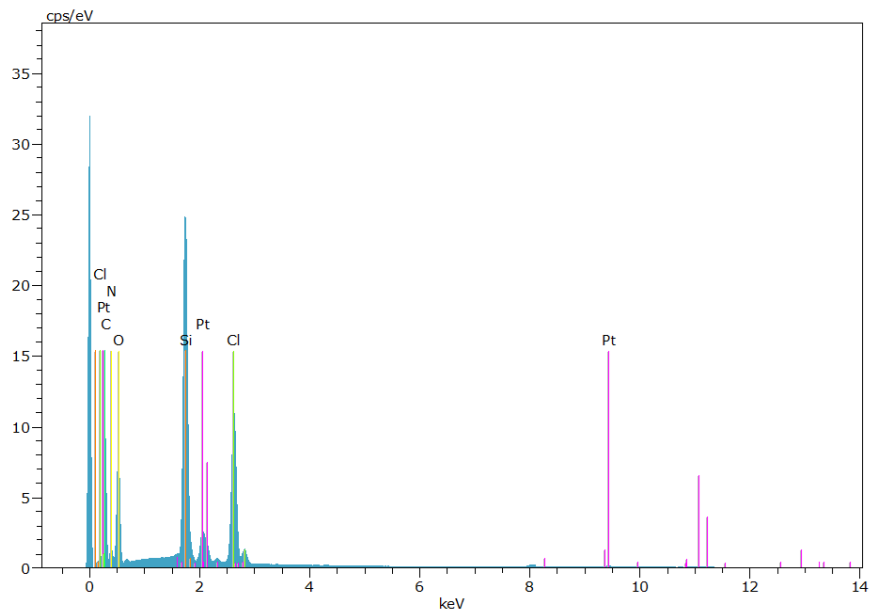
Figure 4.4 EDS pattern of DAEAPTS-SBA-15.

Table 4.4 Physical characteristics of SBA-15 and DAEAPTS-SBA-15 obtained from the N_2 adsorption–desorption data.

Characteristics	SBA-15	DAEAPTS-SBA-15	Unit
Brunauer–Emmett–Teller (BET) analysis			
Monolayer volume (V_m)	204.8	3.2	cm^3/g
BET specific surface area ($a_{s,BET}$)	891.3	14.1	m^2/g
BET constant	106.0	50.0	-
Total pore volume (V_p)	1.3	0.011	cm^3/g
Average pore diameter ($d_{p,ave}$)	5.9	3.1	nm
Barrett–Joyner–Halenda (BJH) analysis			
Mesopore volume ($V_{p,me}$)	1.3	0.009	cm^3/g
Peak diameter of mesopore ($d_{p,me}$)	6.3	3.3	nm
Horvath–Kawazoe (HK) analysis			
Micropore volume ($V_{p,mi}$)	52.1	0.8	cm^3/g
Peak diameter of micropore ($d_{p,mi}$)	0.6	1.1	nm
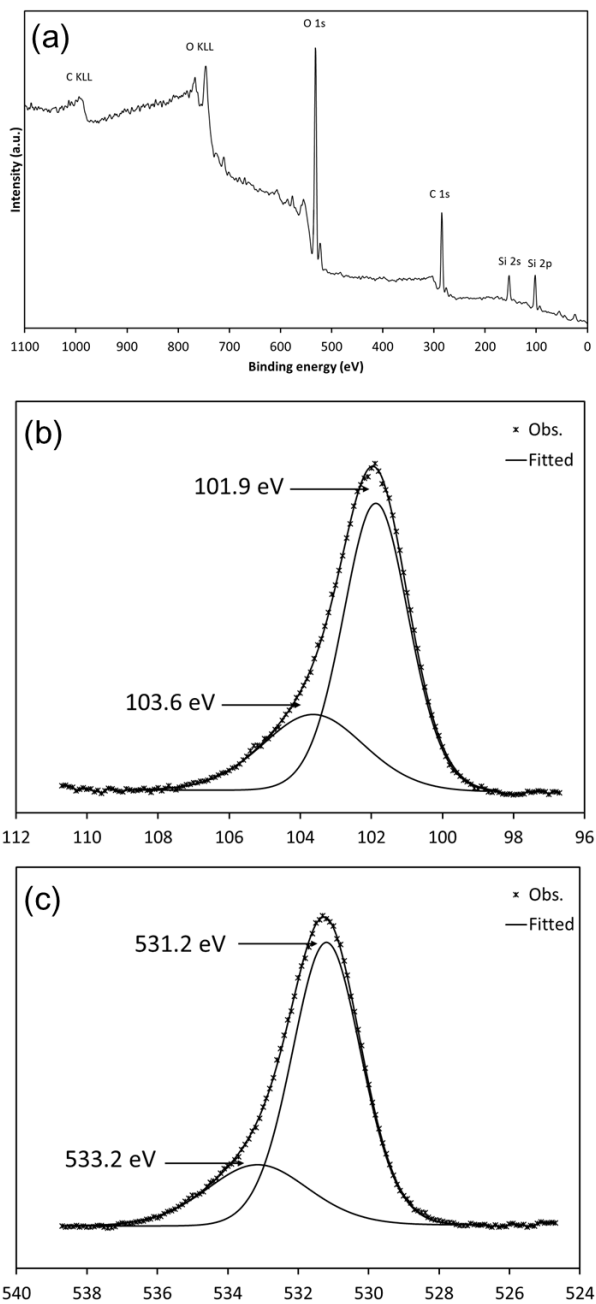
Figure 4.5 X-ray photoelectron spectroscopy (XPS) spectra of SBA-15: (a) wide scan; (b) high-resolution scan of the Si 2p region; (c) high-resolution scan of the O 1s region.
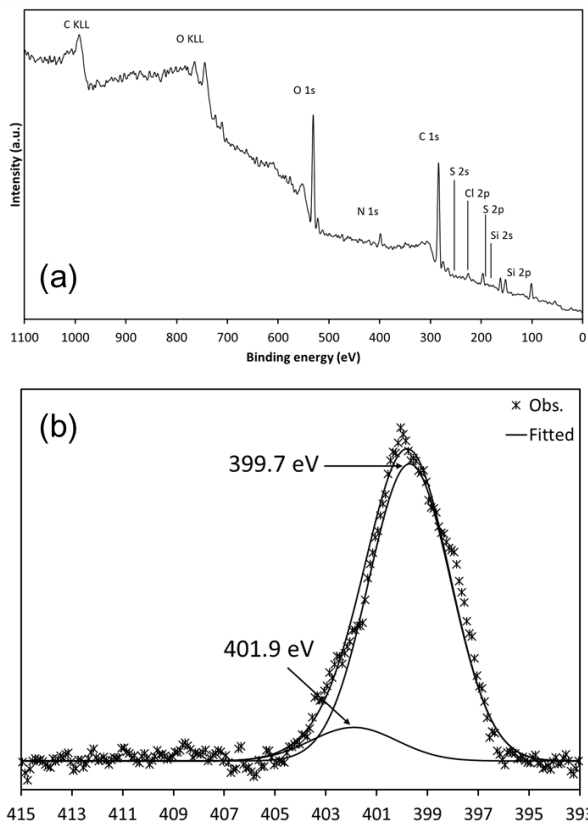
Figure 4.6 X-ray photoelectron spectroscopy (XPS) spectra of
DAEAPTS-SBA-15 before Cr(VI) sorption experiments: (a) wide scan;
(b) high-resolution scan of the N 1s region.
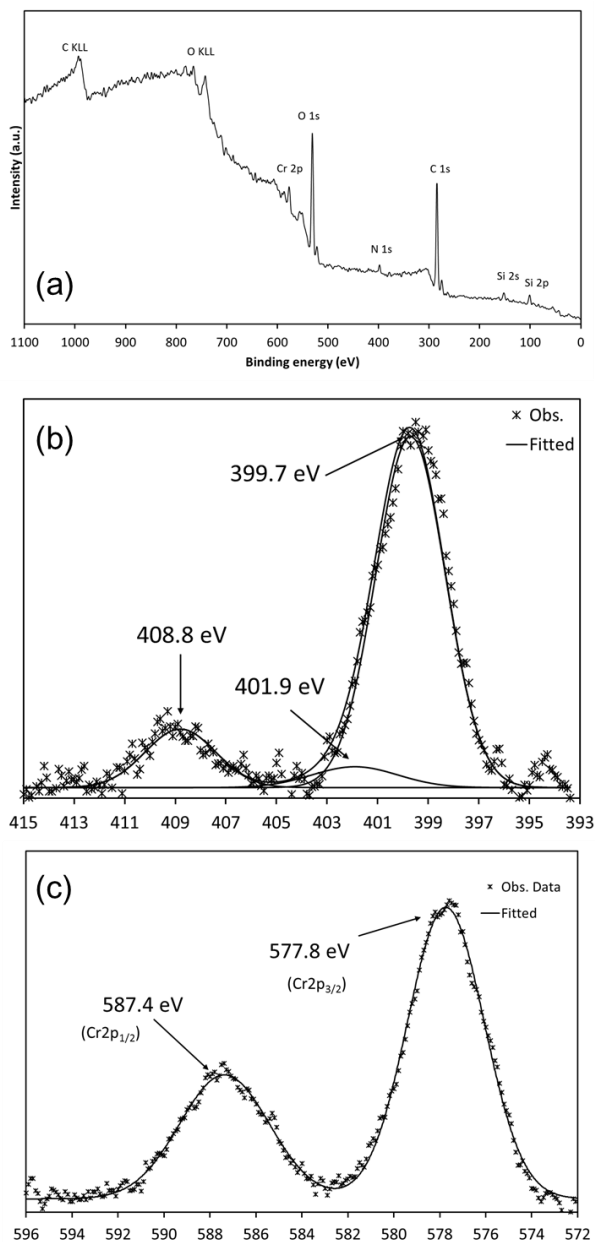
Figure 4.7 X-ray photoelectron spectroscopy (XPS) spectra of DAEAPTS-SBA-15 after Cr(VI) sorption experiments: (a) wide scan; (b) high-resolution scan of the N 1s region; (c) high-resolution scan of the Cr 2p region.

The digital image of DAEAPTS-SBA-15 PVA/alginate composites are presented in Figure 4.8. The composites had a sphere shape with a particle size of 1.13±0.09 mm. The FESEM images of DAEAPTS-SBA-15 PVA/alginate composite are presented in Figure 4.9. It demonstrated that the cross-sectional surface of DAEAPTS-SBA-15 PVA/alginate composite was heterogeneous in surface topography. The EDS pattern demonstrated that silocon (Si), oxygen (O), carbon (C), chlorine (Cl), calcium (Ca), and nitrogen (N) were the major elements of the DAEAPTS-SBA-15 PVA/alginate composite (Figure 4.10).

The physical properties of DAEAPTS-SBA-15 PVA/alginate composites from the N_2 adsorption-desorption data are summarized in Table 4.5. The DAEAPTS-SBA-15 PVA/alginate composites had the BET specific surface area of 0.806 m^2/g, total pore volume of 0.044 cm^3/g, mesopore volume of 0.044 cm^3/g and micropore volume of 0.187 cm^3/g.
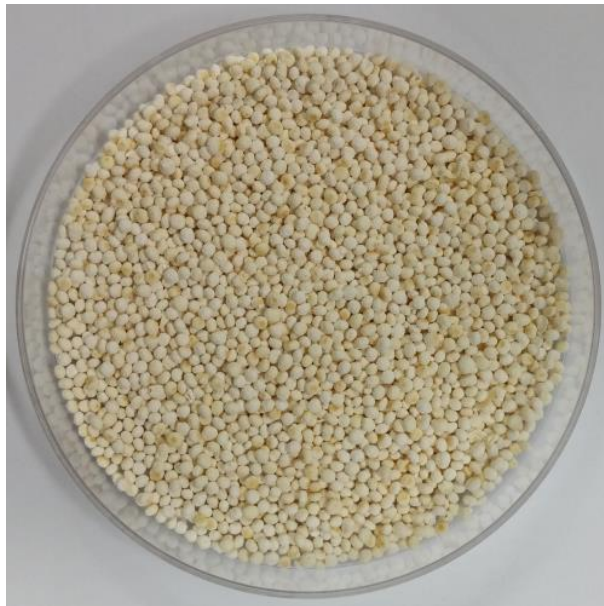
Figure 4.8 Digital image of DAEAPTS-SBA-15 PVA/alginate composites.
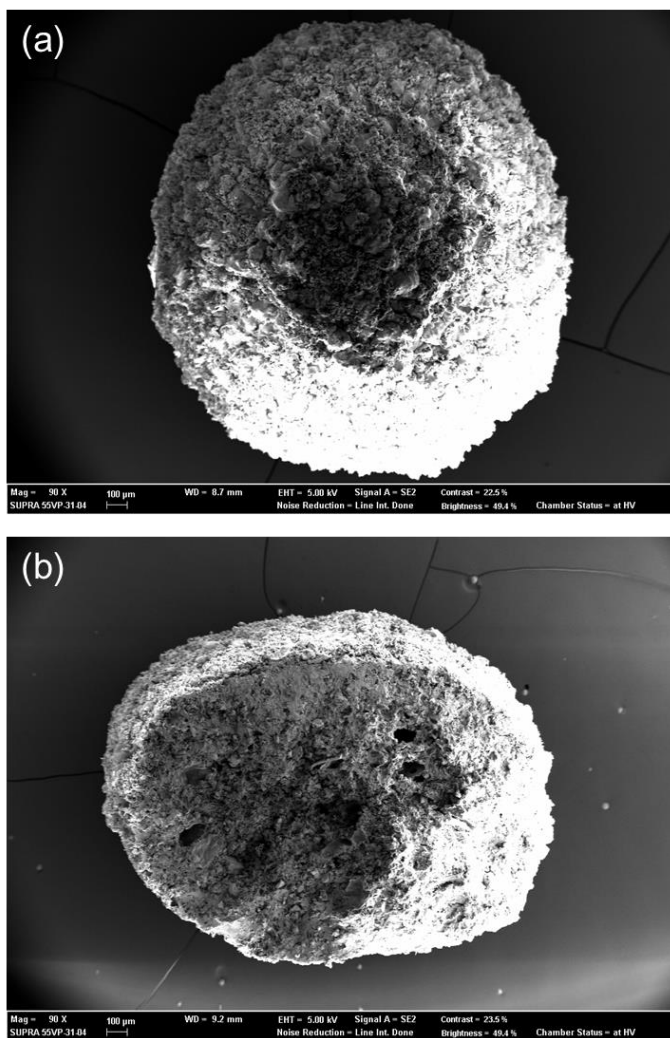
Figure 4.9 Field emission scanning electron microscope (FESEM) images of DAEAPTS-SBA-15 PVA/alginate composite: (a) surface area; (b) cross section area.
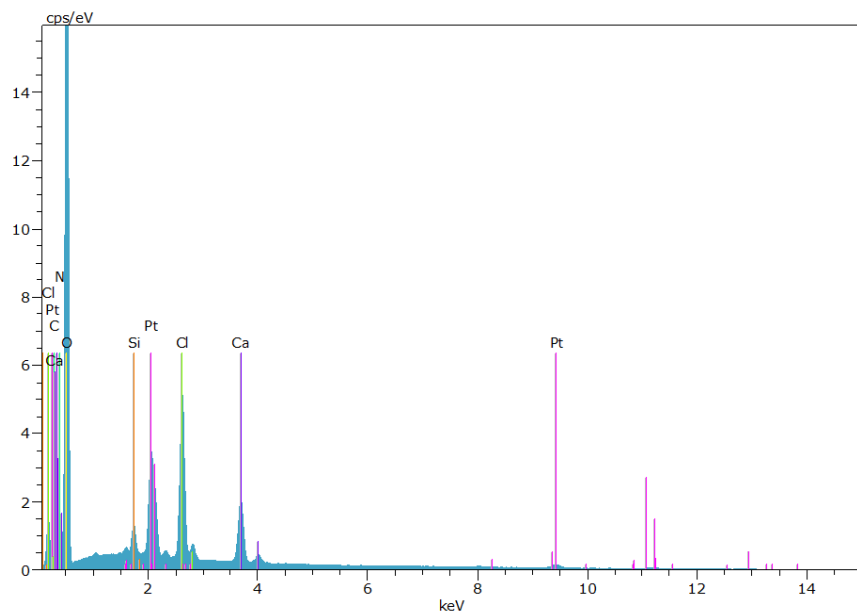
Figure 4.10 EDS pattern of DAEAPTS-SBA-15 PVA/alginate composite.

Table 4.5 Physical characteristics of DAEAPTS-SBA-15 PVA/alginate composites obtained from the N_2 adsorption–desorption data.

Characteristics	Value	Unit
Brunauer–Emmett–Teller (BET) analysis		
Monolayer volume (V_m)	0.8	cm^3/g
BET specific surface area ($a_{s,BET}$)	3.5	m^2/g
BET constant	66.6	-
Total pore volume (V_p)	0.044	cm^3/g
Average pore diameter ($d_{p,ave}$)	50.1	nm
Barrett–Joyner–Halenda (BJH) analysis		
Mesopore volume ($V_{p,me}$)	0.044	cm^3/g
Peak diameter of mesopore ($d_{p,me}$)	140.0	nm
Horvath–Kawazoe (HK) analysis		
Micropore volume ($V_{p,mi}$)	0.2	cm^3/g
Peak diameter of micropore ($d_{p,mi}$)	1.2	nm

4.2.2. Batch experiments

In this study, Cr(VI) was not adsorbed on unfunctionalized SBA-15. It is considered that the positively charged amino group is indispensable to the adsorption of Cr(VI) (Yoshitake *et al*., 2002a).

The effect of initial solution pH on Cr(VI) removal by the DAEAPTS-SBA-15 is shown in Figure 4.11. The maximum sorption capacity of Cr(VI) occurred at a solution pH of 3. The sorption capacity was 81.22 mg/g at pH 3.0. The species of Cr(VI) existing in aqueous solution change according to their concentration and the solution pH. The percentage of the $HCrO_4^-$ species decreased and the percentage of the CrO_4^{2-} species increased when the solution pH was above 4 (Lee *et al*., 2016). The divalent form (CrO_4^{2-}) occupies two active sites, while the monovalent form ($HCrO_4^-$) occupies one. For this reason, Cr(VI) sorption capacity decreased with an increase in the solution pH above 4.

Cr(VI) removal by the DAEAPTS-SBA-15 as a function of adsorbent dose (initial concentration = 100 mg/L; adsorbent dose = 0.1 – 3.0 g/L; reaction time = 24 h) is provided in Figure 4.12. The percent removal was 31.6% at the dose of 0.1 g/L and 100% at a dose of 3.0 g/L. The sorption capacity decreased with increasing adsorbent dose from 0.1 to 3.0 g/L. The sorption capacity was 312.63 mg/g at 0.1 g/L, and decreased to 196.36 mg/g at 0.5 g/L. The sorption capacity decreased to 99.04 mg/g at 1.0 g/L, decreasing further to 33.01 mg/g at 3.0 g/L.

The Cr(VI) removal by DAEAPTS-SBA-15 as a function of reaction time is provided in Figure 4.13(a). At 30 °C, the Cr(VI) concentration decreased rapidly with increasing reaction time until equilibrium was reached. The Cr(VI) concentration dropped to 1.519 mg/L at 5 min of

reaction time and further decreased to 0.052 mg/L at 1 h. The chromate sorption reached equilibrium at 4 h of reaction time with Cr(VI) concentration of 0.017 mg/L. The sorption capacity changed from 97.60 to 99.10 mg/g with reaction time changing from 5 min to 4 h. The chromate removal by DAEAPTS-SBA-15 at different temperature is also presented in Figure 4.13(b), demonstrating that the Cr(VI) sorption to DAEAPTS-SBA-15 increased with increasing temperature from 15 to 45 °C.

The Cr(VI) removal by DAEAPTS-SBA-15 as a function of initial concentration is provided in Figure 4.14. The percent removal decreased with an increasing initial concentration from 10 to 1,000 mg/L. At the lowest concentration of 10 mg/L, the percent removal was 100%. The percent removal decreased to 97.0% at the chromate concentration of 200 mg/L and further decreased to 35.7% at the highest concentration of 1,000 mg/L. The sorption capacity increased from 9.25 to 328.34 mg/g with increasing chromate concentrations from 10 to 1,000 mg/L.
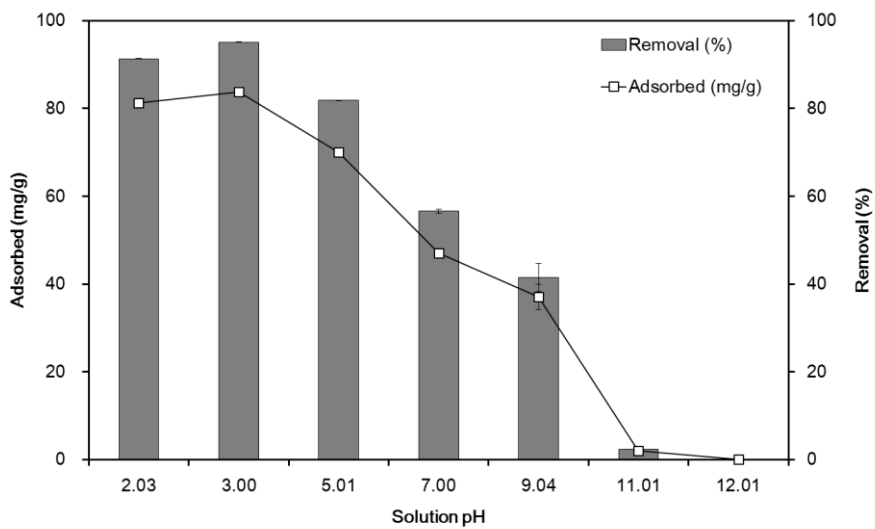
Figure 4.11 Effect of initial solution pH on Cr(VI) removal by
DAEAPTS-SBA-15.
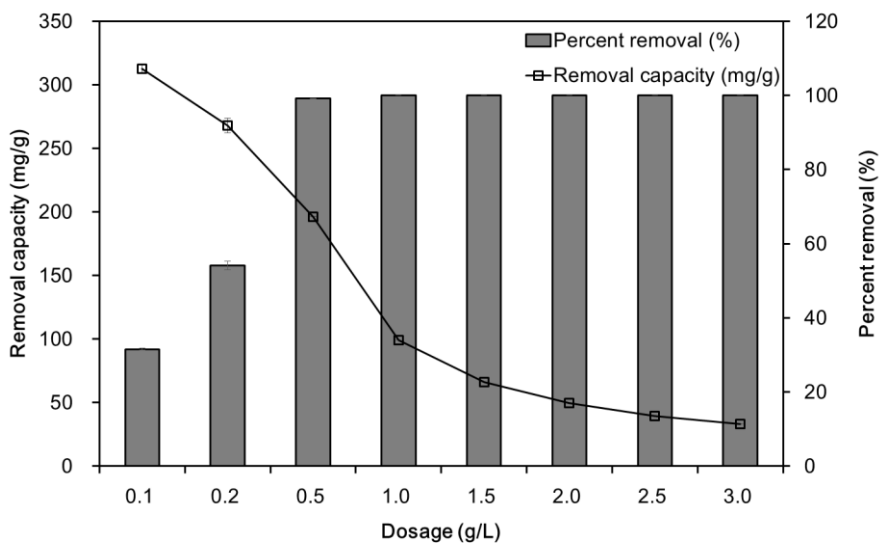
Figure 4.12 Effect of DAEAPTS-SBA-15 dose on removal of Cr(VI)
(initial concentration = 100 mg/L; reaction time = 24 h).
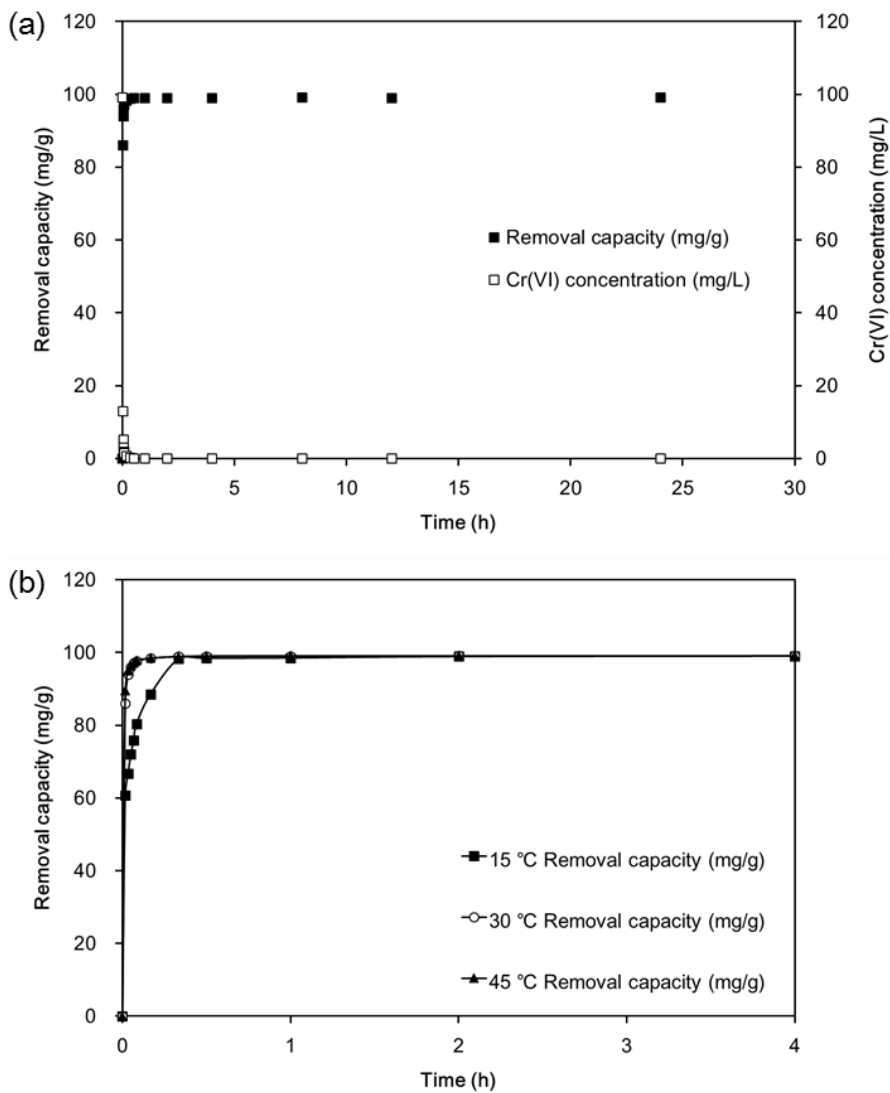
Figure 4.13 Effect of reaction time on Cr(VI) removal by DAEAPTS-SBA-15: (a) temperature = 30 °C; (b) temperature = 15, 30, 45 °C (adsorbent dose = 1 g/L; initial concentration = 100 mg/L).
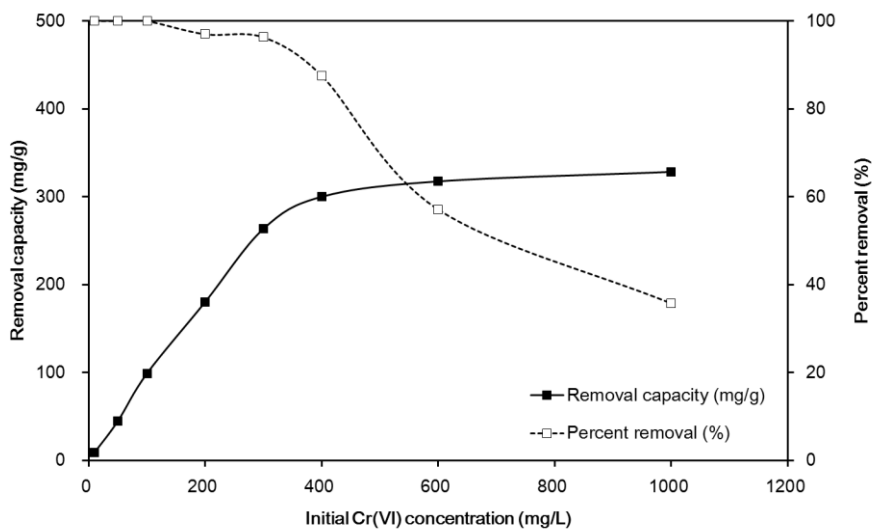
Figure 4.14 Cr(VI) removal by DAEAPTS-SBA-15 as a function of
initial concentration (reaction time = 4 h).

4.2.3. Kinetic, isotherm and thermodynamic model analyses

The kinetic model fits and the related model parameters are provided in Figure 4.15 and Table 4.6, respectively. The values of R^2 indicate that the pseudo second-order model (Figure 4.15(b)) was the best model to describe the kinetic data, and chemisorption is involved in the adsorption of Cr(VI) to DAEAPTS-SBA-15. The values of k_2 increased with increasing temperature, demonstrating that the time for equilibrium decreased as temperature increased.

The thermodynamic analysis for Cr(VI) sorption to DAEAPTS-SBA-15 is also presented in Figure 4.16, demonstrating that the Cr(VI) sorption to DAEAPTS-SBA-15 increased with increasing temperature from 15 to 45 °C. It indicates that the sorption process was endothermic. The thermodynamic parameters are presented in Table 4.7. The value of ΔH° was determined to be 39.64 kJ/mol, demonstrating that Cr(VI) sorption to DAEAPTS-SBA-15 had the endothermic nature. The value of ΔS° was calculated to be 198.92 J/K/mol, indicating that the randomness increased at the interface between solid and solution during the sorption process. The values of ΔG° were in the range from -17.68 to -23.65 kJ/mol, showing that Cr(VI) sorption to DAEAPTS-SBA-15 was spontaneous.

These results agree well with the reports of other researcher who examined the endothermic nature of Cr(VI) adsorption to amino functionalized mesoporous silica such as NH_2-SBA-15 (Wu *et al*., 2014).
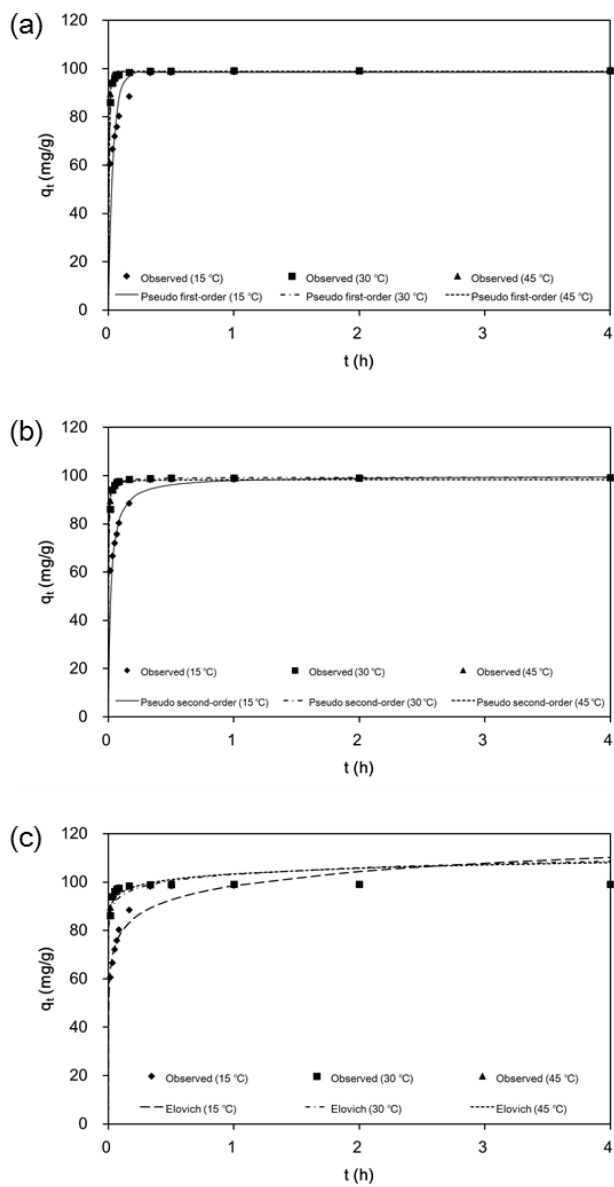
Figure 4.15 Kinetic model fits for Cr(VI) sorption to DAEAPTS-SBA-15: (a) pseudo first-order model; (b) pseudo second-order model; (c) Elovich model.

Table 4.6 Kinetic model parameters obtained from model fitting to experimental data.

Temp. (°C)	Pseudo first-order model				
	q_e (mg/g)	k_1 (1/h)	R^2	χ^2	SAE
15	98.445	26.316	0.858	22.093	57.637
30	98.688	123.405	0.898	0.199	10.097
45	98.893	141.699	0.835	0.200	9.448

Temp. (°C)	Pseudo second-order model				
	q_e (mg/g)	k_2 (g/mg/h)	R^2	χ^2	SAE
15	99.872	0.518	0.948	4.933	28.227
30	99.407	5.240	0.970	0.114	5.226
45	98.471	8.440	0.990	0.097	7.966

Temp. (°C)	Elovich model				
	α (mg/g/h)	β (g/mg)	R^2	χ^2	SAE
15	9.77.E+05	0.118	0.857	3.441	47.142
30	1.27.E+12	0.257	0.531	2.323	42.438
45	6.45.E+13	0.296	0.588	1.786	35.811
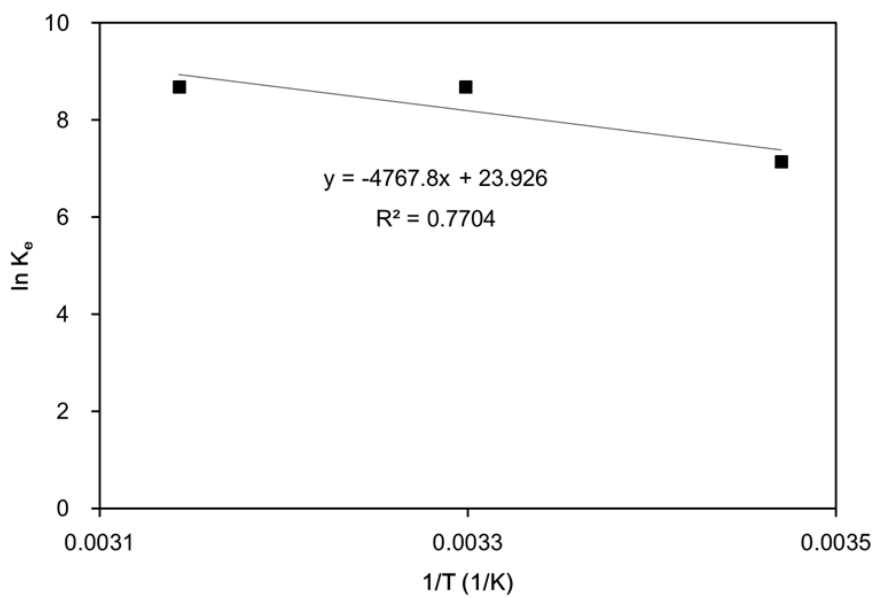
Figure 4.16 Thermodynamic analysis for Cr(VI) sorption to
DAEAPTS-SBA-15.

Table 4.7 Thermodynamic parameters for Cr(VI) sorption to DAEAPTS-SBA-15.

Temp. (°C)	$\Delta H°$ (kJ/mol)	$\Delta S°$ (J/K/mol)	$\Delta G°$ (kJ/mol)
15	39.64	198.92	-17.68
30			-20.67
45			-23.65

The equilibrium isotherm model fits and the related parameters are presented in Figure 4.17 and Table 4.8, respectively. The values of R^2, χ^2 and *SAE* indicate that Freundlich isotherm was best model to describe the equilibrium data. In Table 4.8, The maximum Cr(VI) sorption capacity (Q_m) was calculated to be 330.88 mg/g from the Langmuir model. It was higher than those of most other amino-functionalized mesoporous silicas (16.18 – 405 mg/g) reported in the literature (Yoshitake *et al*., 2002a, 2002b; Lam *et al*., 2007; Li *et al*., 2008; Benhamou *et al*., 2013; Idris *et al*., 2013; Wu *et al*., 2014; Wu *et al*., 2015; Dindar *et al*., 2015) (Table 4.9).

The results could be attributed to structural factor such as the link type of the silane chains and pore size of SBA-15, which is larger than those of MCM-41 and MCM-48. Amino chains in pores with larger dimension have much more freedom and accessibility to chromate ions (Zhang *et al*., 2007). The relatively rigid chain can inhibit the coordination of amino groups to an chromate ion (Yoshitake *et al*., 2005).

In addition, The density of the surface organic groups could influence the adsorption capacity (Li *et al*., 2008). Triamino groups capture oxyanions more effectively than expected from the number of N, suggesting stable complex formations (Yoshitake *et al*., 2002b). Protonation amine molecules is also considered to improve the adsorption capacity.
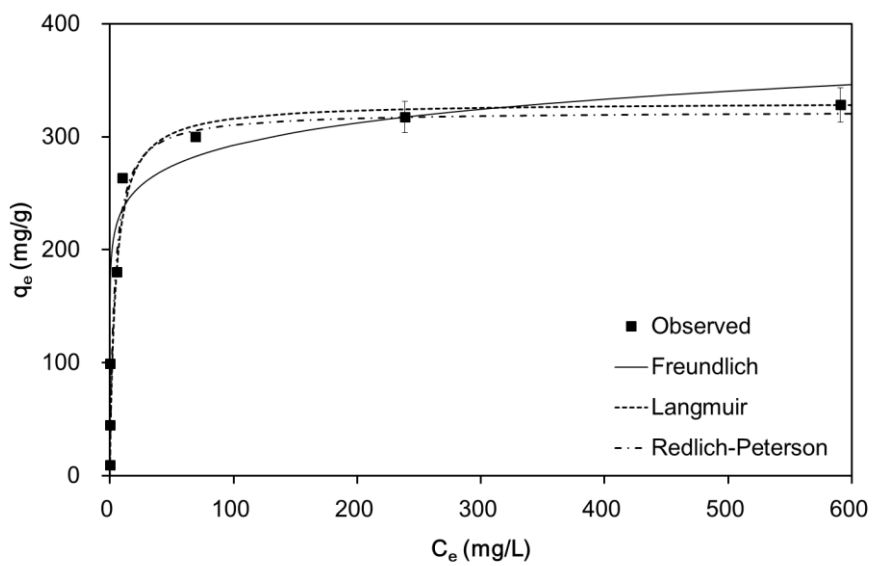
Figure 4.17 Equilibrium isotherm model fits for Cr(VI) sorption to DAEAPTS-SBA-15.

Table 4.8 Equilibrium isotherm model parameters obtained from model fitting to experimental data.

Freundlich model				
K_F (L/g)	1/n	R^2	χ^2	SAE
189.713	0.094	0.964	13.323	159.332

Langmuir model				
Q_m (mg/g)	K_L (L/mg)	R^2	χ^2	SAE
330.879	0.216	0.955	1.36.E+05	207.161

Redlich-Peterson model					
K_R (L/g)	a_R (L/mg)	g	R^2	χ^2	SAE
87.513	0.273	0.999	0.952	1.11.E+05	207.392

Table 4.9 Maximum sorption capacity of Cr(VI) in amino-functionalized mesoporous silicas reported in the literature (from the Langmuir isotherm analysis).

Mesoporous silica	Amino functionalization	Initial conc. (mg/L)	Sorption capacity (mg/g)	References
SBA-15	DAEAPTS	10 – 1000	330.9	This study
SBA-15	APTES	5 – 200	83.3	Dindar *et al*., 2015
SBA-15	APTES	5 – 300	171.9	Wu *et al*., 2015
SBA-15	EDA	5 – 50	16.2	Wu *et al*., 2014
SBA-15	APTMS	10 – 200	48.3	Idris *et al*., 2013
MCM-41	DDA	-	134.6	Benhamou *et al*., 2013
MCM-41	DMDDA	-	159.2	Benhamou *et al*., 2013
MCM-41	HDA		184.6	Benhamou *et al*., 2013
MCM-48	DDA	-	130.0	Benhamou *et al*., 2013
MCM-48	DMDDA	-	151.2	Benhamou *et al*., 2013
MCM-48	HDA	-	165.7	Benhamou *et al*., 2013
SBA-15	APTES	10 – 1000	405	Li *et al*., 2008
MCM-41	APTMS	98.3 – 786.2	196.5	Lam *et al*., 2007
MCM-41	APS	10.8 – 136.4	52.9	Yoshitake *et al*., 2002b
MCM-41	DAPT	10.8 – 123.3	92.1	Yoshitake *et al*., 2002b
MCM-41	TPDT	10.8 – 304.2	115.2	Yoshitake *et al*., 2002b
SBA-1	APS	10.8 – 151.3	94.2	Yoshitake *et al*., 2002a
SBA-1	DAPT	10.8 – 163.8	178.4	Yoshitake *et al*., 2002a
SBA-1	TPDT	10.8 – 317.2	210.8	Yoshitake *et al*., 2002a

4.2.4. Fixed-bed adsorption of chromate

Breakthrough curves (BTCs) obtained from the fixed-bed experiments are shown in Figure 4.18. The results of the column experiments are provided in Table 4.10. The chromate removal in the wastewater 2 (experiment 2) was higher than that in the wastewater 1 (experiment 1). The chromate sorption capacity in the wastewater 1 was 88.7 mg/g, whereas the chromate sorption capacity in the wastewater 2 was 158.8 mg/g. Wastewater 1 had much higher initial concentration (2692.8 mg/L) than wastewater 2 (412.4 mg/L). Higher concentration of chromate in water reduced sorption efficiency of DAEAPTS-SBA-15 PVA/alginate composites. In experiment 2, relative chromate concentration (C/C_0) of effluent remained under 0.2 until 17 days later. In contrast, relatively faster saturation were observed in the BTCs of wastewater 2 (experiment 1, 3).

The regenerated DAEAPTS-SBA-15 PVA/alginate composites were examined for chromate sorption to compare their performances with those of the pristine ones. The chromate sorption capacity of pristine DAEAPTS-SBA-15 PVA/alginate composites was 88.7 mg/g (experiment 1) and regenerated composites had 75.8 mg/g (experiment 3) of sorption capacity. There were loss of 15% in the chromate sorption capacity of DAEAPTS-SBA-15 PVA/alginate composites after regeneration.
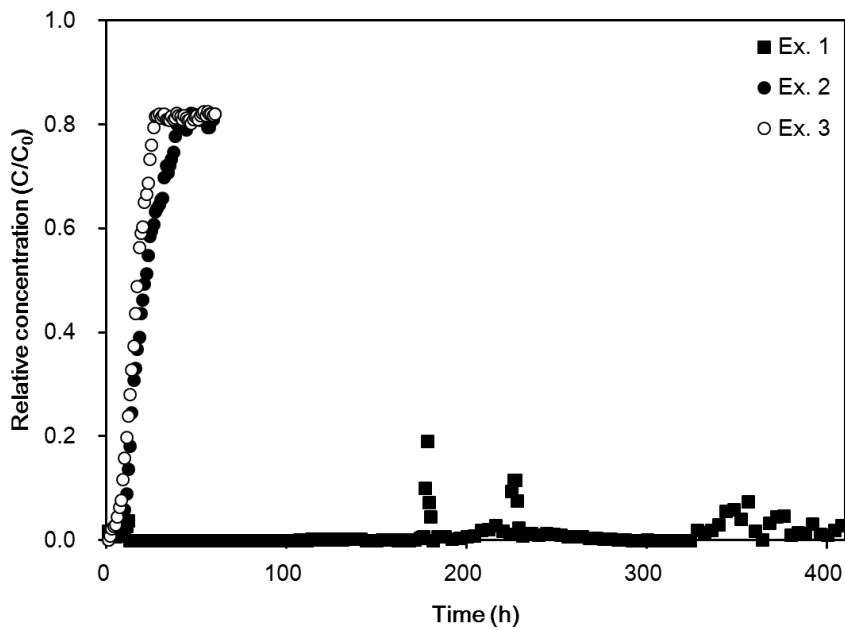
Figure 4.18 Breakthrough curves of Cr(VI) obtained from the fixed-bed experiments.

117

Table 4.10 Results from column experiments for the Cr(VI) sorption to DAEAPTS-SBA-15 PVA/alginate composites.

Ex.	m_{total} (mg)	q_{total} (mg)	Re (%)	q_{eq} (mg/g)
1	4808.9	2222.8	46.2	88.7
2	4023.8	3980.3	98.9	158.8
3	4808.9	1901.5	39.5	75.8

4.2.5. Conclusions

The removal of chromate by triamine-functionalized mesoporous silica (DAEAPTS-SBA-15) and the polymer composites containing the functionalized mesoporous silica (DAEAPTS-SBA-15 PVA/alginate composites) were investigated in this chapter. Kinetic experiment indicated that chromate sorption by DAEAPTS-SBA-15 reached equilibrium at 4 h. The results demonstrated that DAEAPTS-SBA-15 could remove chromate rapidly and effectively with the maximum capacity of 330.88 mg/g. . It was higher than those of most other amino-functionalized mesoporous silicas (16.18 – 405 mg/g) reported in the literature. The chromate sorption capacity decreased with an increase in the solution pH above 4.

The column experiments showed that the adsorption capacities of DAEAPTS-SBA-15 PVA/alginate composites were in the range of 75.8 – 158.8 mg/g in the given experimental conditions. The regenerated DAEAPTS-SBA-15 PVA/alginate composites showed slight decrease in chromate uptake.

These results demonstrated that DAEAPTS-SBA-15 PVA/alginate composites could be applied as efficient adsorbents for chromate sorption from wastewater.

Chapter 5 Characterization of calcined Mg-Fe layered double hydroxide for phosphate removal from aqueous solutions

Layered double hydroxides(LDHs) have high surface area and large anion exchange capacity. It is known that the calcined LDHs can remove phosphate ions through the so-called structural memory effect and ion exchange with HCO_3^- or other anions on the surface (He *et al.*, 2010). The aim of this chapter was examine the removal of phosphate from aqueous solutions by calcined Mg-Fe LDH. The effects of adsorbent dose, reaction time, initial concentration, solution pH, temperature, regeneration, and stream water were investigated. Kinetic, equilibrium isotherm, and thermodynamic models were used to analyze the data obtained from batch experiments.

5.1. Materials and Methods

5.1.1. Synthesis of calcined Mg-Fe layered double hydroxide

All chemicals used for the experiments were purchased from Sigma Aldrich. Mg-Fe layered double hydroxide was prepared by a co-precipitation method using the respective nitrate salts (Park *et al.*, 2011). A 700 mL solution (Mg(II)/Fe(III) molar ratio = 2) of $Mg(NO_3)_2 \cdot 6H_2O$ and $Fe(NO_3)_3 \cdot 6H_2O$ was added dropwise into a 1,000 mL alkali solution (pH = 13) of sodium hydroxide (NaOH, 3.5 mol) and sodium carbonate (Na_2CO_3, 0.94 mol) using a peristaltic pump (QG400, Fasco, Springfield, MO, USA). The dropwise addition was conducted under intensive stirring at room temperature. The resulting precipitates were oven-dried at 65°C for 18 h. Precipitates were washed thoroughly with deionized

water to remove excess sodium, and then final suspensions were centrifuged for 20 min at 11,200×g. The washed precipitates were calcined at 300 ℃ for 24 h in an electric muffle furnace (C-FMA, Vision Lab, Seoul, Korea) and were then pulverized in a ball mill to obtain a powder form of calcined Mg-Fe LDH (Mg-Fe CLDH). It should be noted that the Mg-Fe LDH calcined at 300 ℃ had the largest specific surface area and highest bacteriophage sorption capacity among the four LDHs prepared at different temperatures (105, 300, 500, 700 ℃) (Park *et al.*, 2011).

5.1.2. Characterization of Mg-Fe CLDH

Transmission electron microscopy (TEM, JEM-1010, JEOL, Tokyo, Japan) and field emission scanning electron microscopy (FESEM, Supra 55VP Carl Zeiss, Oberkochen, Germany) were used to visualize the calcined LDH. FESEM was also used to conduct an energy dispersive X-ray spectrometry (EDS) analysis. A Zetasizer (ELSZ-1000, Photal Otsuka Electronics, Osaka, Japan) was used to determine the particle size distribution. A surface area analyzer (BELSORP-max, BEL Japan Inc., Osaka, Japan) was used to perform nitrogen gas (N_2) adsorption–desorption experiments after the samples were pretreated at 120 ℃. A powder X-ray diffractometer (XRD, D8 Advance, Bruker, Germany) was used (Cu Kα radiation = 1.5406 Å, scanning speed = 0.6°/sec) to characterize the calcined LDH before and after the phosphate adsorption experiments. A Fourier-transform infrared (FTIR) spectrometer (Nicolet

6700, Thermo Scientific, Waltham, MA, USA) was used to obtain the infrared spectra of the calcined LDH before and after the phosphate adsorption experiments.

5.1.3. Phosphate sorption experiments

The desired phosphate (P) solution was prepared by diluting the stock solution (1,000 mgP/L) made from potassium dihydrogen orthophosphate (KH_2PO_4). Phosphate removal by the calcined LDH was conducted in triplicate under batch conditions (temperature = 30 °C, reaction time = 24 h) without pH adjustment unless stated otherwise. The batch experiments were performed with 50 mL polypropylene conical tubes (solution volume = 30 mL).

The first set of experiments examined the phosphate removal as a function of adsorbent dosage (adsorbent dose = 0.1 − 1.0 g/L; initial P concentration = 1, 2, 4 mgP/L). The tubes were shaken at 100 rpm using a shaking incubator (Daihan Science, Seoul, Korea). The samples were collected after reaction and were filtered through a 0.45 μm membrane filter. The phosphate concentration was analyzed by the ascorbic acid method (APHA, 1995). The phosphate concentration was measured at a wavelength of 880 nm using a UV−visible spectrophotometer (Helios, Thermo Scientific, Waltham, MA, USA).

The second set of experiments was conducted to observe the phosphate removal as a function of initial solution pH (adsorbent dose = 0.2 g/L; initial P concentration = 2 mgP/L). Basic (0.1 M NaOH) and

acidic (0.1 M HCl) solutions were used to adjust the pH of the reaction solution from 3.0 to 11.0, and the pH was measured using a pH probe (9107BN, Thermo Scientific, Waltham, MA, USA).

The third set of experiments examined the regeneration and reuse of the calcined LDH through adsorption-desorption experiments (adsorbent dose = 0.2 g/L; initial P concentration = 2 mgP/L). For each round of the experiments, desorption of the phosphate from the calcined LDH was performed by dispersing the calcined LDH in 0.1 M NaOH solution for 24 h.

The fourth set of experiments was performed as a function of reaction time (adsorbent dose = 0.2 g/L; initial P concentration = 2 mgP/L). The samples were collected after various reaction times from 5 min to 24 h. Additional experiments were performed at 15 and 45 °C to examine the effect of temperature on phosphate removal.

The fifth set of experiments was conducted as a function of the initial P concentration (adsorbent dose = 0.1 − 0.3 g/L; initial P concentration = 1 − 20 mgP/L).

The sixth set of experiments was conducted using real stream water collected from the Seoho stream located in Suwon, Republic of Korea (adsorbent dose = 0.1 − 0.8 g/L; initial P concentration = 2 mgP/L). The chemical oxygen demand (COD_{cr}) of the stream water was measured according to a standard method (APHA, 1995), whereas the ionic composition was analyzed using an ion chromatograph (Dionex ICS-3000, Thermo Scientific, Waltham, MA, USA). The stream water had the following composition: $CODcr$ = 4.2 mg/L, pH = 6.9, ionic strength = 613 μS/cm, NaCl = 2.41 mM, $NaHCO_3$ = 0.38 mM, $Ca(HCO_3)_2$ = 0.67

mM, $CaSO_4 = 0.17$ mM, $MgSO_4 = 0.20$ mM, $Mg(NO_3)_2 = 0.03$ mM, $KNO_3 = 0.32$ mM, and $K_2HPO_4 = 1.77 \times 10^{-4}$ mM (Table 5.2). Because the stream water sample had a very low phosphate concentration (0.017 mgP/L), phosphate was added to an initial P concentration of 2 mgP/L.

Table 5.1 Batch experimental conditions for the phosphate sorption to Mg-Fe CLDH.

	Dose (g/L)	Reaction Time (h)	Initial conc. (mgP/L)	Solution pH	Temp. (°C)	Solution volume (mL)
Effect of adsorbent dose	0.1 – 1.0	24	1 – 4		30	30
Effect of initial solution pH	0.2	24	2	3.0 – 11.0	30	30
Effect of regeneration and reuse	0.2	24	2		30	30
Effect of reaction time	0.2	0.08 – 24	2		15 – 45	30
Effect of initial P concentration	0.1 – 0.3	24	1 – 20		30	30
Effect of stream water	0.1 – 0.8	24	2		30	30

Table 5.2 Characteristics of stream water samples.

Component	Value
NaCl (mM)	2.41
NaHCO$_3$ (mM)	0.38
Ca(HCO$_3$)$_2$ (mM)	0.67
CaSO$_4$ (mM)	0.17
MgSO$_4$ (mM)	0.20
Mg(NO$_3$)$_2$ (mM)	0.03
KNO$_3$ (mM)	0.32
K$_2$HPO$_4$ (mM)	1.77×10^{-4}
COD$_{cr}$ (mg/L)	4.2
pH	6.9
IS (μS/cm)	613

5.2. Results and Discussion

5.2.1. Characterization of Mg-Fe CLDH

The calcined Mg-Fe LDH was visualized by TEM, FESEM, and digital images (Figures 5.1(a) and 5.1(b)), demonstrating that it had a light brownish color with a particle size of several hundred nanometers. The particle size distribution (Figure 5.2(a)) showed that the average particle size of the calcined LDH was 413.6 nm.

The N_2 adsorption–desorption experiments (Figure 5.2(b)) indicated that the calcined LDH had a BET specific surface area of 117.96 m^2/g, a total pore volume of 0.67 cm^3/g, and an average pore diameter of 22.63 nm. The EDS pattern (Figure 5.2(c)) demonstrated that Mg was evident at a peak position of 1.254 keV as a K alpha X-ray signal, whereas Fe was found at peak positions of 0.707, 6.403 and 7.057 keV as L alpha, K alpha and K beta signals, respectively.

The XRD patterns of the calcined Mg-Fe LDH before and after phosphate adsorption (Figure 5.3(a)) showed that the Mg-Fe LDH had reflection characteristics of the layered structure with sharp and intense lines at low 2θ and less intense lines at high 2θ. The Mg-Fe LDH had a rhombohedral crystal system (cell parameter: a = 3.109, c =23.412) with peaks corresponding to LDH (JCPDS 24-1110, 2θ = 11.341, 22.783, 34.141, 38.541, 45.740, 59.387, 60.676, 64.476), which agreed well with the literature (Kovanda *et al*., 2003; Ferreira *et al*., 2004).

In the calcined Mg-Fe LDH, the hydrotalcite structure (LDH phase) changed to a rather amorphous phase due to thermal treatment at 300 °C (Kovanda *et al*., 2003; Ferreira *et al*., 2004; Kanezaki, 1998) with XRD

peaks of $2\theta = 13.827, 34.085, 35.801$, and 59.820 (before P adsorption). After P adsorption, the calcined LDH had peaks at $2\theta = 11.518, 22.999, 34.481$, and 59.688, which were slightly different from those observed before P adsorption, indicating that structural change occurred during the reaction due to contact with water. The XRD pattern after P adsorption was not fully reconstructed to the LDH phase but became similar to the XRD pattern of the Mg-Fe LDH.

The FTIR spectra of the calcined LDH before and after phosphate adsorption are presented in Figure 5.3b. In the FTIR data before P adsorption, the band at approximately 3628 cm^{-1} corresponded to the stretching vibration of the OH groups (Fernández $et\ al.$, 1998). The peak at approximately 1396 cm^{-1} corresponded to the stretching vibration of CO_3^{2-} (Ferreira et al., 2004). The peak at approximately 1058 cm^{-1} corresponded to C-O-C (Madhu $et\ al.$, 2013). The FTIR data after P adsorption showed the OH stretching band (3445 cm^{-1}) that was found before P adsorption. The peak at approximately 1362 cm^{-1} corresponded to the C-O stretching vibration (Sasai $et\ al.$, 2012). After P adsorption, a band corresponding to a Fe-O-P vibration (1048 cm^{-1}) was found in the FTIR data (Mal $et\ al.$, 2006).
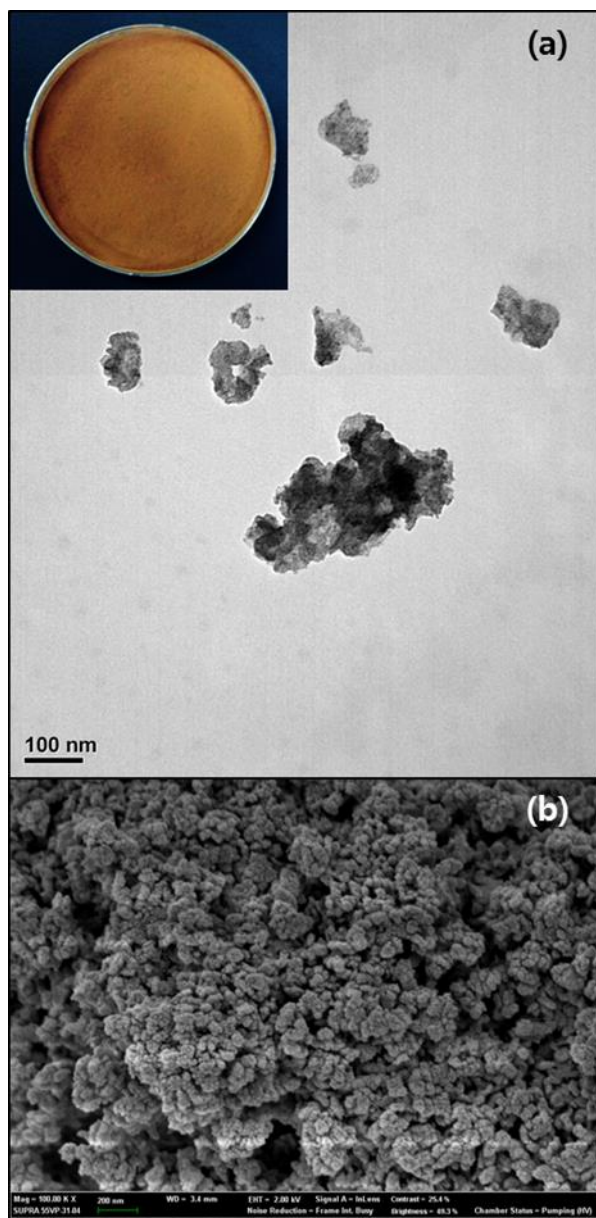
Figure 5.1 (a) TEM image (inset = digital image) and (b) FESEM
image of calcined Mg-Fe LDH.
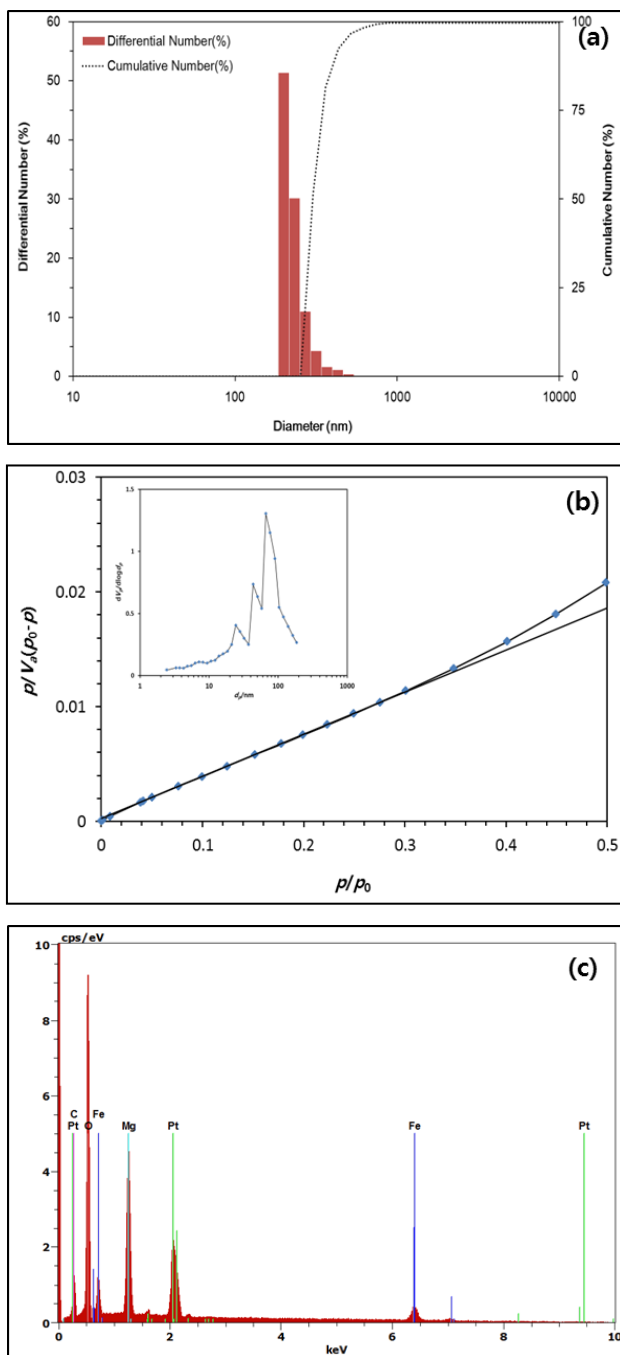
Figure 5.2 (a) Particle size distribution, (b) N$_2$ adsorption-desorption analysis, and (c) EDS pattern of calcined Mg-Fe LDH.
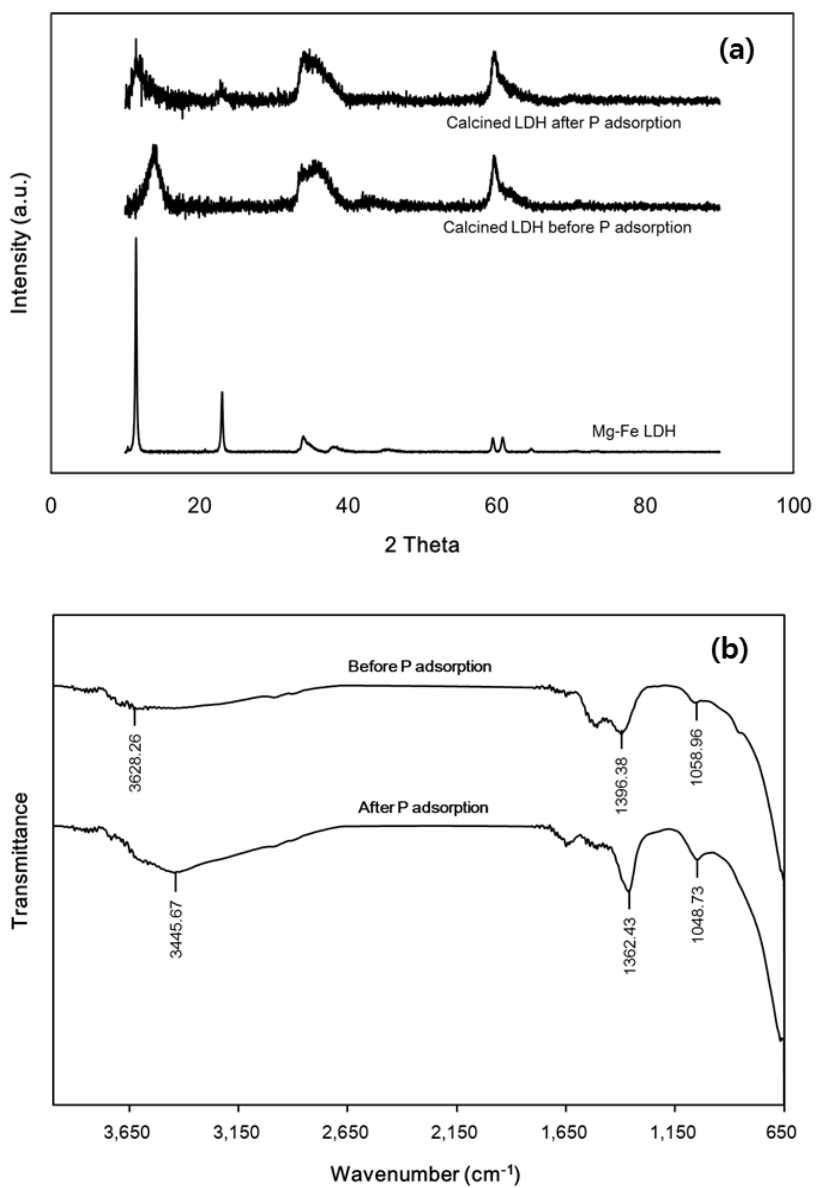
Figure 5.3 (a) XRD patterns and (b) FTIR spectra of calcined Mg-Fe
LDH before and after phosphate sorption experiments.

5.2.2. Characterization of phosphate removal

The characteristics of phosphate adsorption to the calcined LDH are presented in Figure 5.4 – 5.6. The phosphate removal as a function of adsorbent dose is shown in Figure 5.4. The percent removal increased as the adsorbent dose increased from 0.05 to 1.0 g/L. The percent removal reached 100% at an adsorbent dose of 0.2 or 0.3 g/L, depending on the initial P concentration (1, 2, 4 mgP/L). Meanwhile, the sorption capacity decreased with increasing adsorbent dose from 0.05 to 1.0 g/L at initial P concentrations of 1 and 2 mgP/L. At 4 mgP/L, the sorption capacity increased slightly with increasing adsorbent dose from 0.05 to 0.1 g/L and then decreased gradually thereafter.

The effect of initial solution pH on phosphate removal by the calcined LDH is shown in Figure 5.5. The sorption capacity did not vary much (8.99 – 9.41 mgP/L) at initial pH values of 3.0 – 9.1. In other words, phosphate removal by the calcined Mg-Fe LDHs was relatively constant at acidic, neutral, and weakly basic solution conditions. This was attributed to the final pH converging to 7.4 – 8.0 during the experiments at initial pH values of 3.0 – 9.1. This could be ascribed to the competition between phosphate and hydroxyl ions for the sorption sites.

A previous study reported that three mechanisms can contribute to the removal of phosphate by LDHs and calcined LDHs. In surface adsorption, the negatively-charged phosphate can adsorb to the positively charged brucite-like layer through electrostatic interactions. In interlayer anion exchange, the charge-balancing anions in the interlayer region can be replaced by phosphate. In the reconstruction/rehydration of calcined LDHs, phosphate could intercalate into the interlayer of

LDHs due to the reformation effect (Goh *et al*., 2008).

The removal of phosphate after regeneration and reuse of the calcined LDH is presented in Figure 5.6. In the first adsorption-desorption cycle, the sorption capacity was determined to be 9.28 mgP/g, whereas the recovery rate from desorption was 98.2%. In the second cycle, the sorption capacity was slightly reduced to 8.21 mgP/g, whereas the recovery rate was 95.5%. In the third cycle, the sorption capacity decreased to 7.86 mgP/g with a recovery rate of 91.7%. Our results demonstrate that the calcined Mg-Fe LDH could be used repeatedly as adsorbents for phosphate removal through adsorption-desorption procedures.
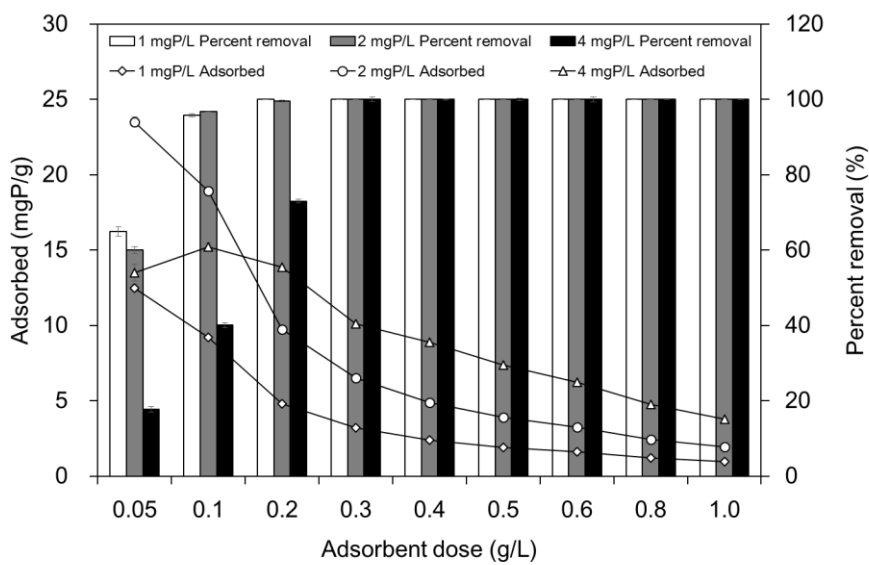
Figure 5.4 Effect of adsorbent dose on phosphate adsorption to calcined Mg-Fe LDH
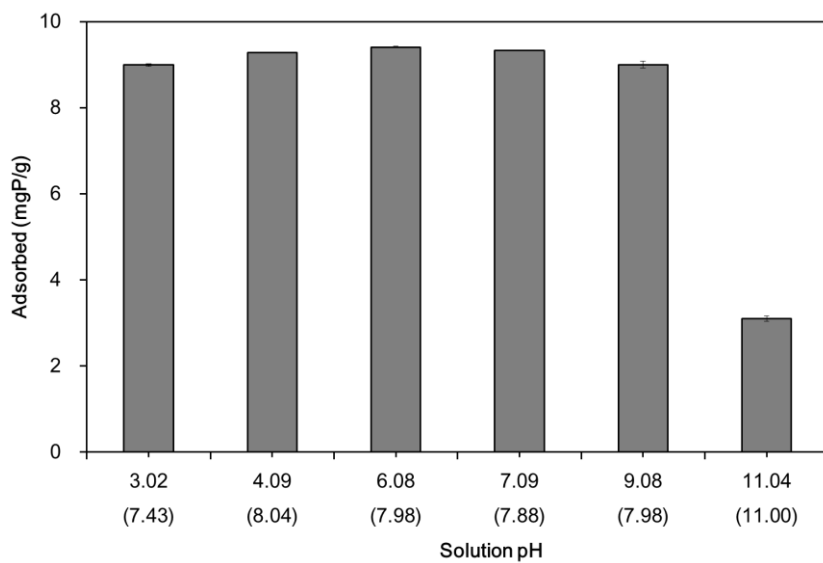
Figure 5.5 Effect of adsorbent initial solution pH on phosphate adsorption to calcined Mg-Fe LDH (the number in parentheses is the final pHs).
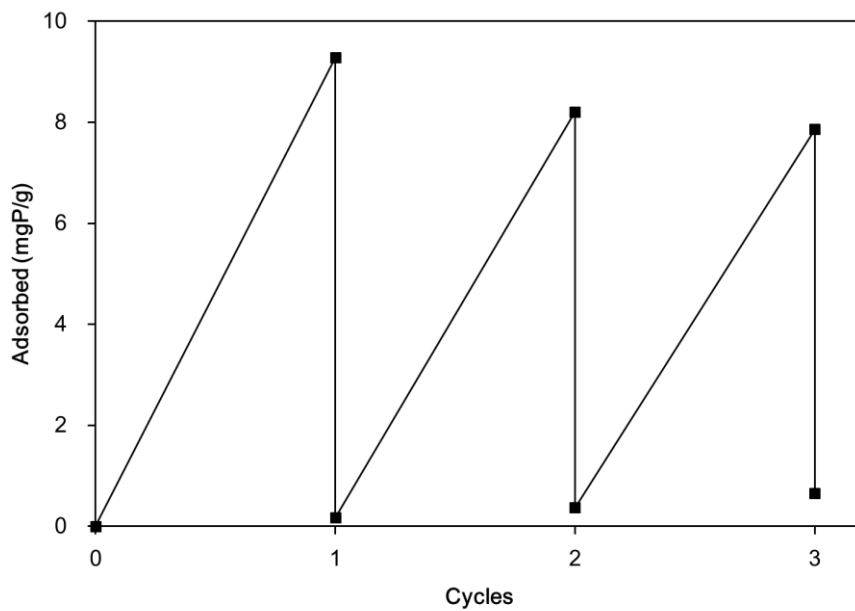
Figure 5.6 Effect of regeneration and reuse on phosphate adsorption to calcined Mg-Fe LDH.

The characteristics of phosphate adsorption on the calcined Mg-Fe LDH are also shown in Figure 5.7 – 5.9. The phosphate removal as a function of reaction time is shown in Figure 5.7. The sorption capacity increased gradually with increasing reaction time until equilibrium was reached. At 15 °C, the sorption capacity increased from 4.63 to 8.72 mgP/g with increasing reaction time from 1 to 24 h. At the same reaction time range, the sorption capacity at 30 °C increased from 6.71 to 9.28 mgP/g, whereas the sorption capacity at 45 °C increased from 7.64 to 9.31 mgP/g. In addition, the sorption capacity increased with an increase in temperature from 15 to 45 °C.

The phosphate removal as a function of initial phosphate concentration is provided in Figure 5.8. At an adsorbent dose of 0.1 g/L, the sorption capacity increased from 8.86 to 30.01 mgP/g with increasing initial phosphate concentration from 1 to 20 mgP/L. At the same initial phosphate concentration range, the sorption capacity at 0.2 g/L increased from 3.15 to 21.53 mgP/g, whereas the sorption capacity at 0.3 g/L increased from 3.14 to 17.37 mgP/g. Also, the sorption capacity decreased as the adsorbent dose increased from 0.1 to 0.3 g/L.

The phosphate removal by the calcined LDH from stream water is shown in Figure 5.9. The percent removal increased from 83.7 to 99.5% as the adsorbent dose increased from 0.1 to 0.8 g/L, whereas the sorption capacity decreased from 15.76 to 2.34 mgP/g at the same adsorbent dose range. Phosphate removal in the stream water was lower than that in the synthetic phosphate solution (Figure 5.4). For instance, the sorption capacity in the synthetic solution was 18.95 mgP/g for an adsorbent dose of 0.1 g/L, whereas the sorption capacity in the stream water was 15.76

mgP/g at the same adsorbent dose. This could be attributed to the presence of oxyanions, including nitrate, sulfate, and (bi)carbonate, in the stream water. Previous investigators reported that (bi)carbonate could play a major role as interference in phosphate removal by adsorbents in aqueous solutions (Lee *et al*., 2012).
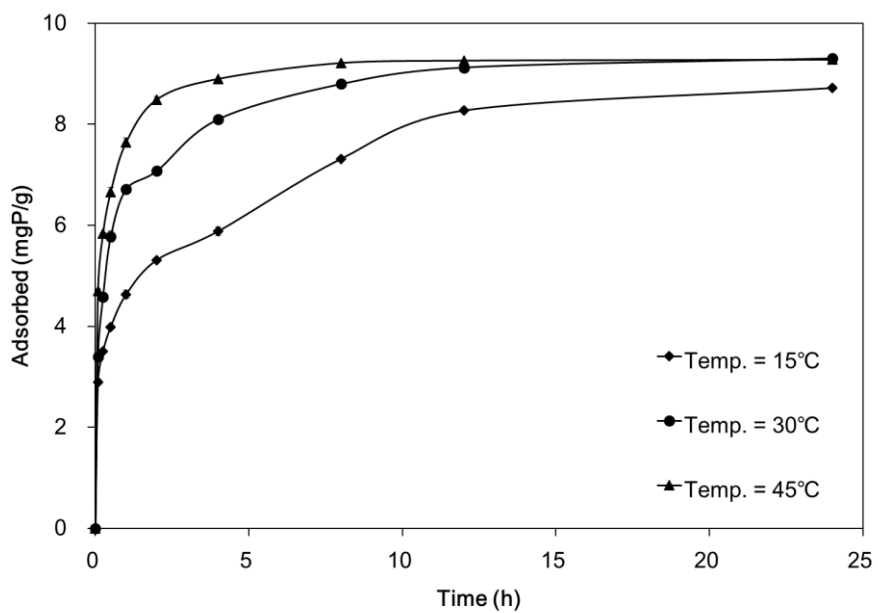
Figure 5.7 Effect of reaction time on phosphate adsorption to calcined
Mg-Fe LDH.
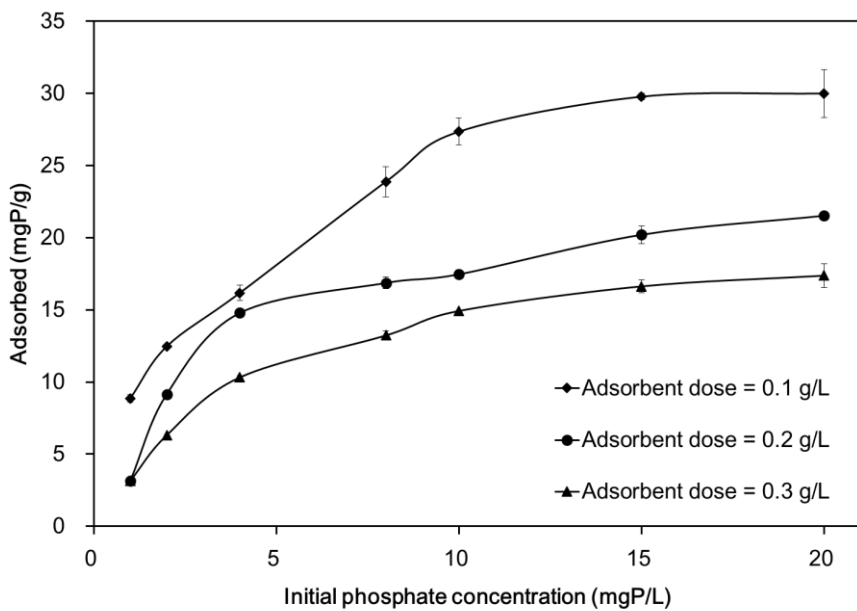
Figure 5.8 Effect of initial concentration on phosphate adsorption to calcined Mg-Fe LDH.
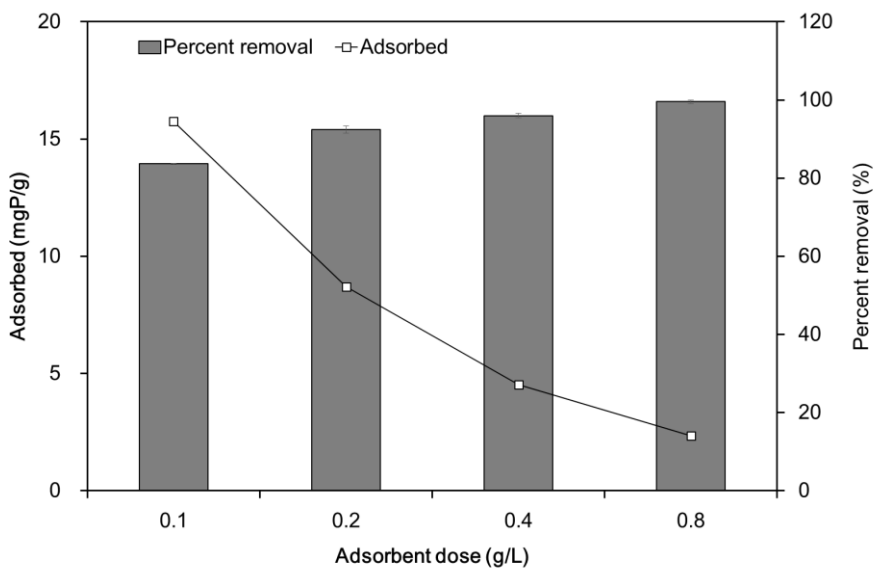
Figure 5.9 Effect of stream water on phosphate adsorption to calcined Mg-Fe LDH.

5.2.3. Kinetic, isotherm and thermodynamic analyses

The kinetic model analysis is presented in Figure 5.10. The kinetic model parameters are provided in Table 5.3. In the pseudo first-order and pseudo second-order model parameters (Table 5.3), the values of q_e increased with increasing temperature, demonstrating that the phosphate sorption capacity increased with increasing temperature. The values of k_1 and k_2 increased with increasing temperature, indicating that the time required to reach equilibrium decreased with increasing temperature. The rate constant k_2 was used to calculate the initial adsorption rate constant (h) at $t \rightarrow 0$ with the following equation (Gupta *et al.*, 2011):

$$ h = k_2 q_e^2 \tag{1} $$

The value of h increased with increasing temperature, indicating that adsorption at an initial phase of the sorption process became faster with increasing temperature. The values of R^2, χ^2, and *SAE* indicate that the Elovich model (Figure 5.10(c)) was most suitable at describing the kinetic data. The Elovich model assumes that adsorbents have energetically heterogeneous surfaces (Gupta *et al.*, 2011). The value of α from the Elovich model increased with increasing temperature. Also, the value of α was $1 - 2$ orders of magnitude higher than the value of h from the pseudo second-order model.
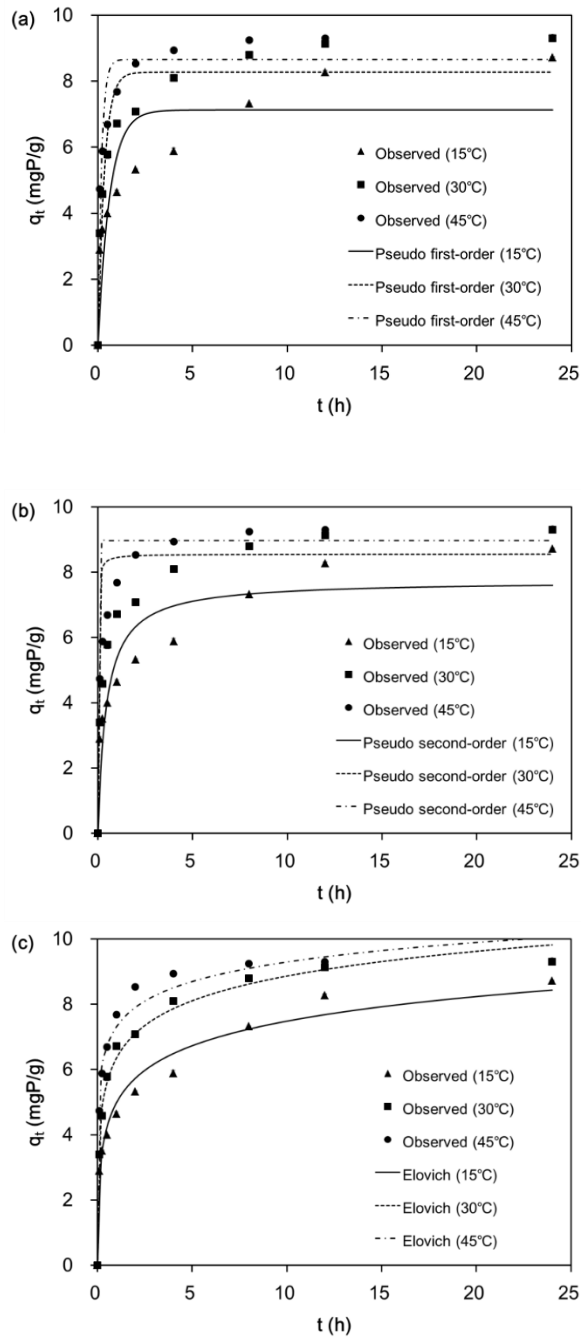
Figure 5.10 Kinetic model analysis: (a) pseudo first-order model; (b) pseudo second-order model; (c) Elovich model.

144

Table 5.3 Kinetic model parameters obtained from model fitting to experimental data.

Temp. (°C)	Pseudo first-order model				
	q_e (mgP/g)	k_1 (1/h)	R^2	χ^2	SAE
15	7.314	1.577	0.708	6.272	9.761
30	8.101	3.341	0.801	1.783	7.272
45	8.934	4.284	0.816	1.955	5.838

Temp. (°C)	Pseudo second-order model					
	q_e (mgP/g)	k_2 (g/mgP/h)	h (mgP/g/h)	R^2	χ^2	SAE
15	7.745	0.274	16.451	0.823	3.464	7.132
30	9.110	0.387	32.080	0.948	1.035	3.904
45	9.371	0.717	62.920	0.944	0.632	2.762

Temp. (°C)	Elovich model				
	α (mgP/g/h)	β (g/mgP)	R^2	χ^2	SAE
15	6.68E+01	0.834	0.956	0.757	3.092
30	2.60E+02	0.863	0.982	0.099	1.837
45	4.08E+03	1.161	0.933	0.193	3.128

The equilibrium isotherm model analysis is presented in Figure 5.11. The isotherm model parameters are provided in Table 5.4. The values of R^2, χ^2, and *SAE* indicate that the Freundlich isotherm was most suitable for describing the equilibrium data. The Freundlich isotherm can be applied to multilayer adsorption on the heterogeneous surfaces of adsorbents (Foo and Hameed, 2010). Freundlich model parameters are shown in Table 5.4, and the values of K_F were in the range of 11.52 – 16.36 L/g. The maximum sorption capacity (Q_m) from the Langmuir isotherm was determined to be 33.06 mgP/g, which is in the range of the phosphate sorption capacity (7.3 – 350 mgP/g) of LDHs or calcined LDHs reported in the literature (Table 5.5).

The thermodynamic analysis is presented in Figure 5.12. The thermodynamic parameters are provided in Table 5.6. The positive value of ΔH° (528.84 kJ/mol) indicates the endothermic nature of phosphate adsorption to the calcined Mg-Fe LDH. The positive value of ΔS° (1836.48 J/K/mol) indicates that the randomness increased at the interface between the calcined LDH and solution during the sorption process. The negative values of ΔG° (-0.36 to -55.45 kJ/mol) indicate that the phosphate adsorption process was spontaneous. Our results agree well with the reports of other researchers who examined the endothermic nature of phosphate adsorption to LDHs such as Zn-Al LDH (Cheng *et al*., 2009), and Ca-Al LDH (Son *et al*., 2016).
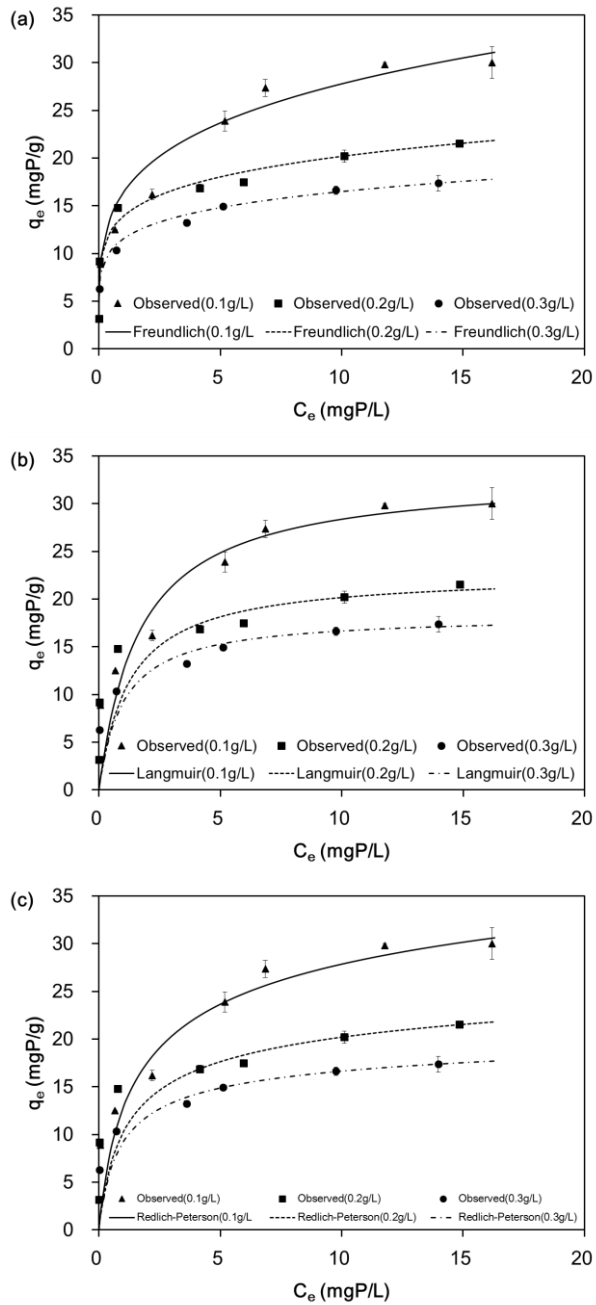
Figure 5.11 Equilibrium model analysis: (a) Freundlich model, (b)
Langmuir model, (c) Redlich-Peterson model.

Table 5.4 Equilibrium model parameters obtained from fitting the model to experimental data.

Dose (g/L)	Freundlich model				
	K_F (L/g)	$1/n$	R^2	χ^2	SAE
0.1	16.36	0.230	0.956	1.215	10.102
0.2	13.86	0.163	0.967	1.043	6.224
0.3	11.52	0.156	0.990	0.087	1.730

Dose (g/L)	Langmuir model				
	Q_m (mgP/g)	K_L (L/mgP)	R^2	χ^2	SAE
0.1	33.06	0.604	0.936	55.789	16.090
0.2	22.71	0.796	0.888	656.572	20.382
0.3	18.33	1.003	0.959	94.548	10.405

Dose (g/L)	Redlich-Peterson model					
	K_R (L/g)	a_R (L/mgP)	g	R^2	χ^2	SAE
0.1	28.51	1.224	0.878	0.945	37.601	14.931
0.2	24.01	1.351	0.906	0.903	494.041	18.399
0.3	23.31	1.537	0.928	0.966	73.810	9.040

Table 5.5 Phosphate sorption capacity of LDHs reported in the literature.

Type of LDH	Maximum sorption capacity (mgP/g)	Reference
Calcined Zn-Al LDH	50	Cheng *et al.*, 2009
Mg-Fe/Zr LDH	10	Chitrakar *et al.*, 2010
Calcined Mg-Al/Fe LDH	350	Triantafyllidis *et al.*, 2010
Zn-Al LDH	68.4	Yang *et al.*, 2014
Calcined Mg-Mn LDH	7.3	Chitrakar *et al.*, 2005
Calcined Mg-Al LDH	44.3	Das *et al.*, 2006
Mg-Al LDH	47.3	Kuzawa *et al.*, 2006
Zn-Al/Zr LDH	91	Koilraj *et al.*, 2010
Calcined Zn-Al LDH	232	Zhou *et al.*, 2011
Calcined Mg-Fe LDH	33.1	This study
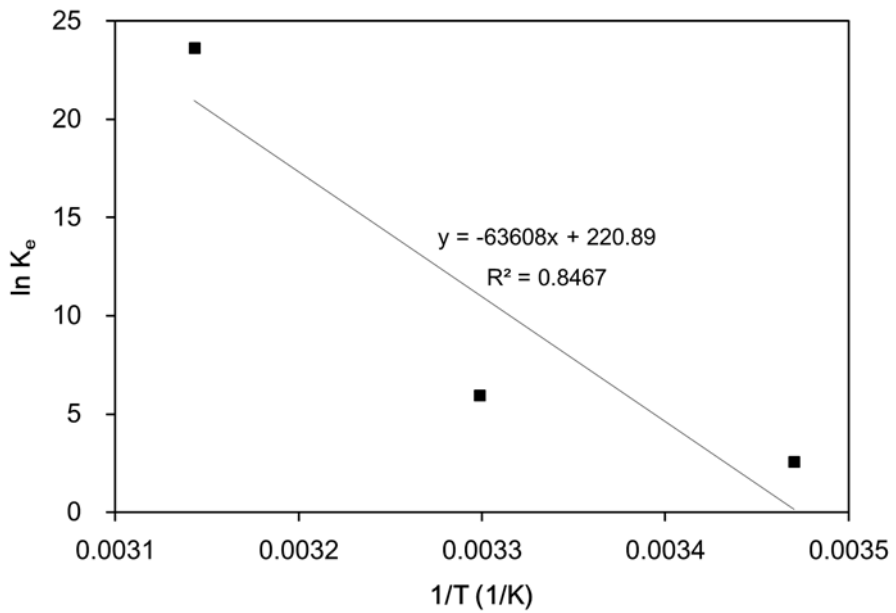
Figure 5.12 Thermodynamic analysis for phosphate adsorption to calcined Mg-Fe LDH.

Table 5.6 Thermodynamic parameters obtained from fitting the model to experimental data.

Temp. (˚C)	ΔH° (kJ/mol)	ΔS° (J/K/mol)	ΔG° (kJ/mol)
15	528.84	1836.48	-0.36
30			-27.91
45			-55.45

5.2.4. Conclusions

Phosphate removal by calcined Mg-Fe LDHs was examined in this chapter using batch experiments. The results demonstrated that calcined Mg-Fe LDHs effectively removed phosphate with the maximum sorption capacity of 33.06 mgP/g. From pH experiments, it was demonstrated that phosphate removal by calcined Mg-Fe LDHs was relatively constant at acidic, neutral, and weakly basic solution conditions. However, the phosphate sorption capacity decreased sharply as the solution pH approached a highly alkaline condition. Regeneration experiments demonstrated that calcined Mg-Fe LDH could be used repeatedly as adsorbents for phosphate removal through adsorption-desorption procedures. The thermodynamic analysis indicated that phosphate sorption to calcined Mg-Fe LDHs increased with increasing temperature from 15 to 45 °C, indicating the spontaneous and endothermic nature of sorption process. It was found that Elovich model was most suitable for describing the kinetic data, whereas Freundlich isotherm model was fitted well to the equilibrium data. It was found that phosphate removal in stream water was lower than that in the synthetic phosphate solution, possibly due to the presence of oxyanions, including nitrate, sulfate, and (bi)carbonate, in the stream water. This study showed that calcined Mg-Fe LDHs could be applied as adsorbents for phosphate removal from aqueous solutions with regeneration and reuse.

Chapter 6 Preparation and characterization of calcined Mg-Fe layered double hydroxide PVDF/PVA composites for phosphate removal from aqueous solutions

Due to low hydraulic conductivity and large sludge production, however, a powder form of LDHs might not be suitable in water treatment systems (Han *et al*., 2012). Thus, It was necessary to development of granular forms, such as composites containing LDHs for application as adsorbents. Also, Used CLDHs can be regenerated using a thermal recycle method or desorption-regeneration cycle method by NaOH solution (Ahmed and Gasser, 2012; Ashekuzzaman and Jiang, 2014).

Its excellent thermal stability and chemical resistance, PVDF was considered suitable polymer for immobilization of MgFe CLDHs. PVDF with an inorganic materials has been widely used as film form in membrane filtration and membrane distillation (Zhang *et al*., 2014). Granular type of PVDF composite had been seldom used in the adsorption. Yoon (2014) synthesized PVDF/PVA composite containing zeolite for removal of cations such as Cu(II) and Cr(III). In this chapter, granular type of MgFe CLDH-PVDF/PVA composites was synthesized and a series of experiments were carried out to investigate the removal of phosphate. To evaluate the phosphate removal capacity, batch and column experiments were performed using real stream water.

6.1. Materials and Methods

6.1.1. Synthesis of MgFe CLDH-PVDF/PVA composites

Polyvinylidene fluoride (PVDF) has features such as excellent chemical, physical resistance, thermal stability, high strength and

flexibility. However, hydrophobicity of PVDF limited its application in water treatment. Thus, hydrophilic modification needs to be conducted by blending with other polymeric materials. Polyvinyl alcohol (PVA) is well known for its hydrophilicity and miscibility with PVDF (Li *et al*., 2010). Polyethylene glycol (PEG) also act as a pore forming agent because it is water soluble and can be rinsed out (Meng *et al*., 2012). In this study, PVDF, PVA and PEG were used to synthesize Mg-Fe CLDH containing composites and dimethyl sulfoxide (DMSO) was used as a solvent for the composites.

All chemicals used for the experiments were purchased from Sigma Aldrich. Mg-Fe calcined layered double hydroxide (CLDH) was prepared by co-precipitation method. Polyvinylidene fluoride (PVDF) (11.2 wt.%), polyvinyl alcohol (PVA) (2.8 wt.%), polyethylene glycol (PEG) (6 wt.%) were added into round-bottom flask filled with 100mL of DMSO. After sealing the flask, the solution was heated in heating mantle with stirring at 85℃ for 12 h. Then, Mg-Fe CLDH (6 wt.%) was added to the solution under intensive stirring to obtain a homogeneous suspension. The suspension was filled in plastic syringe and dropped into deionized water using a syringe pump (78-1100I, Fisher Scientific) at 4 mL/min. To prepare composites for experiments, the composites were air-dried for 20 min.

6.1.2. Characterization of MgFe CLDH-PVDF/PVA composites

Field emission scanning electron microscopy (FESEM) analysis and

energy dispersive X-ray spectrometry (EDS) analysis were performed using a field emission scanning electron microscope (Supra 55VP; Carl Zeiss, Oberkochen, Germany). From the N_2 adsorption-desorption isotherms, the specific surface area, average pore diameter, total pore volume, and mesopore volume were determined using Brunauer-Emmett-Teller (BET), Barrett-Joyner-Halenda (BJH), and Horvath-Kawazoe (HK) analyses with an ASAP 2010 instrument (Micromeritics, Nocross, Georgia, USA).

6.1.3. Batch experiments

Phosphate removal by MgFe CLDH-polymer composites was conducted under batch conditions (Table 6.1). The phosphate solution was prepared using real stream water. The stream water samples were collected from the Seoho stream located in Suwon, Korea. The ionic composition of the stream water was analyzed using ion chromatograph (ICS-3000; Dionex, USA), and chemical oxygen demand (COD_{cr}) was measured according to standard method (APHA, 1995). The stream water had the following composition: NaCl=2.41 mM, $NaHCO_3$=0.38 mM, $Ca(HCO_3)_2$=0.67 mM, $CaSO_4$=0.17 mM, $MgSO_4$=0.20 mM, $Mg(NO_3)_2$=0.03 mM, KNO_3=0.32 mM, K_2HPO_4=1.77×10^{-4} mM, COD=4.2 mg/L, pH=6.9, IS=613 μS/cm. The stream water was passed through a 0.45 μm filter prior to the experiments in order to remove microorganisms and suspended particles. For the stream water sample, which had a very low phosphate concentration (0.017 mgP/L), potassium

dihydrogen orthophosphate (KH_2PO_4) was added to meet the initial P concentration of 100 mgP/L. The desired phosphate solution was prepared by diluting the stock solution.

The batch experiments were performed at 30 ^{o}C using 50 mL polypropylene conical tubes, unless otherwise stated. All of the batch experiments were performed in triplicate. To investigate dose effect of adsorbent, 5, 10, 20, 30, 40, 50 g/L of MgFe CLDH-polymer composites were added into 30 mL solution. The experiments were conducted at an initial phosphate concentration of 1, 2, 4, 8 mgP/L. The tubes were shaken at 30 ^{o}C and 100 rpm using a shaking incubator (Daihan Science, Seoul, Korea). After 12 h, the samples were collected and filtered through a 0.45 μm membrane filter. The phosphate was analyzed by the ascorbic acid method (APHA, 1995). The phosphate concentrations were measured at a wavelength of 880 nm using a UV–vis spectrophotometer (Helios, Thermo Scientific, Waltham, MA, USA).

For the pH experiments (adsorbent dose = 40 g/L; initial phosphate concentration = 2 mgP/L; temperature = 30 ^{o}C), 0.1 M NaOH and 0.1 M HCl solutions were used to adjust the pH of the reaction solution from 5.02 to 9.03. The pH was measured with a pH probe (9107BN, Thermo Scientific, USA).

To determine the effect of reaction time on the removal of phosphate, 40 g/L of adsorbents were added to 30 mL solution (initial phosphate concentration = 1, 2, 4, 8 mgP/L). In the experiments, samples were collected after various reaction times ranging from 15 min to 12 h. The additional experiments were performed at 15 and 45 °C to examine the effect of temperature on phosphate removal.

Further batch experiments were conducted at different initial concentration of phosphate solution. MgFe CLDH-polymer composites (dose = 5, 10, 20, 40 g/L) were added 30 mL of solution (initial phosphate concentration = 1 − 20 mgP/L). The sample were collected 12 h post-reaction.

The batch experiments were conducted to examined the repeated use of MgFe CLDH-polymer composite for phosphate sorption (adsorbent dose = 40 g/L; initial phosphate concentration = 2 mgP/L). For each round of the sorption experiments, desorption of the phosphate from MgFe CLDH-polymer composite was performed by dispersing the adsorbents in 1 M NaOH solution for 24 h. Then, adsorbents were air-dried for 20 min. After regeneration of the spent adsorbent, MgFe CLDH-polymer composite was reused for the sorption experiments.

Table 6.1 Batch experimental conditions for the phosphate sorption to MgFe CLDH-polymer composites.

	Dose (g/L)	Reaction Time (h)	Initial conc. (mgP/L)	Solution pH	Temperature (°C)	Solution volume (mL)
Effect of dosage	5 – 50	12	1 – 8		30	30
Effect of solution pH	40	12	2	5.0 – 9.0	30	30
Effect of reaction time	40	0.25 – 12	1 – 8		15 – 45	30
Effect of initial concentration	5 – 40	12	1 – 20		30	30
Effect of regeneration and use	40	12	2		30	30

6.1.4. Fixed-bed experiments

Column experiments were performed using a Plexiglas column (inner diameter = 2.5 cm; column length = 10, 20, 30 cm) packed with MgFe CLDH-polymer composite. For column experiments, a column was packed for each experiment with MgFe CLDH-polymer composite by the tap-fill method. Prior to the experiments, the packed column was flushed upward using a connected peristaltic pump (QG400, Fluid Metering Inc., Syosset, NY, USA) for 20 pore volumes of deionized water until steady state flow conditions were established. Then, the phosphate solution (initial concentration = 2 mgP/L) was introduced downward into the packed column at the same flow rate in a step injection mode.

Portions of the effluent were collected using an autocollector (Retriever 500, Teledyne, City of Industry, CA, USA) at regular intervals. The effluent pH was measured with a pH probe (9107BN, Thermo Scientific, Waltham, MA, USA) and the electrical conductivity (EC) was measured with an EC probe (815PDL, Istek, Korea). The experimental conditions are provided in Table 6.2.

Table 6.2 Fixed-bed experimental conditions for the phosphate sorption to MgFe CLDH-polymer composites.

Ex.	Phosphate solution	Initial conc. (mgP/L)	Linear velocity (cm/min)	Flow rate (mL/min)	Bed depth (cm)	Bed volume (cm^3)	EBCT (min)	Pore volume (cm^3)	Mass of adsorbent (g)	pH$_{effluent}$	EC$_{effluent}$ (µS/cm)
1	Stream water	2	2	0.0098	10	49.09	5	13.49	43.3	8.15±0.31	575.76±46.50
2	Stream water	2	1	0.0049	10	49.09	10	15.54	40.8	8.21±0.14	555.37±60.09
3	Stream water	1	1	0.0049	10	49.09	10	15.54	40.8	8.22±0.21	569.86±26.29
4	Synthetic water	2	1	0.0049	10	98.17	20	31.01	40.8	8.13±0.31	537.94±52.41
5	Stream water	2	1	0.0049	20	49.09	10	15.54	81.7	8.26±0.09	554.40±39.54
6	Stream water	2	1	0.0049	30	147.26	30	46.63	122.4	8.29±0.09	543.46±49.82

6.2. Results and Discussion

6.2.1. Characteristics of MgFe CLDH-PVDF/PVA composites

The digital image of calcined MgFe CLDH-polymer composites are presented in Figure 6.1. The composites had a sphere shape with a particle size of 2.4±0.1 mm.

The FESEM images of MgFe CLDH-polymer composite are presented in Figure 6.2. It demonstrated that the cross-sectional surface of MgFe CLDH-polymer composite was heterogeneous in surface topography. The EDS pattern demonstrated that magnesium (Mg), iron (Fe), oxygen (O), and carbon(c) were the major elements of the MgFe CLDH-polymer composite. Magnesium was found on the MgFe CLDH-polymer composite at the peak positions of 1.25 keV as K-alpha X-ray signal. In addition, iron was evident at the peak position of 0.71 and 6.40 keV as L alpha, K alpha signals, respectively in Figure 6.3.

The physical properties of the MgFe CLDH-polymer composites from the N_2 adsorption-desorption data are summarized in Table 6.3. The MgFe CLDH-polymer composites had the BET specific surface area of 30.41 m^2/g, total pore volume of 0.12 cm^3/g, mesopore volume of 0.11 cm^3/g and micropore volume of 0.02 cm^3/g.

Figure 6.1 Digital image of MgFe CLDH-polymer composites.
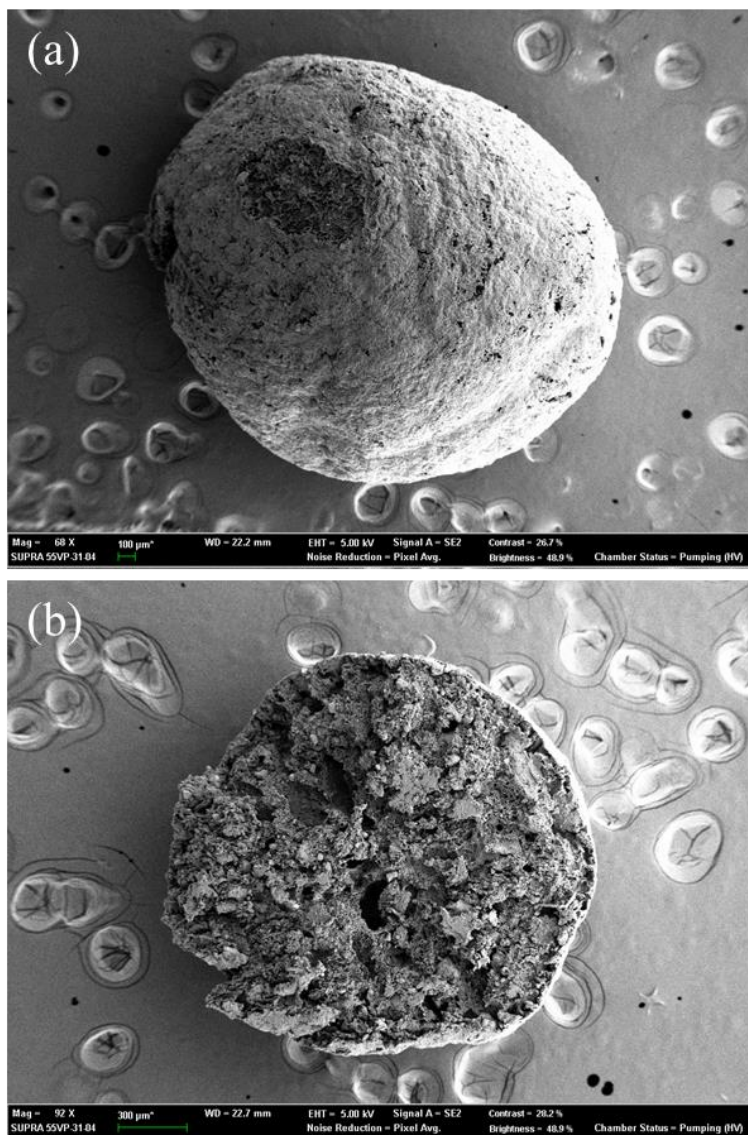
Figure 6.2 Field emission scanning electron microscope (FESEM) images of MgFe CLDH-polymer composite: (a) surface area; (b) cross section area.
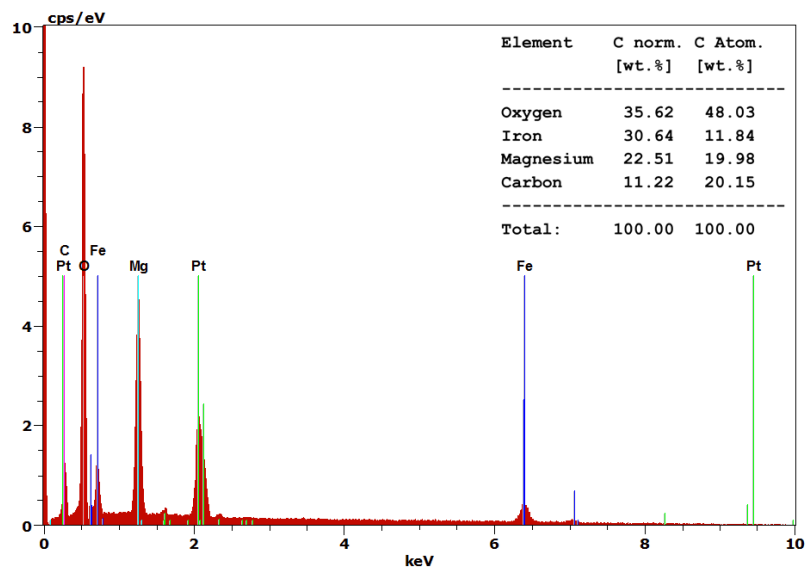
Figure 6.3 Energy dispersive X-ray spectrometer (EDS) pattern of
MgFe CLDH-polymer composite.

Table 6.3 Physical characteristics of the MgFe CLDH-polymer composite obtained from the N_2 adsorption–desorption data.

Characteristics	Value	Unit
Brunauer–Emmett–Teller (BET) analysis		
Monolayer volume (V_m)	7.0	cm^3/g
BET specific surface area ($a_{s,BET}$)	30.4	m^2/g
BET constant	51.7	-
Total pore volume (V_p)	0.12	cm^3/g
Average pore diameter ($d_{p,ave}$)	15.3	nm
Barrett–Joyner–Halenda (BJH) analysis		
Mesopore volume ($V_{p,me}$)	0.11	cm^3/g
Peak diameter of mesopore ($d_{p,me}$)	43.6	nm
Horvath–Kawazoe (HK) analysis		
Micropore volume ($V_{p,mi}$)	0.02	cm^3/g
Peak diameter of micropore ($d_{p,mi}$)	0.9	nm

6.2.2. Batch adsorption of phosphate

The phosphate removal by the MgFe CLDH-polymer composites as a function of adsorbent dose (initial P concentration = 1, 2, 4, 8 mgP/L; adsorbent dose = 5 – 50 g/L; reaction time = 12 h) is shown in Figure 6.4. The percent removal increased with a rise in the adsorbent dose from 5 to 50 g/L. When the initial P concentration was 2 mgP/L, the percent removal was 52.9% at the MgFe CLDH-polymer composites dose of 5 g/L and 99.9% at a dose of 50 g/L. The sorption capacity decreased with increasing adsorbent dose from 5 to 50 g/L. When the initial P concentration was 2 mgP/L, the sorption capacity was 0.20 mgP/g at 5 g/L, and then decreased to 0.09 mgP/g at 20 g/L. The sorption capacity decreased to 0.05 mgP/g at 40 g/L, decreasing further to 0.04 mgP/g at 2.0 g/L.

The effect of the initial solution pH on phosphate removal by MgFe CLDH-polymer composites (initial phosphate concentration = 2 mgP/L; adsorbent dose = 40 g/L; reaction time = 12 h) is shown in Figure 6.5. The sorption capacity at pH 5.02 was 0.046 mgP/g and remained at 0.045 – 0.047 mgP/g up to pH 9.03. The results indicate that phosphate removal was relatively constant at acidic and alkaline pHs.

The effect of the reaction time on phosphate removal by MgFe CLDH-polymer composites (initial P concentration = 1, 2, 4, 8 mgP/L; adsorbent dose = 40 g/L) is shown in Figure 6.6. At an initial P concentration of 1 mgP/L, the sorption capacity gradually increased, reaching 0.02 mgP/g after a reaction time of 12 h. As the initial P concentration was increased from 1 to 8 mgP/L, the sorption capacity at 12 h increased from 0.02 to 0.18 mg P/g.
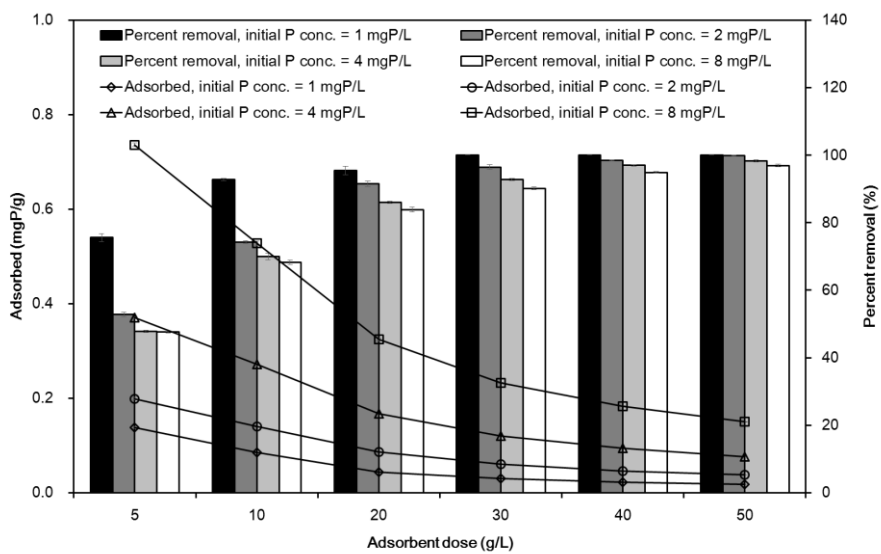
Figure 6.4 Effect of MgFe CLDH-polymer composite dose on removal of phosphate.
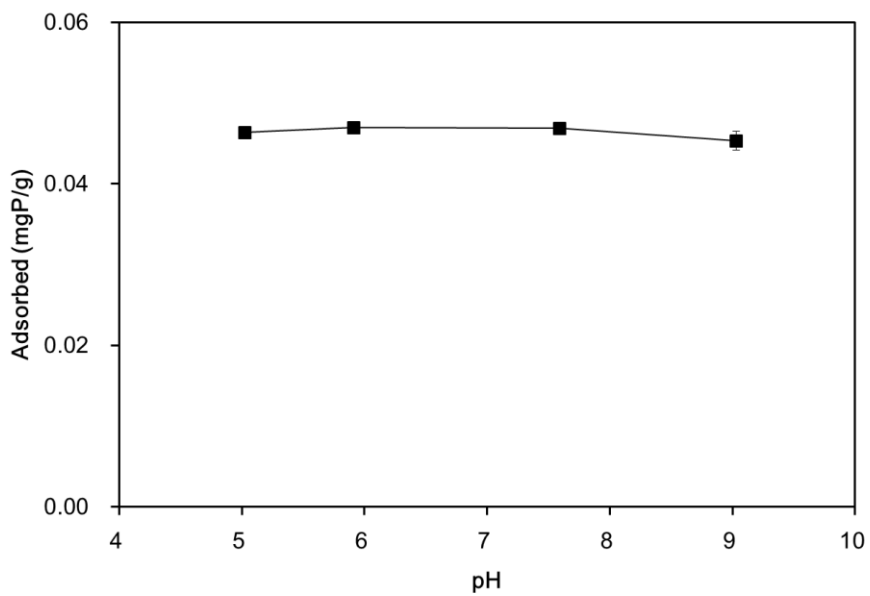
Figure 6.5 Effect of solution pH on phosphate removal by MgFe CLDH-polymer composites (adsorbent dose = 40 g/L; initial concentration = 2 mgP/L).
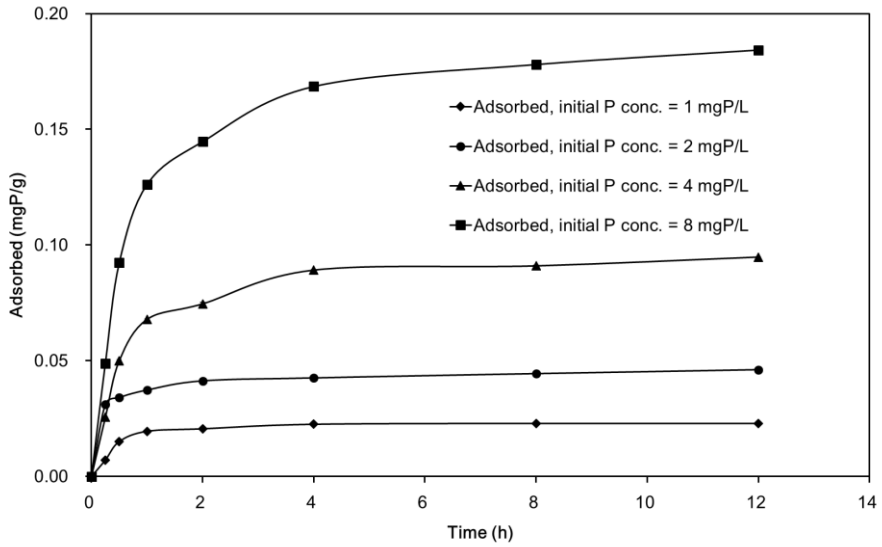
Figure 6.6 Phosphate removal by MgFe CLDH-polymer composite as a
function of reaction time (adsorbent dose = 40 g/L).

The effect of reaction temperature on the removal of phosphate by MgFe CLDH-polymer composites (initial P concentration = 2 mgP/L; adsorbent dose = 40 g/L) is presented in Figure 6.7. The sorption capacity was increased with increasing reaction temperature. At 15°C, the sorption capacity was 4.58×10^{-2} mgP/g with a percent removal of 97.6%. When the temperature was raised to 30°C, the sorption capacity increased slightly to 4.61×10^{-2} mgP/g with an increase in the percent removal to 99.3%. At 45°C, the sorption capacity further increased to 4.81×10^{-2} mgP/g with the percent removal reaching 100%. These results demonstrated that the phosphate removal process was endothermic.

The effect of the initial phosphate concentration on phosphate removal by MgFe CLDH-polymer composites (adsorbent dose = 5, 10, 20, 40 g/L; reaction time = 12 h) is presented in Figure 6.8. The percent removal decreased with a rise in the initial phosphate concentration at all MgFe CLDH-polymer composites dosages. At a dose of 5 g/L, the percent removal decreased from 71.2 to 37.5% with an increase in the initial phosphate concentration from 1 to 20 mgP/L. For a 20 g/L dose, the percent removal decreased from 96.5 to 71.7% over the same phosphate concentration range. In the case of a 40 g/L dose, the percent removal was 100% at initial phosphate concentration of 1 mgP/L, but decreased 77.3% at initial phosphate concentration of 20 mgP/L. Meanwhile, the sorption capacity increased with a rise in the initial phosphate concentration at all dosages. For example, the sorption capacity at 40 g/L increased from 0.02 to 0.37 mgP/g as the initial phosphate concentration was increased from 1 to 20 mgP/L.
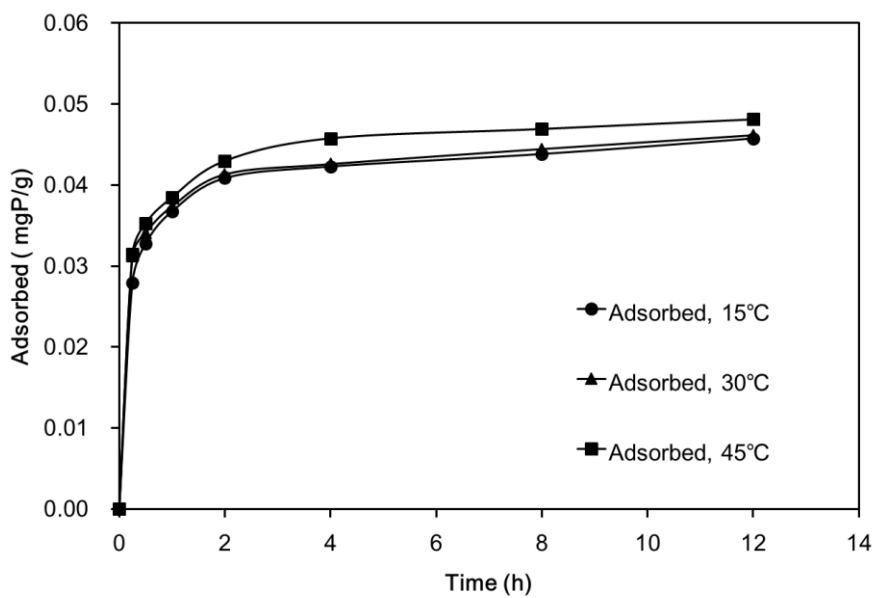
Figure 6.7 Effect of reaction temperature on phosphate removal by MgFe CLDH-polymer composite (adsorbent dose = 40 g/L; initial concentration = 2 mgP/L).
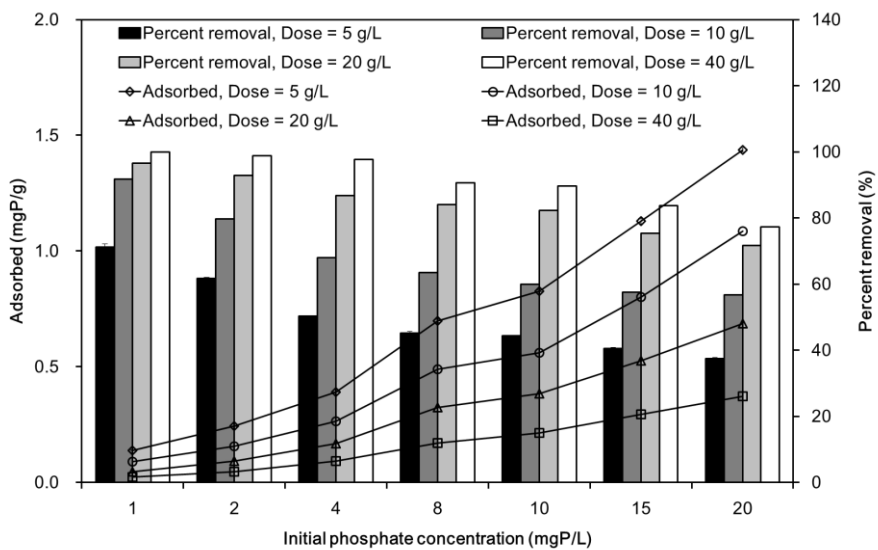
Figure 6.8 Phosphate removal by MgFe CLDH-polymer composite as a function of initial concentration (reaction time = 12 h).

Effect of desorption and reuse on phosphate removal by MgFe CLDH-polymer composites (initial phosphate concentration = 2 mgP/L; adsorbent dose = 40 g/L; reaction time = 12 h) is presented Figure 6.9. In the first adsorption, the sorption capacity was determined to be 4.65×10^{-2} mgP/g. In the first desorption, the recovery rate was 90.3%. In the second cycle, the sorption capacity was reduced to 4.57×10^{-2} mgP/g, whereas the recovery rate from desorption was 94.0%. The sorption capacity was reduced to 4.38×10^{-2} mgP/g in the third cycle with 81.4% recovery.
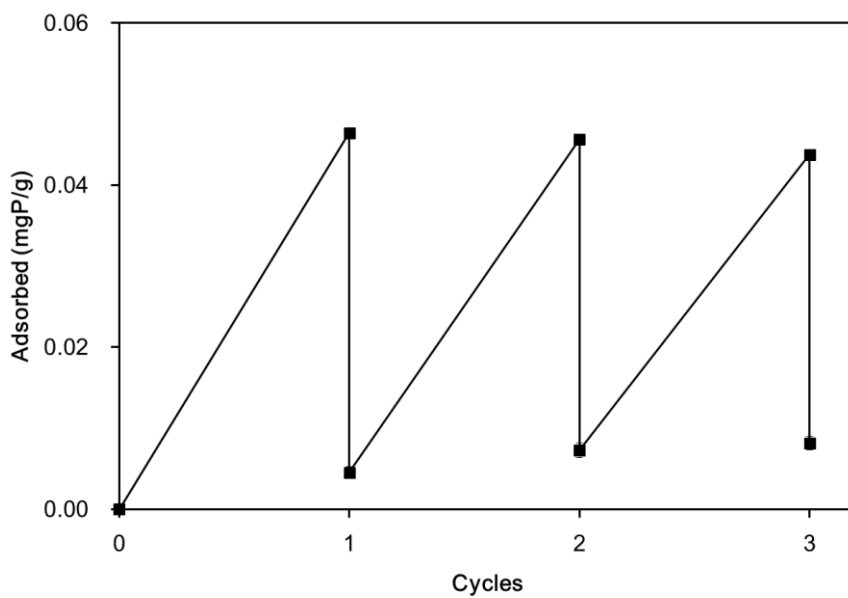
Figure 6.9 Effect of desorption and reuse on phosphate removal by MgFe CLDH-polymer composites (adsorbent dose = 40 g/L; initial concentration = 2 mgP/L).

6.2.3. Kinetic, isotherm and thermodynamic model analyses

The results from the kinetic model analyses are presented in Figure 6.10, while the kinetic model parameters are provided in Table 6.4. When the initial P concentration was 1 mgP/L, from the obtained values of R^2, χ^2, and SAE, it was concluded that the pseudo first order model (Figure 6.10(a)) was most suitable for describing the kinetic data. Meanwhile, when the initial P concentration was 2 mgP/L, the values of R^2, χ^2, and SAE indicate that the Elovich model (Figure 6.10(c)) was most suitable at describing the kinetic data. When the initial P concentration was 4 and 8 mgP/L, the values of R^2, χ^2, and SAE, it was concluded that the pseudo second order model (Figure 6.10(b)) was most suitable for describing the kinetic data. This finding indicates that chemisorption is involved in the adsorption of phosphate to MgFe CLDH-polymer composites.

The intra-particle diffusion model applied to the data is shown in Figure 6.11, indicating that the plots were composed of three line segments. The first line in the plot indicates the diffusion of solute through the solution to the external surface of adsorbent, or the boundary layer diffusion of solute molecules. The second portion described the gradual adsorption stage, where in intra-particle diffusion was rate limiting. The third line indicates the final equilibrium stage for which the intra-particle diffusion started to slow down due to the extremely low solute concentration left in the solution. (Cheung *et al*., 2007) The intra-particle diffusion model parameters are provided in Table 6.5.
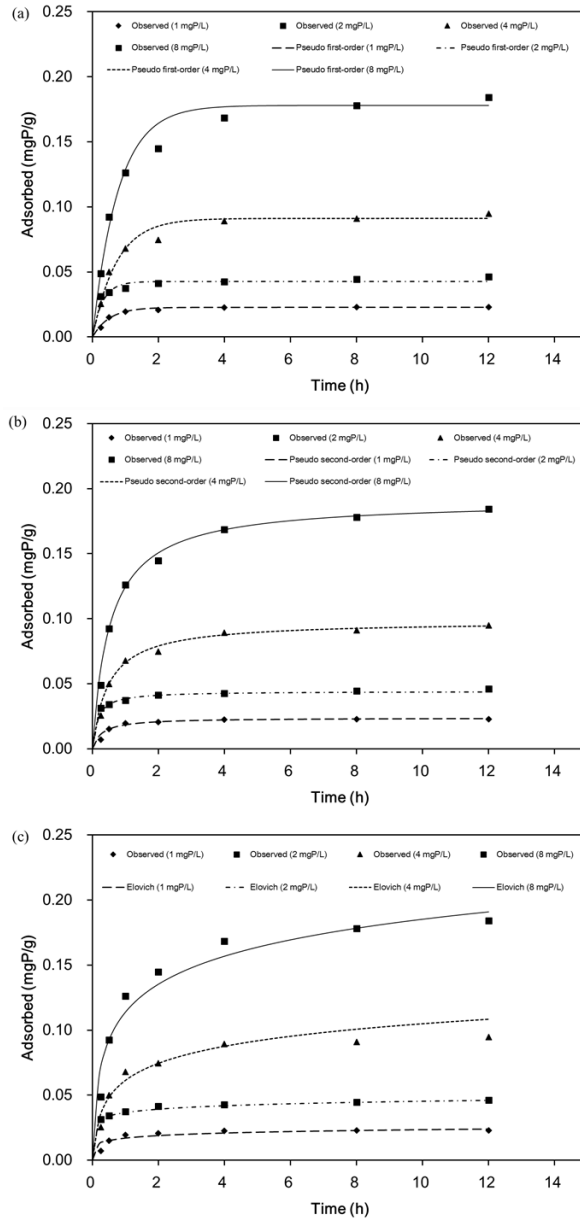
Figure 6.10 Kinetic model fits for phosphate removal to MgFe CLDH-polymer composites: (a) pseudo first-order model; (b) pseudo second-order model; (c) Elovich model.

Table 6.4 Kinetic model parameters obtained from model fitting to MgFe CLDH-polymer composites experimental data.

Initial conc. (mgP/L)	Pseudo first-order model				
	q_e (mgP/g)	k_1 (1/h)	R^2	χ^2	SAE
1	0.023	1.943	0.972	0.001	0.005
2	0.423	3.228	0.761	0.003	0.018
4	0.091	1.370	0.963	0.002	0.022
8	0.178	1.282	0.969	0.004	0.045

Initial conc. (mgP/L)	Pseudo second-order model				
	q_e (mgP/g)	k_2 (g/mgP/h)	R^2	χ^2	SAE
1	0.024	146.904	0.959	0.002	0.006
2	0.044	150.413	0.927	0.001	0.008
4	0.098	21.137	0.986	0.002	0.018
8	0.191	9.797	0.993	0.003	0.022

Initial conc. (mgP/L)	Elovich model				
	α (mgP/g/h)	β (g/mgP)	R^2	χ^2	SAE
1	1.196	355.057	0.798	0.0034	0.013
2	61.029	263.677	0.981	0.0001	0.004
4	0.487	52.818	0.923	0.0061	0.043
8	1.217	32.237	0.945	0.0099	0.062
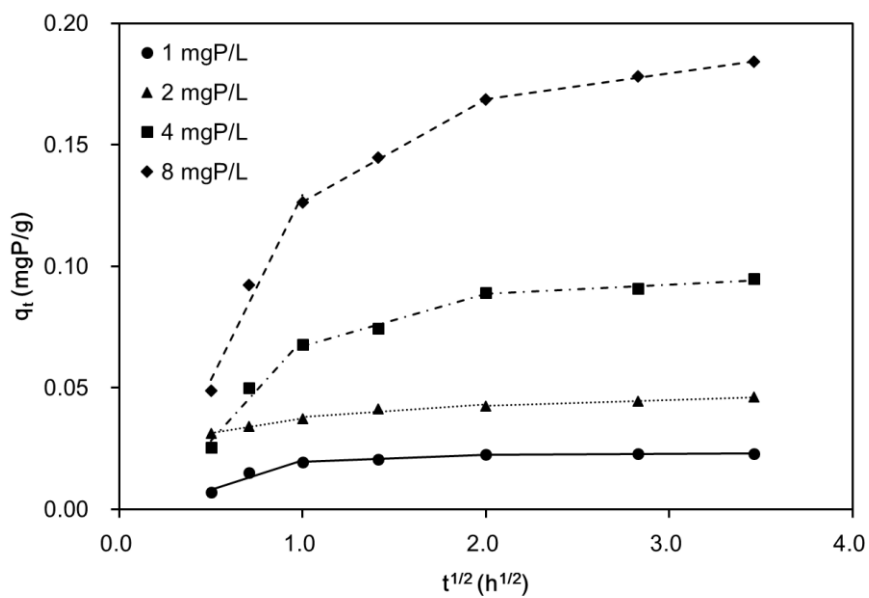
Figure 6.11 Intra-particle diffusion model for phosphate removal to MgFe CLDH-polymer composites.

Table 6.5 Intra-particle diffusion model parameters obtained from model fitting to MgFe CLDH-polymer composites experimental data.

Initial P concentration	1 mgP/L	2 mgP/L	4 mgP/L	8 mgP/L
$k_{i,1}$ $(mg/g/h^{0.5})$	0.024	0.012	0.083	0.152
I	0.000	0.025	0.000	0.000
R^2	0.932	0.996	0.965	0.971
$k_{i,2}$ $(mg/g/h^{0.5})$	0.003	0.005	0.022	0.042
I	0.016	0.033	0.046	0.084
R^2	0.996	0.857	0.988	0.999
$k_{i,3}$ $(mg/g/h^{0.5})$	0.000	0.002	0.004	0.011
I	0.022	0.038	0.081	0.147
R^2	0.813	0.997	0.927	0.998

The thermodynamic analysis results are shown in Figure 6.12, and thermodynamic parameters are provided in Table 6.6. The positive value of $\Delta H°$ (499.33 kJ/mol) indicates that phosphate removal by MgFe CLDH-polymer composites is an endothermic process, while the positive value of $\Delta S°$ (1739.38 J/K/mol) suggests that the degree of randomness increased at the interface between the solid and solution during the removal process. The negative values of $\Delta G°$ (-1.89 to -54.07 kJ/mol) indicate that the phosphate removal process was spontaneous.

The equilibrium isotherm model analyses are presented in Figure 6.13, while the corresponding equilibrium model parameters are provided in Table 6.7. The values of R^2, χ^2, and SAE indicated that the Redlich–Peterson model was suitable for describing the equilibrium data. Parameter values of $K_R/a_R = 0.215 - 0.281$ mgP/g and $g = 0.260 - 0.627$ were determined from the Redlich–Peterson model. The Redlich–Peterson model is an empirical model that combines the Freundlich and Langmuir equations to explain adsorption over a wide range of concentrations. When g is close to unity, the expression reduces to the Langmuir equation (Foo and Hammed, 2010).
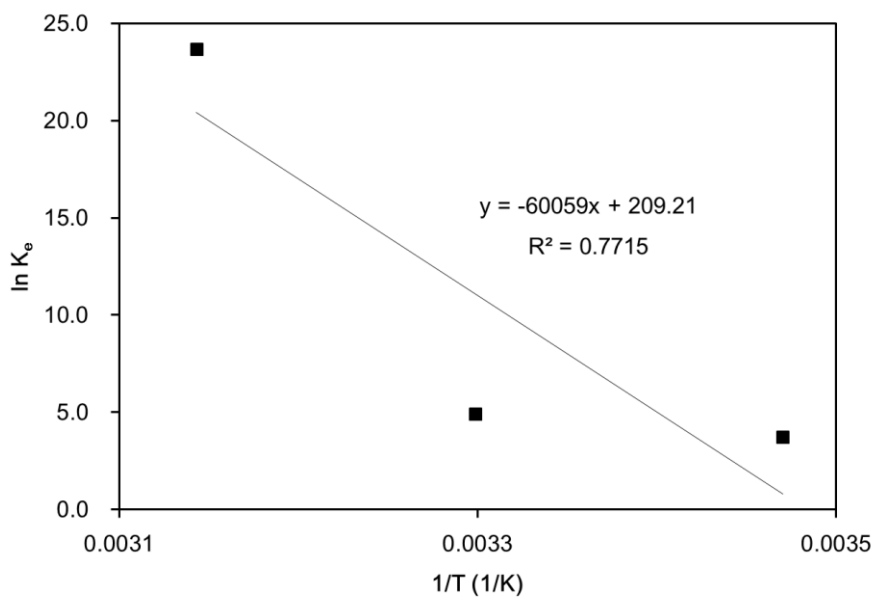
Figure 6.12 Thermodynamic analysis for phosphate adsorption to calcined MgFe CLDH-polymer composites.

Table 6.6 Thermodynamic parameters for phosphate adsorption to MgFe CLDH-polymer composites.

Temp. (℃)	ΔH° (kJ/mol)	ΔS° (J/K/mol)	ΔG° (kJ/mol)
15	499.33	1739.38	-1.89
30			-27.98
45			-54.07
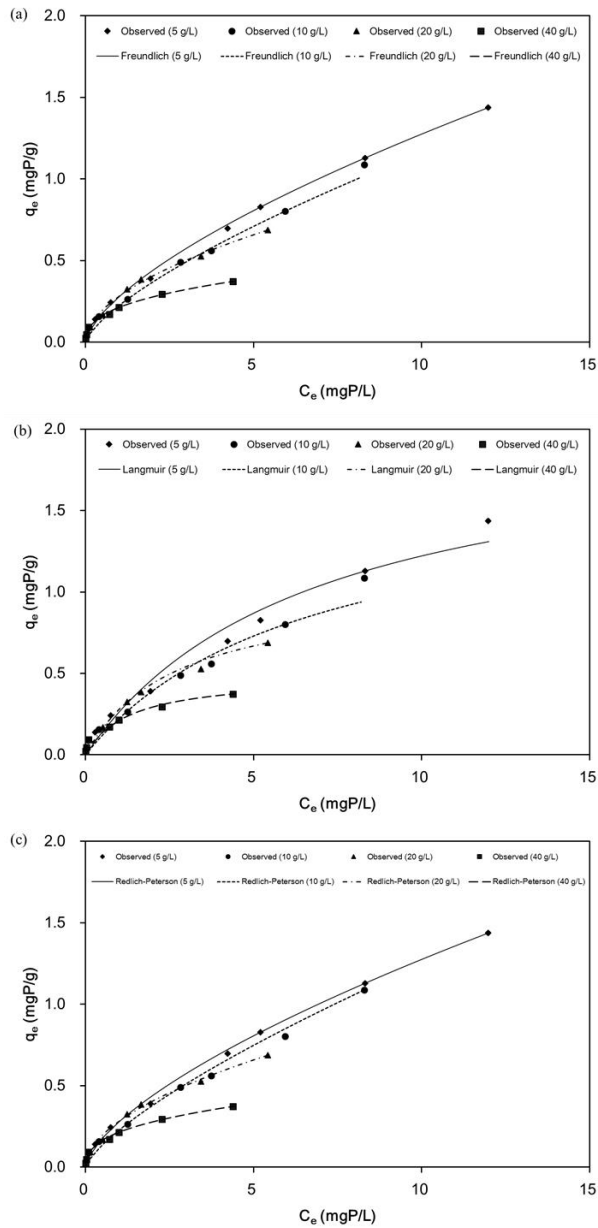
Figure 6.13 Equilibrium isotherm model fits for phosphate removal to MgFe CLDH-polymer composites: (a) Freundlich model; (b) Langmuir model; (c) Redlich-Peterson model.

Table 6.7 Equilibrium isotherm model parameters obtained from model fitting to MgFe CLDH-polymer composites experimental data.

Dose (g/L)	Freundlich model				
	K_F (L/g)	$1/n$	R^2	χ^2	SAE
5	0.278	0.661	0.998	0.008	0.095
10	0.225	0.714	0.993	0.092	0.195
20	0.281	0.529	0.996	0.007	0.080
40	0.214	0.376	0.993	0.003	0.055

Dose (g/L)	Langmuir model				
	Q_m (mgP/g)	K_L (L/mgP)	R^2	χ^2	SAE
5	2.050	0.147	0.973	0.084	0.439
10	1.701	0.150	0.967	0.298	0.347
20	1.026	0.373	0.993	0.126	0.134
40	0.484	0.768	0.985	0.289	0.142

Dose (g/L)	Redlich-Peterson model					
	K_R (L/g)	a_R (L/mgP)	g	R^2	χ^2	SAE
5	145.398	521.942	0.339	0.998	0.008	0.095
10	275.249	1211.068	0.260	0.994	0.104	0.189
20	434.102	1544.978	0.471	0.996	0.007	0.080
40	676.052	3149.036	0.627	0.991	0.003	0.054

6.2.4. Fixed-bed adsorption of phosphate

Breakthrough curves(BTCs) obtained from the fixed-bed experiments are shown in Figure 6.14. The results of the column experiments are provided in Table 6.8. With increasing flow rate from 0.49 mL/min (experiment 2) to 0.98 mL/min (experiment 1), Steeper BTC were observed. As the flow rate increases, the contact time between the phosphate and the filter medium decreases. EBCT decreased from 10 min (experiment 2) to 5 min (experiment 1) as the flow rate was increased (column length = 10 cm). As the flow rate increases, the BTC becomes steeper because the driving forces increase, leading to a decrease in the adsorption zone length (Han *et al*., 2008). Increasing the flow rate decreased the phosphate adsorption capacity from 0.588 mgP/g (experiment 2) to 0.521 mgP/g (experiment 1).

In addition, with increasing phosphate concentration from 1.0 mgP/L (experiment 5) to 2.0 mgP/L (experiment 2), the BTCs became steeper and saturation was achieved more quickly. As the influent concentration increased, the phosphate adsorption capacity decreased from 0.635 mgP/g (experiment 5) to 0.588 mgP/g (experiment 2). Compared with synthetic solution (experiment 3), stream water (experiment 2) has steeper BTC.

The total removal percentage(Re) increased with increasing bed depth from 10 to 30cm. The total removal percentage was 29.18% at bed depth = 10cm (experiment 2), and then increased to 34.83% at bed depth = 20cm (experiment 5), increasing further to 41.83% at bed depth = 30cm (experiment 6).
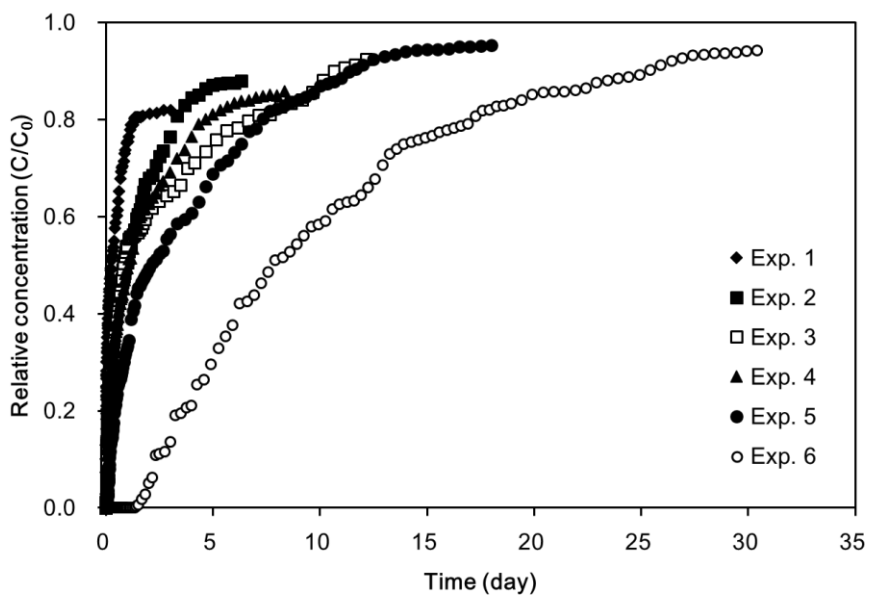
Figure 6.14 Breakthrough curves of phosphate obtained from the fixed-bed experiments.

Table 6.8 Results from column experiments for the phosphate sorption to MgFe CLDH-polymer composites.

Ex.	m_{total} (mgP)	q_{total} (mgP)	Re (%)	q_{eq} (mgP/g)
1	84.25	22.54	26.76	0.521
2	84.81	24.01	28.31	0.588
3	73.71	21.07	28.58	0.516
4	114.92	33.53	29.18	0.822
5	148.99	51.89	34.83	0.635
6	343.92	143.85	41.83	1.175

6.2.5. Conclusions

MgFe CLDH-polymer composites were synthesized and used for phosphate removal in this chapter. Kinetic experiments indicated that phosphate removal by the composites reached equilibrium at 12 h with a high removal percentage. The phosphate removal by MgFe CLDH-polymer composites was relatively stable over acidic and alkaline pHs. The composites were regenerated three cycles and sorption capacity was remained almost constant. Whereas recovery rate was decreased to 81.4% after three cycles of regeneration.

The column experiments showed that the adsorption capacities of MgFe CLDH-polymer composites were in the range of 0.52 – 1.18 mgP/g in the given experimental conditions. As the influent concentration increased, the phosphate sorption capacity decreased in fixed-bed adsorption. The total removal percentage was increased from 29.18% at bed depth = 10cm to 41.83% at bed depth = 30cm.

These results demonstrated that MgFe CLDH-polymer composites had chemical stability and potential for phosphate removal as adsorbents.

Chapter 7 Removal of phosphate and fluoride from aqueous solution by quintinite particles

Quintinite is a carbonate mineral with hexagonal crystal system. It has a chemical formula of $Mg_4Al_2(OH)_{12}CO_3 \cdot 3H_2O$, which is included in the family of hydrotalcite-like (HTL) particles (Delorme *et al*., 2007). HTL particles consist of positively charged brucite-like layers and negatively-charged interlayers and can be easily synthesized in the laboratory. They are a class of anionic clays with high surface area and large anion exchange capacity (Goh *et al*., 2008). The aims of this chapter were to characterize quintinite in phosphate and fluoride removal from aqueous solutions.

7.1. Materials and Methods

7.1.1. Synthesis of quintinite

All chemicals used for the experiments were purchased from Sigma Aldrich. Quintinite particles were prepared by the following procedures. The particles were synthesized by co-precipitating mixtures of magnesium nitrate $[Mg(NO_3)_2 \cdot 6H_2O]$ and aluminum nitrate $[Al(NO_3)_3 \cdot 9H_2O]$. A 700 mL solution (Mg/Al molar ratio = 2) of $Mg(NO_3)_2 \cdot 6H_2O$ (1 mol) and $Al(NO_3)_3 \cdot 9H_2O$ (0.5 mol) was added dropwise using a peristaltic pump (QG400, Fasco, Springfield, MO, USA) at 3 mL/min into 1,000 mL of alkali solution (pH = 13) consisting of sodium hydroxide (NaOH) and sodium carbonate (Na_2CO_3) with intensive stirring at room temperature. The resulting precipitates were aged at 65 ^{o}C for 18 h in mother liquor. The precipitates were washed thoroughly with deionized water to remove excess sodium, and then final

suspensions were centrifuged at 8,500 rpm for 20 min. The washed precipitates were oven-dried again at 65 °C for 24 h and then pulverized in a ball mill. The pulverized precipitates were passed through US Standard Sieve No. 100 (grain size: 0.149 mm). The particles used for the experiments were finally obtained through oven dry at 105 °C.

7.1.2. Characterization of quintinite

TEM (JEM-1010, JEOL, Tokyo, Japan) was used to take images of the particles. The particle size was determined by the analysis of the TEM image (number of particle = 71) using ImageJ 1.43u software (National Institutes of Health, Bethesda, MD, USA). The mineralogical and crystalline structural properties were examined using XRD (D8 Advance, Bruker, Germany) with a CuKα radiation of 1.5406 Å at a scanning speed of 0.6°/sec. N_2 adsorption-desorption experiments were performed using a surface area analyzer (BELSORP-max, BEL Japan Inc., Japan) after the sample was pretreated at 120 °C. From the N_2 adsorption-desorption isotherms, the specific surface area, total pore volume, and mesopore volume were determined by Brunauer-Emmett-Teller (BET) and Barrett-Joyner-Halenda (BJH) analyses. XPS (XPS Sigma Probe, Thermo VG, UK) measurement was performed with monochromatic Al Kα radiation.

7.1.3. Stream water samples

The stream water samples were collected from the Seoho stream located in Suwon, Korea. The ionic composition of the stream water was analyzed using ion chromatograph (ICS-3000; Dionex, USA), and chemical oxygen demand (COD_{cr}) was measured according to standard method (APHA, 1995).

The stream water had the following composition: NaCl=2.41 mM, $NaHCO_3$=0.38 mM, $Ca(HCO_3)_2$=0.67 mM, $CaSO_4$=0.17 mM, $MgSO_4$=0.20 mM, $Mg(NO_3)_2$=0.03 mM, KNO_3=0.32 mM, K_2HPO_4=1.77×10^{-4} mM, COD=4.2 mg/L, pH=6.9, IS=613 μS/cm. The stream water was passed through a 0.45 μm filter prior to the experiments in order to remove microorganisms and suspended particles. For the stream water sample, which had a very low phosphate concentration (0.017 mgP/L), potassium dihydrogen orthophosphate (KH_2PO_4) was added to meet the initial P concentration of 100 mgP/L. The desired phosphate solution was prepared by diluting the stock solution.

Table 7.1 Characteristics of stream water samples.

Components	Values
NaCl (mM)	2.41
NaHCO$_3$ (mM)	0.38
Ca(HCO$_3$)$_2$ (mM)	0.67
CaSO$_4$ (mM)	0.17
MgSO$_4$ (mM)	0.20
Mg(NO$_3$)$_2$ (mM)	0.03
KNO$_3$ (mM)	0.32
K$_2$HPO$_4$ (mM)	1.77×10^{-4}
COD$_{Cr}$ (mg/L)	4.2
pH	6.9
IS (μS/cm)	613

7.1.4. Batch experiments

Phosphate removal by the quintinite was conducted under batch conditions. The desired phosphate (P) solution was prepared by diluting the stock solution (1,000 mgP/L) that had been made from potassium dihydrogen orthophosphate (KH_2PO_4). The batch experiments were performed at 30 ^{o}C using 50 mL polypropylene conical tubes, unless otherwise stated. All of the batch experiments were performed in triplicate.

The first set of experiments were performed at the different dosages of adsorbent (quintinite) ranging from 0.2 to 2.0 g in 30 mL solution. The tubes were shaken at 100 rpm using a shaking incubator (Daihan Science, Seoul, Korea). After 24 h, the samples were collected and filtered through a 0.45 μm membrane filter. The phosphate concentration was analyzed by the ascorbic acid method (APHA, 1995). The phosphate concentrations were measured at a wavelength of 880 nm using a UV–vis spectrophotometer (Helios, Thermo Scientific, Waltham, MA, USA).

The second set of experiments was performed as a function of reaction time (adsorbent dose = 1.2 g/L; initial P concentration = 2 mgP/L). The additional experiments were performed at 15 and 45 ^{o}C to examine the effect of temperature on phosphate removal.

The third set of experiments was conducted as a function of the initial P concentration. Quintinite particles (1.2 g/L) were added to 30 mL of phosphate solution (initial concentration = 2 − 20 mgP/L), and the samples were collected 4 h later.

The fourth set of experiments examined phosphate removal as a function of initial solution pH (adsorbent dose = 1.2 g/L; initial P

concentration = 2 mgP/L); 0.1 M NaOH and 0.1 M HCl solutions were used to adjust the pH of the reaction solution from 2.0 to 11.0, and the pH was measured by a pH probe (9107BN, Thermo Scientific, USA).

The fifth set of experiments performed to compare the phosphate removal in synthetic water solution and real stream water sample. Synthetic water solutions were prepared using deionized water in the laboratory, whereas real water samples were collected from the Seoho stream located in Suwon, Korea. The ionic composition of the stream water was analyzed using ion chromatograph (Dionex, ICS-3000), and chemical oxygen demand (CODcr) was measured according to standard method (APHA, 1995). The experiments were conducted at an initial P concentration of 2 mgP/L with an adsorbent dose of 0.8 g/L in 30 mL of solution. In the case of the stream water sample, which had a very low phosphate concentration (0.017 mgP/L), phosphate was added to meet the initial P concentration of 2 mgP/L.

Fluoride removal by the quintinite was also conducted under batch conditions. The desired fluoride solution was prepared by diluting the stocking fluoride solution (1,000 mgF/L), which was made from sodium fluoride (NaF). The first batch experiments were performed at the different dosages of adsorbent ranging from 0.1 to 2.0 g in 30 mL solution. Adsorbent was added to 30 mL of fluoride solution (initial concentration = 10 mgF/L) in 50 mL polypropylene conical tubes. The tubes were shaken at 25 ℃ and 100 rpm using a culture tube rotator (MG-150D, Mega Science, Korea). The samples were collected 6 h after the reaction and were filtered through a 0.45 μm membrane filter. The fluoride concentration was measured using a fluoride ion selective

electrode (9609BNWP, Thermo Scientific, USA). For the fluoride measurement, total ionic strength adjustment buffer solution (58 g of NaCl, 57 mL of CH_3COOH, 150 mL of 6 M NaOH in 1,000 mL of deionized water) was used to prevent the interference of other ions.

Based on the results from the above tests, further batch experiments were conducted at the adsorbent dose of 1.5 g in 30 mL solution. The second batch experiments were performed at the initial fluoride concentrations of 10 mgF/L to examine the effect of contact time on fluoride removal. In the experiments, the samples were collected 1, 2, 3, 6, 9, 12, and 24 h after the reaction.

The third batch experiments were conducted at fluoride concentrations of 10 – 1,000 mgF/L to examine the effect of initial fluoride concentrations on fluoride removal. The samples were collected 6 h after the reaction for the fluoride measurement.

The fourth batch experiments were performed to examine the effect of initial solution pH, which was adjusted to the desired value with 0.1 M NaOH and/or 0.1 M HCl. All experiments were performed in triplicate.

Table 7.2 Batch experimental conditions for the phosphate sorption to quintinite.

	Dose (g/L)	Reaction Time (h)	Initial conc. (mgP/L)	Solution pH	Temperature (°C)	Solution volume (mL)
Effect of dosage	0.2 – 2.0	24	2		30	30
Effect of reaction time	1.2	0.08 – 24	2		15 – 45	30
Effect of initial concentration	1.2	4	2 – 20		30	30
Effect of solution pH	1.2	4	2	2.0 – 11.0	30	30
Comparison between synthetic solution and stream water	1.2	4	2		30	30

Table 7.3 Batch experimental conditions for the fluoride sorption to quintinite.

	Dose (g/L)	Reaction Time (h)	Initial conc. (mgF/L)	Solution pH	Temperature (°C)	Solution volume (mL)
Effect of dosage	3.3 – 66.7	6	10		25	30
Effect of solution pH	50	12	2	3.0 – 11.0	25	30
Effect of reaction time	50	1 – 24	10		25	30
Effect of initial concentration	50	6	10 – 1,000		25	30

7.2. Results and Discussion

7.2.1. Characteristics of quintinite

The characteristics of quintinite particles are presented in Figure 7.1. The TEM image (Figure 7.1(a)) demonstrates that the particles were nano-sized. The particle size distribution (Figure 7.1(b)) determined from the TEM image shows that the particle size was in the range from 20 to 120 nm with the mean particle size of 59 nm.

Energy dispersive X-ray spectrometer (EDS) analysis was also performed using the FESEM (Figure 7.2). The EDS pattern (Figure 7.2(b)) demonstrates that magnesium (Mg) and aluminum (Al) were the major elements of the particles. The atomic weight percents of Mg and Al were 21.14 and 10.38%, respectively. In the EDS analysis, Mg was evident at the peak position of 1.254 keV as K alpha X-ray signal, while Al was found at the peak position of 1.485 keV as K alpha X-ray signal (Figure 7.2(b)).

According to the XRD pattern (Figure 7.3(a)), the particle had a layered structure with sharp and intense lines at low 2θ and less intense lines at high 2θ. The peaks observed at 2θ = 11.673, 23.469, 34.437, 35.978, 38.428, 41.652, 45.520, 60.675 and 62.025 (JCPDS 87-1138) were corresponded well to quintinite particles found in the literature (Delorme *et al*., 2007). The particle had a chemical formula of $Mg_4Al_2(OH)_{12}CO_3 \cdot 3H_2O$ with hexagonal crystal system (a = 5.283 Å; c = 15.159 Å). Based on the XRD pattern, the average crystal size (*d*) of the particle was estimated by the Debye-Scherrer formula (Yu *et al*., 2009):

$$d = \frac{0.9\lambda}{\beta \cos\theta}$$

(1)

where λ is the wavelength of the X-ray (= 1.5406 Å), β is full width at half maximum width of diffraction peak (= 0.369 °), and θ is the diffraction angle (= 11.673 °/2). From the Debye-Scherrer analysis (inset in Figure 7.3(a)), the value of d was calculated to be 21.6 nm. N_2 adsorption and desorption isotherms are presented in Figure 7.3(b). According to the BET analysis (inset in Figure 7.3(b)), the particles had the specific surface area of 49.8 m^2/g and total pore volume of 0.4582 cm^3/g. From the BJH analysis, the mesopore volume was determined to be 0.4522 cm^3/g.
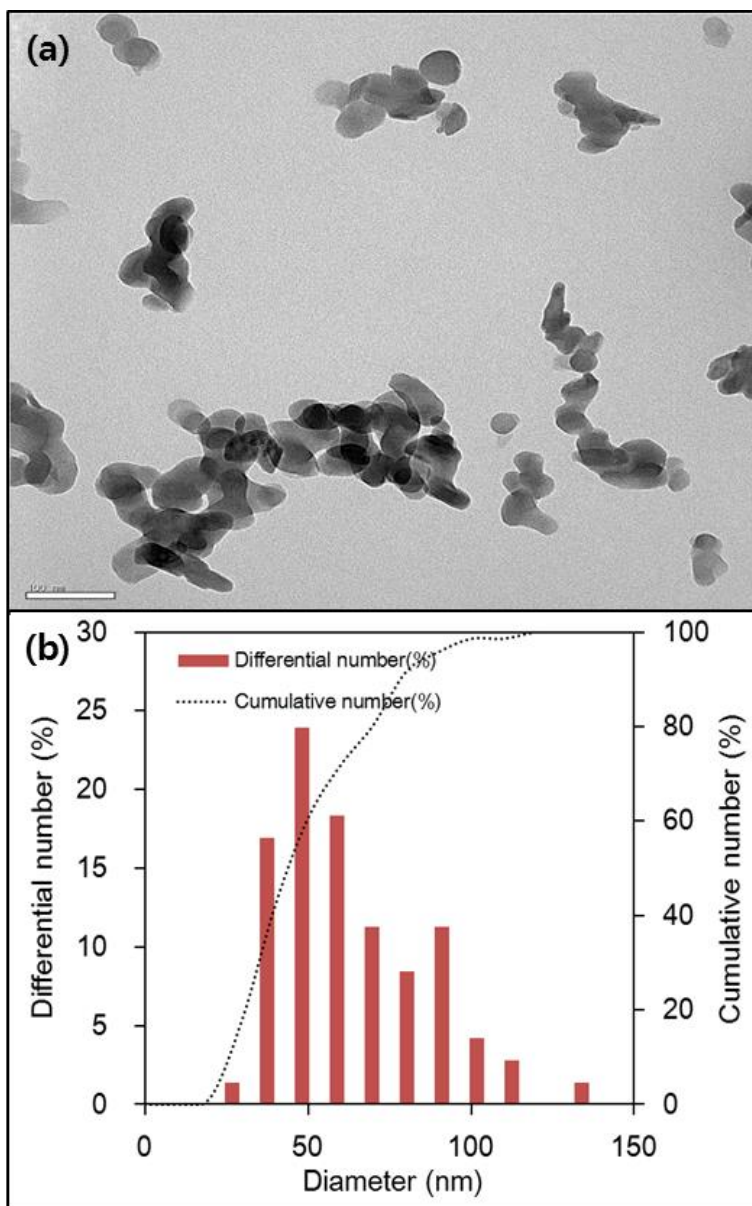
Figure 7.1 Characteristics of quintinite particles: (a) transmission electron microscopy (TEM) image (bar = 100 nm); (b) particle size analysis based on the TEM image (number of particle = 71).
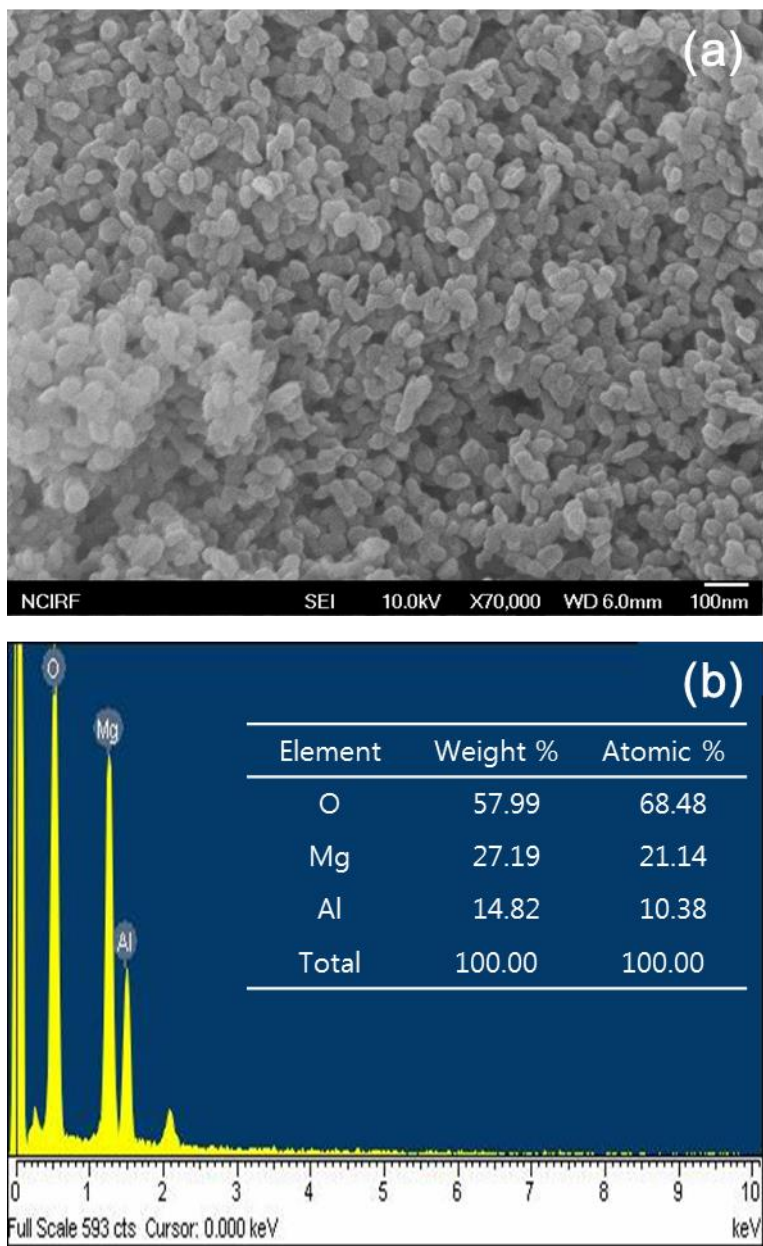
Figure 7.2 Characteristics of quintinite: (a) FESEM image (bar = 100 nm); (b) EDS pattern (inset = element composition).
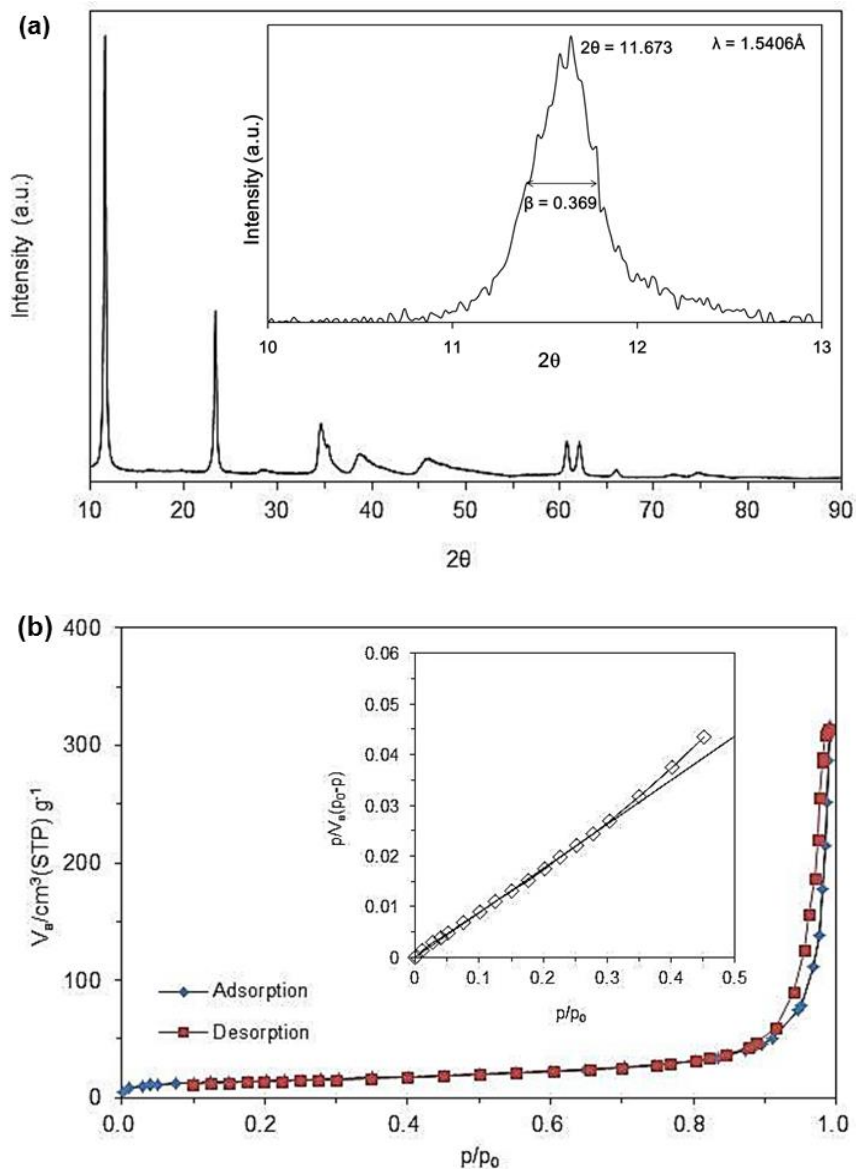
Figure 7.3 Characteristics of quintinite particles: (a) X-ray diffraction (XRD) pattern of quintinite particles (inset = Debye-Scherrer analysis); (b) N_2 adsorption-desorption isotherms (inset = BET analysis).

Table 7.4 Physical characteristics of quintinite obtained from the N_2 adsorption–desorption data.

Characteristics	Value	Unit
Brunauer–Emmett–Teller (BET) analysis		
Monolayer volume (V_m)	11.4	cm^3/g
BET specific surface area ($a_{s,BET}$)	49.8	m^2/g
BET constant	918.9	-
Total pore volume (V_p)	0.458	cm^3/g
Average pore diameter ($d_{p,ave}$)	36.8	nm
Barrett–Joyner–Halenda analysis		
Mesopore volume ($V_{p,me}$)	0.452	cm^3/g
Peak diameter of mesopore ($d_{p,me}$)	163.2	nm
Horvath–Kawazoe analysis		
Micropore volume ($V_{p,mi}$)	2.9	cm^3/g
Peak diameter of micropore ($d_{p,mi}$)	0.9	nm

7.2.2. Batch adsorption of phosphate

The phosphate removal by the quintinite as a function of adsorbent dose (initial P concentration = 2 mgP/g; adsorbent dose = 0.2 – 2.0 g/L; reaction time = 24 h) is provided in Figure 7.4. The percent removal was 34.3% at the dose of 0.2 g/L and 100% at a dose of 2.0 g/L. The sorption capacity decreased with increasing adsorbent dose from 0.2 to 2.0 g/L. The sorption capacity was 3.26 mgP/g at 0.2 g/L, and decreased to 1.57 mgP/g at 1.2 g/L. The sorption capacity decreased to 1.27 mgP/g at 1.5 g/L, decreasing further to 0.95 mgP/g at 2.0 g/L.

The phosphate removal by the quintinite as a function of reaction time is provided in Figure 7.5. At 30 °C, the phosphate concentration decreased rapidly with increasing reaction time until equilibrium was reached. The phosphate concentration dropped to 0.124 mgP/L at 5 min of reaction time and further decreased to 0.057 mgP/L at 1 h. The phosphate sorption reached equilibrium at 4 h of reaction time with a phosphate concentration of < 0.05 mgP/L. The sorption capacity changed from 1.44 to 1.51 mgP/g with reaction time changing from 5 min to 4 h.

The phosphate removal by the quintinite at different temperature is also presented in Figure 7.5, demonstrating that the phosphate sorption to the quintinite increased with increasing temperature from 15 to 45 °C. It indicates that the sorption process was endothermic.

The phosphate removal by quintinite particles as a function of initial phosphate concentration is provided in Figure 7.6. The percent removal decreased with an increasing initial phosphate concentration from 2 to 20 mgP/L. At the lowest concentration of 2 mgP/L, the percent removal was 98.4%.
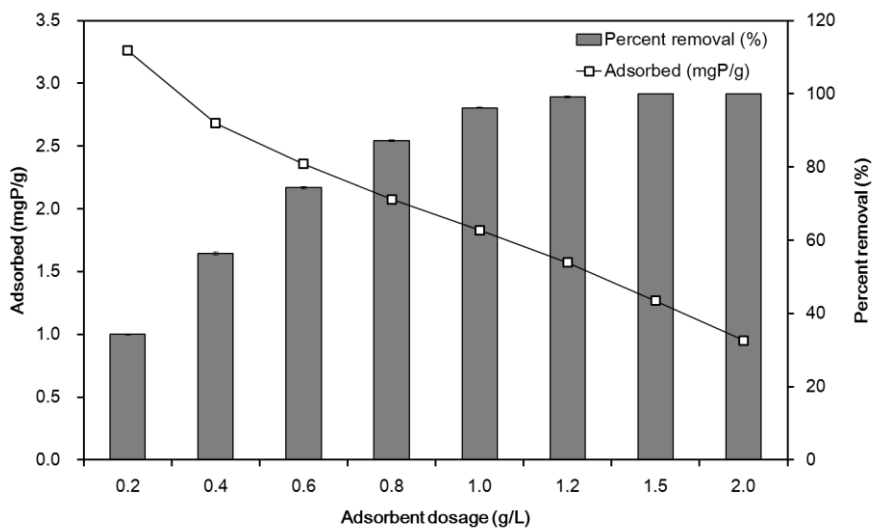
Figure 7.4 Effect of quintinite dose on removal of phosphate (initial concentration = 2 mgP/L; reaction time = 4 h).
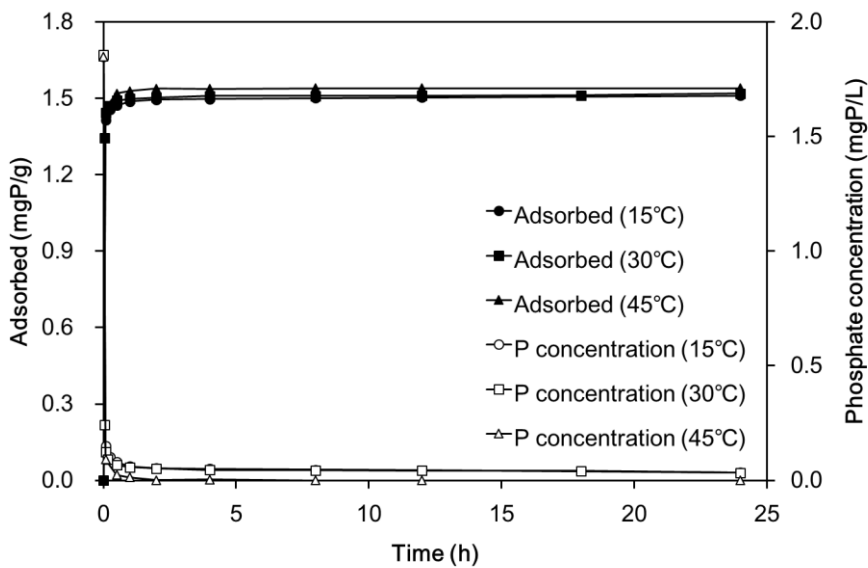
Figure 7.5 Effect of reaction temperature on phosphate removal by quintinite (adsorbent dose = 1.2 g/L; initial concentration = 2 mgP/L).
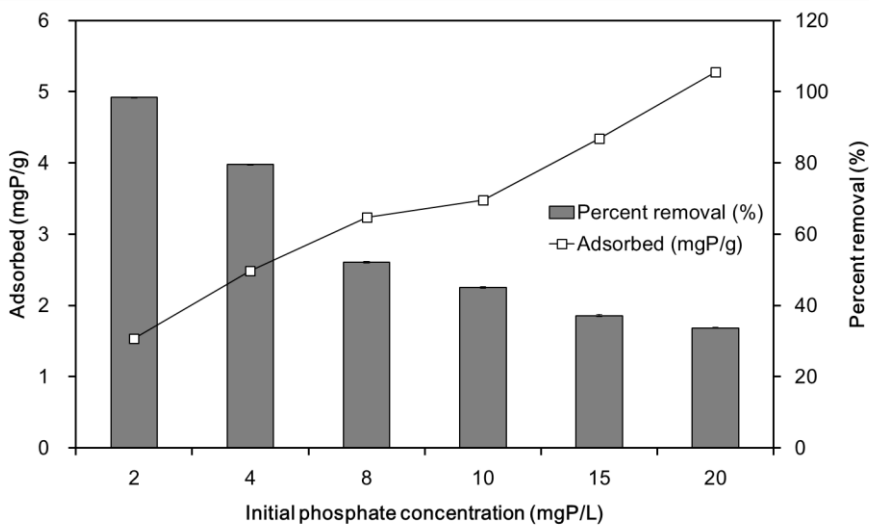
Figure 7.6 Phosphate removal by quintinite as a function of initial concentration (reaction time = 4 h).

The percent removal decreased to 45.0% at the phosphate concentration of 10 mgP/L and further decreased to 33.7% at the highest concentration of 20 mgP/L. The sorption capacity increased from 1.54 to 5.28 mgP/g with increasing phosphate concentrations from 2 to 20 mgP/L.

The effect of initial solution pH on phosphate removal by the quintinite is shown in Figure 7.7. The sorption capacity was 1.55 mgP/g at pH 3.0. The sorption capacity remained relatively constant at 1.50 – 1.55 mgP/g between pH 3.0 and 7.1. At pH 9.1, the sorption capacity decreased to 1.36 mgP/g. As the pH approached 11.0, the sorption capacity decreased sharply to 0.70 mgP/g. The results indicate that phosphate removal was not much varied at initial pH 3 – 7. This result could be related to the fact that the final (equilibrium) pH converged to 7.2 – 7.8 during the sorption experiments (initial pH 3.0 – 7.1).

Similar findings were reported in the literature by Han *et al*. (2011) reporting that the removal of phosphate in the alginate beads containing calcined Mg/Al LDH was not sensitive to solution pH. They demonstrate that the percent removal of phosphate decreased slightly from 98.6% to 95.5% as solution pH increased from 4.9 to 8.9. In our experiments, phosphate removal decreased sharply as the solution pH approached a highly alkaline condition (pH 11.0). This could be due to the competition between phosphate ions and hydroxyl ions (OH^-) to the sorption sites.

The phosphate removal in synthetic solution and stream water are compared in Figure 7.8. The sorption capacity in the synthetic solution was 2.07 mgP/g with the percent removal of 87.2%, whereas the sorption capacity in the stream water was 1.88 mgP/g with the percent removal of

79.9%.

The results indicate that phosphate removal in the stream water was lower than that in the synthetic solution. This result could possibly be due to the presence of anions such as (bi)carbonate (HCO_3^{2-}) and sulfate (SO_4^{2-}) in the stream water. Especially, (bi)carbonate could greatly interfere with the phosphate removal from the stream water (Lee *et al*., 2012). It is known that two mechanisms including interlayer anion exchange and surface adsorption could contribute to the removal of phosphate by quintinite (Goh *et al*., 2008). In anion exchange process, the charge balancing anions (carbonate) in the interlayer region is replaced by phosphate ions. In surface adsorption, the negatively charged phosphate ions could adsorb to the positively charged brucite-like layer through electrostatic interaction (Goh *et al*., 2008).
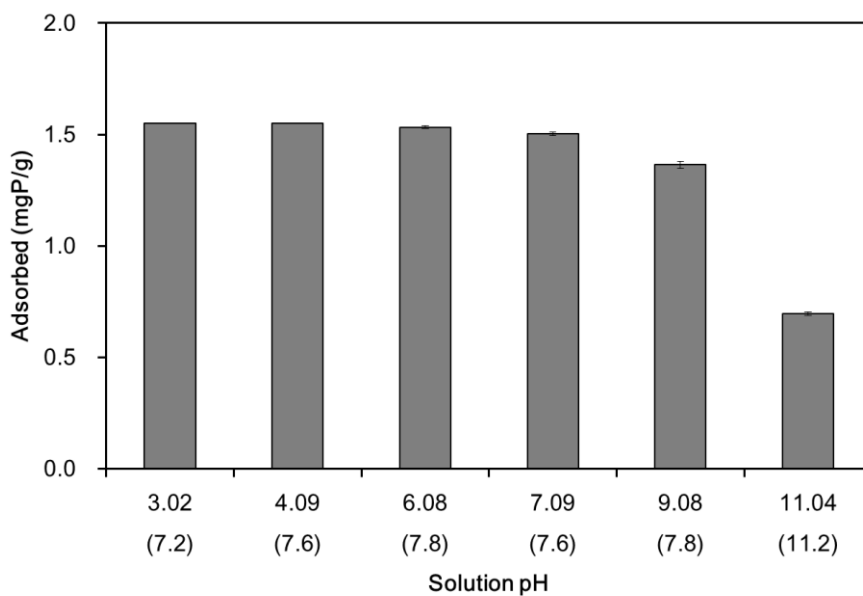
Figure 7.7 Effect of initial solution pH on phosphate removal by quintinite (the numbers in the parenthesis of X-axis = final (equilibrium) pHs).
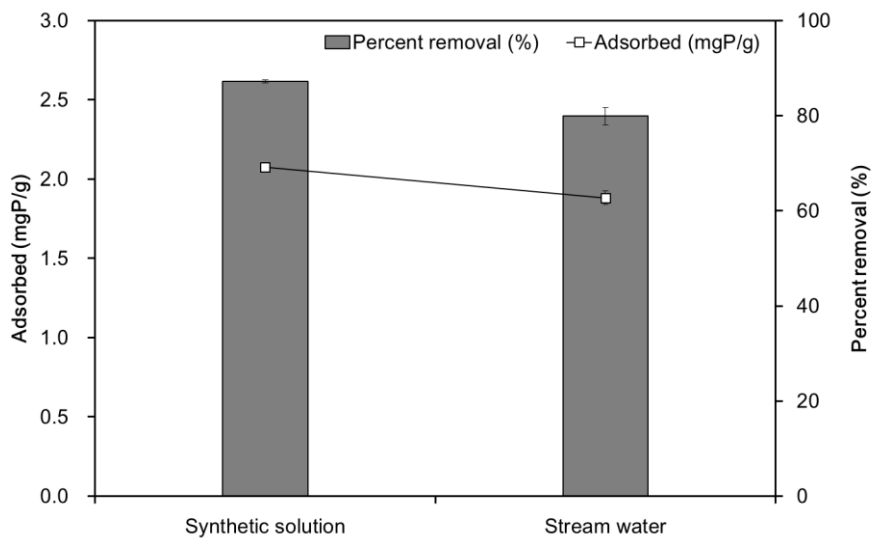
Figure 7.8 Comparison between synthetic solution and stream water
(initial P concentration = 2 mgP/L).

7.2.3. Kinetic, isotherm and thermodynamic model analyses

The kinetic model fits and the related model parameters are provided in Figure 7.9 and Table 7.5, respectively. The values of R^2 indicate that the pseudo second-order model (Figure 7.9(b)) was the best model to describe the kinetic data, and chemisorption is involved in the adsorption of phosphate to the quintinite. In addition, the values of q_e in the pseudo second-order model increased with increasing temperature (Table 7.5), showing that the phosphate adsorption capacity of the quintinite increased as temperature increased. The values of k_2 also increased with increasing temperature, demonstrating that the time for equilibrium decreased as temperature increased.

The phosphate removal by the quintinite at different temperature is also presented in Figure 7.9, demonstrating that the phosphate sorption to the quintinite increased with increasing temperature from 15 to 45 °C. It indicates that the sorption process was endothermic. The thermodynamic parameters are presented in Table 7.6. The value of $\Delta H°$ was determined to be 487.08 kJ/mol, demonstrating that the phosphate sorption to the quintinite had the endothermic nature. The value of $\Delta S°$ was calculated to be 1696.12 J/K/mol, indicating that the randomness increased at the interface between solid and solution during the sorption process. The values of $\Delta G°$ were in the range from -1.67 to -52.56 kJ/mol, showing that the phosphate sorption to the quintinite was spontaneous.

These results agree with the report of Halajnia *et al*. (2013) who examined the endothermic nature of phosphate sorption to Mg/Al LDH. Cheng *et al*. (2009) also reported that phosphate adsorption to calcined

Zn/Al LDH increased with increasing temperatures from 25 to 50 °C. However, Das *et al*., (2006) reported that phosphate adsorption to calcined Mg/Al LDH decreased with increasing temperatures from 30 to 60 °C, showing that the sorption process was exothermic.

The equilibrium isotherm model fits and the related parameters are presented in Figure 7.11 and Table 7.7, respectively. The values of R^2, χ^2 and *SAE* indicate that both the Freundlich and Redlich-Peterson isotherms were more suitable than the Langmuir isotherm at describing the equilibrium data. Note that the Redlich-Peterson model fit was superimposed on the Freundlich fit in Figure 7.11. It is known that when a_R and K_R are much greater than unity, the Redlich-Peterson model can be reduced to the Freundlich model (Zhang *et al*., 2011). In Table 7.7, the value of K_F from the Freundlich isotherm (= 2.63 L/g) was equivalent to the value of K_R/a_R from the Redlich-Peterson model, whereas the value of $1/n$ (= 0.24) was corresponded to the value of (1 - g). The maximum phosphate adsorption capacity (Q_m) was calculated to be 4.77 mgP/g from the Langmuir model, which was lower than the removal capacity for LDHs (7.3 – 81.6 mgP/g) reported in the literature (Goh *et al*., 2008). However, it should be noted that experiments were performed at the low initial phosphate concentration range (2 – 20 mgP/L).
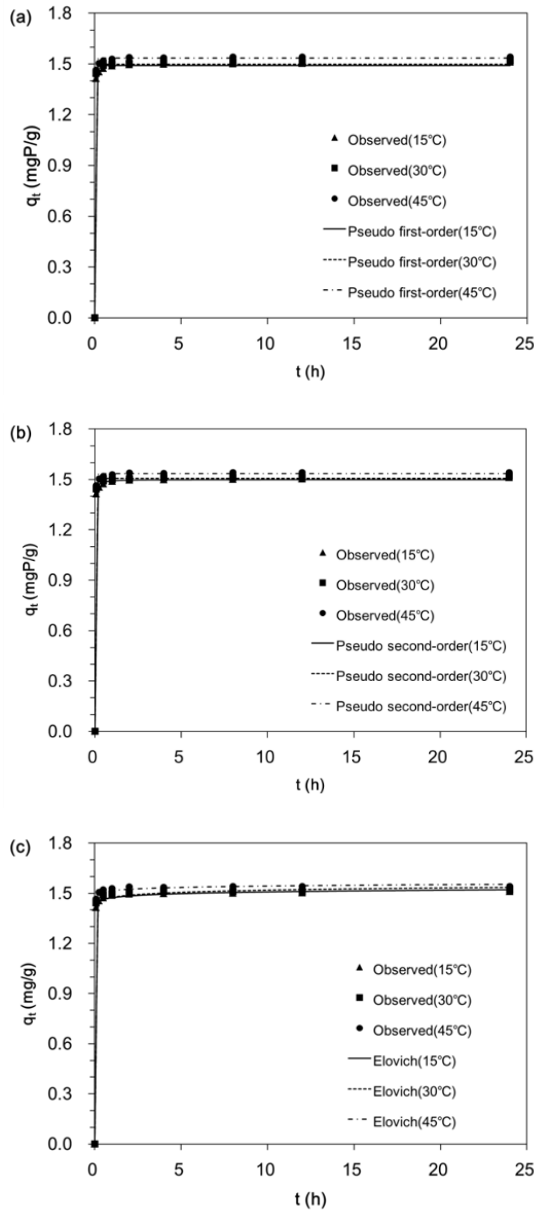
Figure 7.9 Kinetic model fits for phosphate sorption to quintinite: (a) pseudo first-order model; (b) pseudo second-order model; (c) Elovich model.

Table 7.5 Kinetic model parameters obtained from model fitting to phosphate sorption experimental data.

Temp. (°C)	Pseudo first-order model				
	q_e (mgP/g)	k_1 (1/h)	R^2	χ^2	SAE
15	1.49	35.58	0.999	1.59E-03	0.112
30	1.50	37.00	0.833	2.52E-01	0.120
45	1.54	67.46	1.000	2.35E-04	0.072

Temp. (°C)	Pseudo second-order model				
	q_e (mgP/g)	k_2 (g/mgP/h)	R^2	χ^2	SAE
15	1.50	122.28	1.000	3.39E-04	0.053
30	1.51	151.33	0.993	1.18E-01	0.031
45	1.54	161.15	1.000	4.38E-05	0.027

Temp. (°C)	Elovich model				
	α (mgP/g/h)	β (g/mgP)	R^2	χ^2	SAE
15	3.55E+05	66.23	0.854	7.57E-04	0.085
30	2.30E+06	53.19	0.694	1.72E-01	0.121
45	2.53E+06	84.03	0.735	8.23E-04	0.091
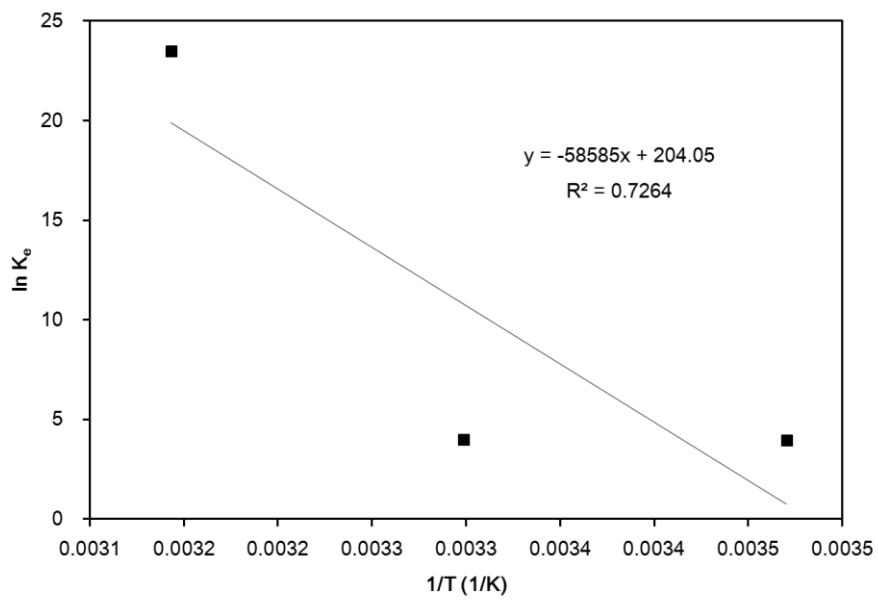
Figure 7.10 Thermodynamic analysis for phosphate sorption to quintinite.

Table 7.6 Thermodynamic parameters for phosphate sorption to quintinite.

Temp. (°C)	ΔH° (kJ/mol)	ΔS° (J/K/mol)	ΔG° (kJ/mol)
15	487.08	1696.12	-1.67
30			-27.11
45			-52.56
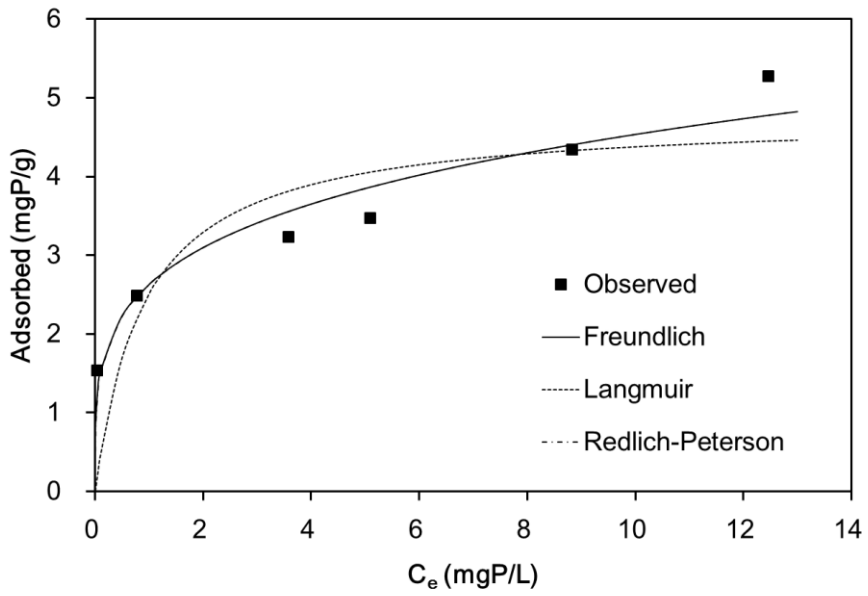
Figure 7.11 Equilibrium isotherm model fits for phosphate sorption to quintinite.

Table 7.7 Equilibrium isotherm model parameters obtained from model fitting to phosphate sorption experimental data.

Freundlich model				
K_F (L/g)	1/n	R^2	χ^2	SAE
2.630	0.237	0.924	0.194	1.676

Langmuir model				
Q_m (mgP/g)	K_L (L/mgP)	R^2	χ^2	SAE
4.773	1.117	0.617	0.228	3.669

Redlich-Peterson model					
K_R (L/g)	a_R (L/mgP)	g	R^2	χ^2	SAE
6.30E+06	2.40E+06	0.763	0.924	0.195	1.674

7.2.4. Batch adsorption of fluoride

The effect of adsorbent dose on fluoride removal is shown in Figure 7.12. The percent removal increased from 41.7±0.3 to 89.8±0.2% with increasing adsorbent doses from 0.1 to 2.0 g in 30 mL of solution. Meanwhile, the sorption capacity decreased from 1.26±0.01 to 0.14± 0.01 mgF/g with increasing adsorbent doses. Results indicate that initial fluoride concentration of 10 mgF/L could be reduced to < 1.5 mgF/L at the adsorbent dose $\geq$ 1.5 g.

The effect of reaction time on the removal of fluoride is provided in Figure 7.13. The fluoride concentrations decreased rapidly with increasing reaction time until the equilibrium was reached at 6 h. At 1 h of reaction time, the fluoride concentration dropped sharply to 2.7 mgF/L (initial fluoride concentration =10 mgF/L), and further decreased to 1.4 mgF/L at 6 h. Then, the fluoride concentration reached to 1.2 mgF/L at 24 h of reaction time. Meanwhile, the sorption capacity increased from 0.15 to 0.18 mgF/g with increasing reaction time from 1 to 24 h.

The effect of initial fluoride concentration on fluoride removal is presented in Figure 7.14. At the lowest concentration of 10 mgF/L, the percent removal was 87.6% and then decreased to 68.0% at the fluoride concentration of 100 mgF/L. The percent removal further decreased to 27.8% at the highest concentration of 1,000 mgF/L. Meanwhile, the sorption capacity increased from 0.18 to 5.75 mgF/g with increasing fluoride concentrations from 10 to 1,000 mgF/L.
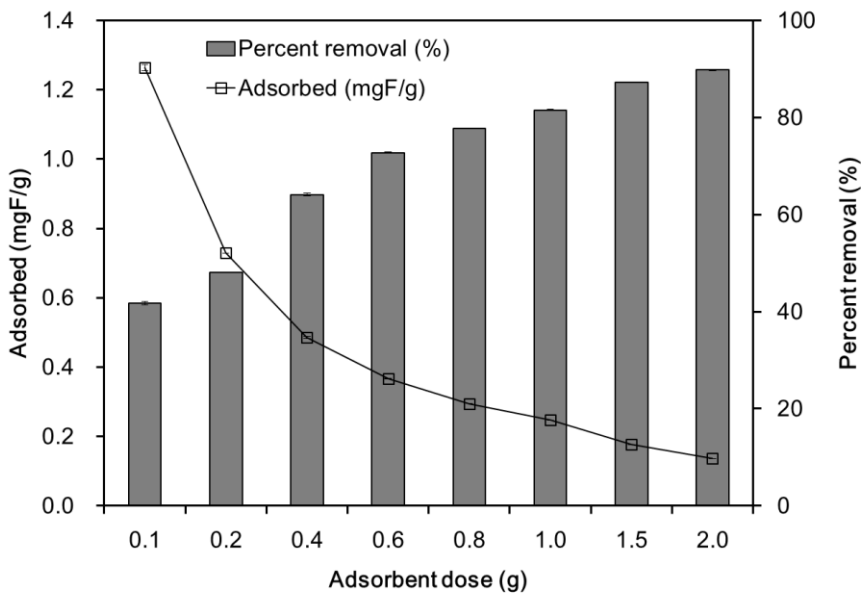
Figure 7.12 Effect of quintinite dose on removal of fluoride (initial concentration = 10 mgF/L; reaction time = 6 h).
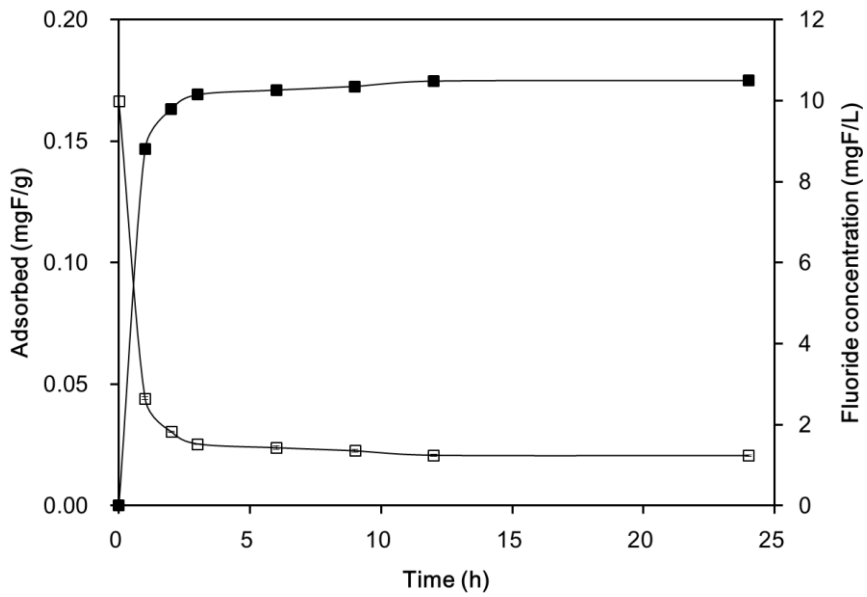
Figure 7.13 Effect of reaction time on fluoride removal by
quintinite(adsorbent dose = 50 g/L; initial concentration = 10 mgF/L).
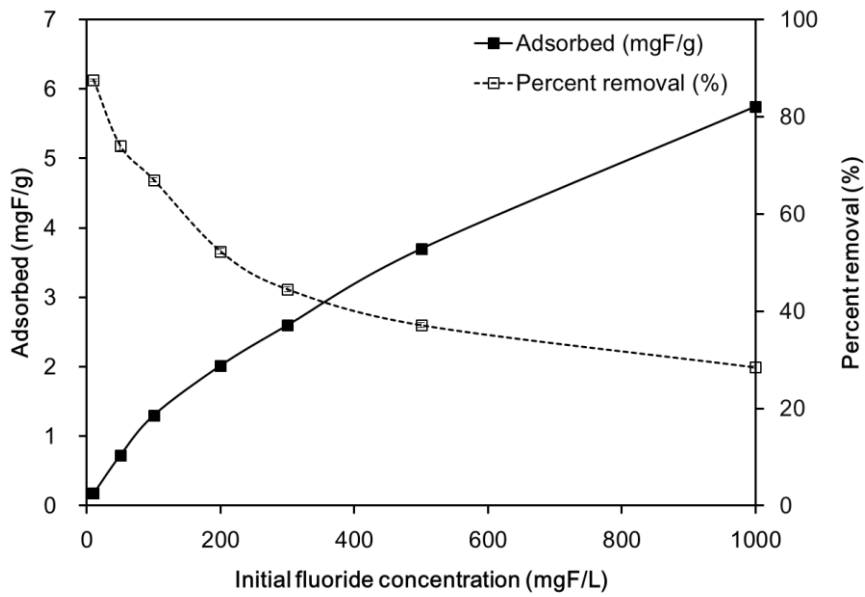
Figure 7.14 Fluoride removal by quintinite as a function of initial
concentration (reaction time = 6 h).

The effect of initial solution pH on fluoride removal is demonstrated in Figure 7.15. The sorption capacity at pH 3 was 0.10 mgF/g and increased to 0.17 mgF/g at pH 5. Between pH 5 and pH 9, the sorption capacity remained relatively constant at $0.17 - 0.18$ mgF/g. At pH 10, the sorption capacity dropped to 0.16 mgF/g and then further decreased sharply to 0.09 mgF/g.

Results demonstrate that fluoride sorption in quintinite particles was not much varied at initial pH $4 - 10$. This result could be related to the fact that the final (equilibrium) pH converged to $8.1 - 8.8$ during the sorption experiments (initial pH $4 - 10$). Similar findings were reported in the literature by Kim *et al*. (2013) showing that the fluoride sorption capacity of calcined Mg/Al LDH was not greatly varied between pH 4 and pH 9; the sorption capacity changed from 15.6 to 14.1 mgP/g with increasing pH from 4 to 9. Han *et al*. (2011) also reported that the removal of phosphate in the alginate beads containing calcined Mg/Al LDH was not sensitive to solution pH. They demonstrate that the percent removal of phosphate decreased slightly from 98.6% to 95.5% as solution pH increased from 4.9 to 8.9.

In this study, the fluoride sorption capacity decreased considerably at highly acidic (pH < 3) and alkaline pH (pH > 11) conditions. At highly acidic pH, the fluoride sorption could decrease due to the formation of HF (hydrofluoric acid), which is not favorable for adsorption to the surfaces of adsorbent. According to MINTEQ calculation (Visual MINTEQ 3.0), HF species is formed at 35% of total F species (HF and F^-) at pH 3. In addition, metal cations in quintinite might be dissolved at highly acidic pH, which results in the decrease of fluoride sorption (Lv

226

et al., 2007). At highly alkaline pH, the fluoride sorption could decrease due to the competition between F^- and OH^- on the sorption sites. The contribution of NaF formation to the decrease of fluoride sorption might be negligible at highly alkaline pH. According to MINTEQ calculation, NaF species is only 0.2% of total F species (F^- and NaF) at pH 11. Note that alkaline pH was obtained by adding 0.1 M NaOH in the experiments. Lv *et al*. (2007) reported that phosphate removal in Mg/Al HTL decreased sharply from 110 to 5 mg/g with increasing pH from 5 to 10. Mandal and Mayadevi (2008) showed that phosphate removal in Zn/Al LDH had an increasing tendency between 2.5 and 6.2 but a decreasing one between 6.2 and 9.8.

X-ray photoelectron spectroscopy (XPS) spectra were presented in Figure 7.16. In the wide scan before and after fluoride sorption experiments (Figure 7.16(a)), the peaks at binding energy of 49.15 and 73.20 eV are assigned to Mg 2p and Al 2p, respectively. In the high-resolution scan of the F 1s region after fluoride sorption experiment (Figure 7.16(b)), the peak at 683.4 eV is ascribed to adsorbed fluoride ion on the surfaces of quintinite (Zhou *et al*., 2011). It is known that two mechanisms including interlayer anion exchange and surface adsorption could contribute to the removal of fluoride by quintinite particles (Goh *et al*., 2008). In anion exchange process, the charge balancing anion (carbonate) in the interlayer region is replaced by fluoride ion. In surface adsorption, the negatively charged fluoride could adsorb to the positively charged brucite-like layer via electrostatic interaction (Goh *et al*., 2008).
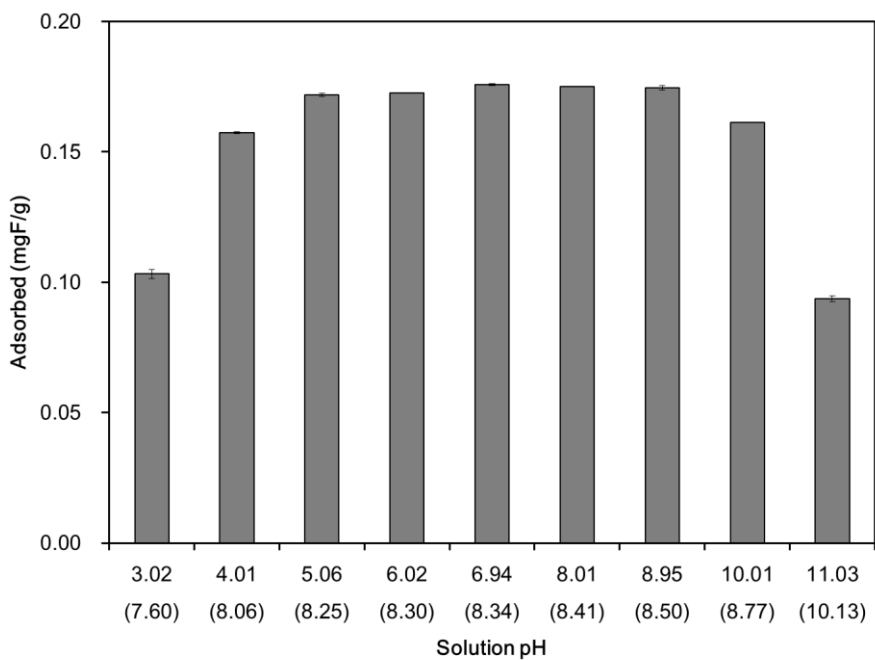
Figure 7.15 Effect of initial solution pH on fluoride removal by quintinite (the numbers in the parenthesis of X-axis = final (equilibrium) pHs).
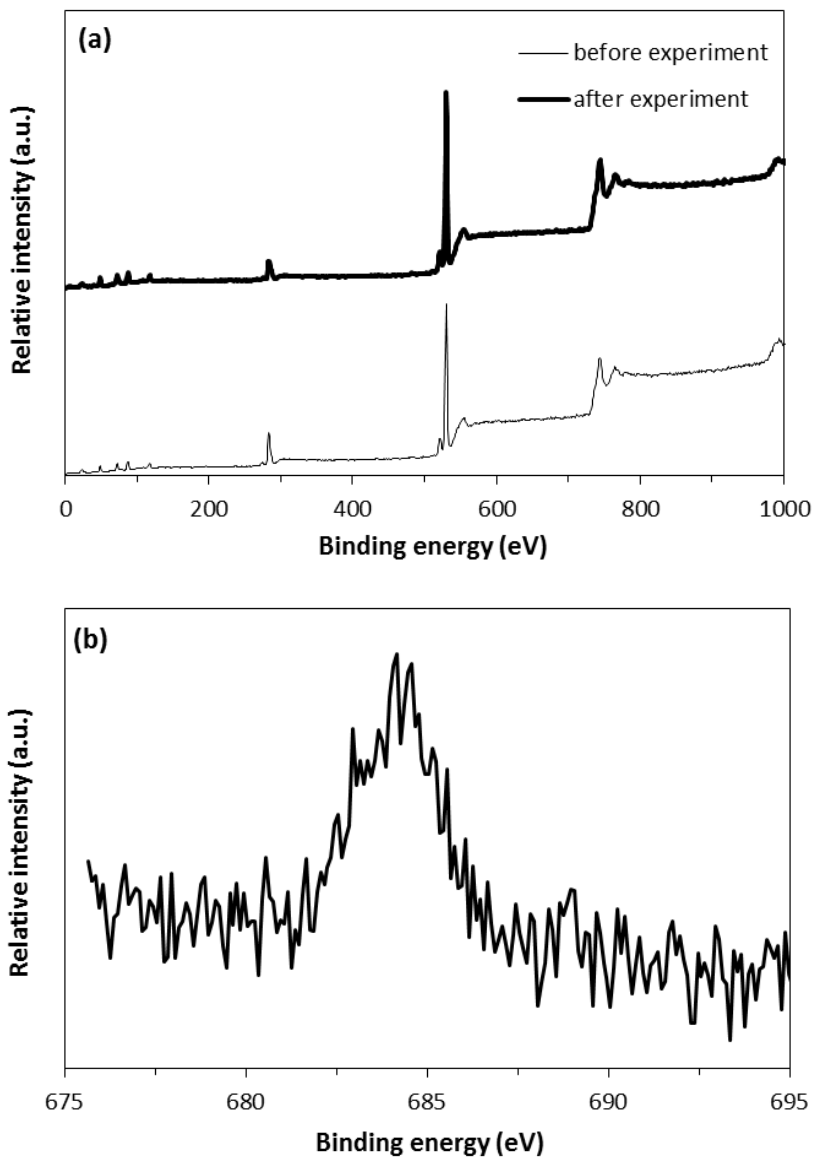
Figure 7.16 X-ray photoelectron spectroscopy (XPS) spectra: (a) wide scan before and after fluoride sorption experiments; (b) high-resolution scan of the F 1s region after fluoride sorption experiment.

7.2.5. Kinetic, isotherm and thermodynamic model analyses

The kinetic data and model fits for fluoride sorption to quintinite are shown in Figure 7.17. Model parameters for the pseudo first-order, pseudo second-order, and Elovich models are provided in Table 7.8. In the pseudo first-order model, the value of q_e was 0.17 mgF/g, and the value of k_1 was 1.85 h^{-1}. The value of q_e from the pseudo second-order model was similar to that from the pseudo first-order model. The value of q_e was 0.18 mgF/g, and the value of k_2 was 28.80 g/mgF/h, respectively. In the Elovich model, the values of α and β were 1.90E+06 mgF/g/h and 125.0 g/mgF, respectively. The values of R^2, χ^2, and SAE indicate that the pseudo second-order model was the most suitable for describing the data.

This finding indicates that chemisorption is involved in the adsorption of fluoride to quintinite. In the literature, Cai *et al*. (2012) reported that the kinetic data for fluoride sorption to calcined Mg/Al LDH were found to fit very well the pseudo second-order model. Zhou *et al*. (2011) also reported that the pseudo-second-order model was suitable for describing the adsorption kinetics of fluoride on calcined Li/Al LDH.
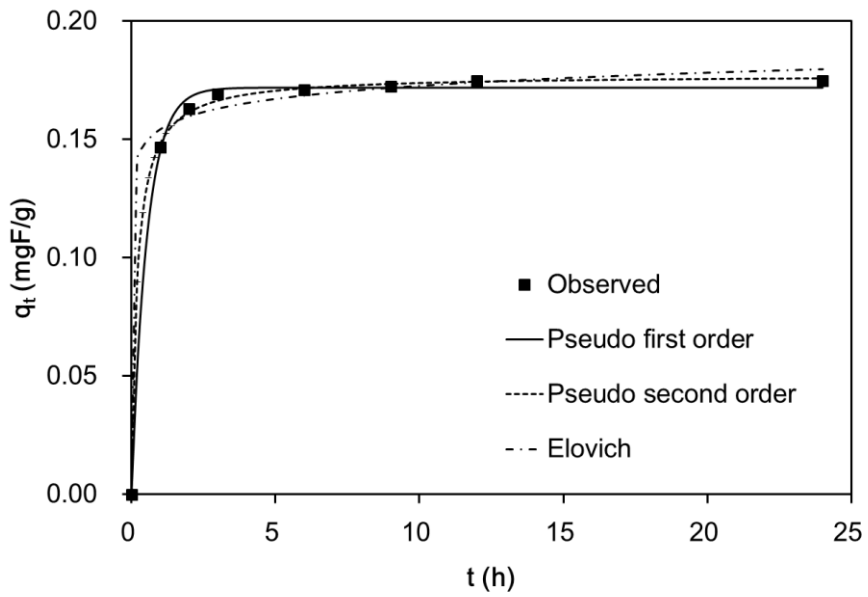
Figure 7.17 Kinetic model fits for fluoride removal to quintinite.

Table 7.8 Kinetic model parameters obtained from model fitting to fluoride removal experimental data.

Pseudo first-order model				
q_e (mgF/g)	k_1 (1/h)	R^2	χ^2	SAE
0.172	1.853	0.923	2.75E-04	0.016

Pseudo second-order model				
q_e (mgF/g)	k_2 (g/mgF/h)	R^2	χ^2	SAE
0.177	28.800	0.975	9.19E-05	0.009

Elovich model				
α (mgF/g/h)	β (g/mgF)	R^2	χ^2	SAE
1.90E+06	125.000	0.775	8.39E-04	0.025

The equilibrium data and isotherm model fits for fluoride sorption to quintinite are shown in Figure 7.18. The equilibrium isotherm parameters for the Langmuir, Freundlich, and Redlich-Peterson models are summarized in Table 7.9. The values of R^2, χ^2, and SAE indicate that both Freundlich and Redlich-Peterson models were suitable for describing the data. Note that the Redlich–Peterson model fit was superimposed on the Freundlich fit (Figure 7.18). The Redlich–Peterson model can be reduced to the Freundlich model if K_R and a_R are much greater than unity (Zhang *et al*., 2011). In the Freundlich model, the value of K_F was 0.20 L/g, which corresponded well to the value of K_R/a_R in the Redlich–Peterson model. The value of $1/n$ was equivalent to the value (0.51) of $(1 - g)$.

The fluoride sorption capacities of hydrotalcite-like particles or mixed metal oxides from in the literature are summarized in Table 7.10. The maximum adsorption capacity (Q_m) of quintinite in this study was determined to be 7.71 mgF/g from the Langmuir model, which was in the low range of adsorption capacity in Table 7.10. In order to improve the fluoride sorption capacity of quintinite, thermal treatment of quintinite at high temperatures ($\geq$ 300 ^{o}C) is recommended, which results in the increase of the BET surface area and fluoride sorption capacity (Kim *et al*., 2013). Consequently, it is expected that the cost effectiveness of the adsorbent in fluoride removal can be improved.
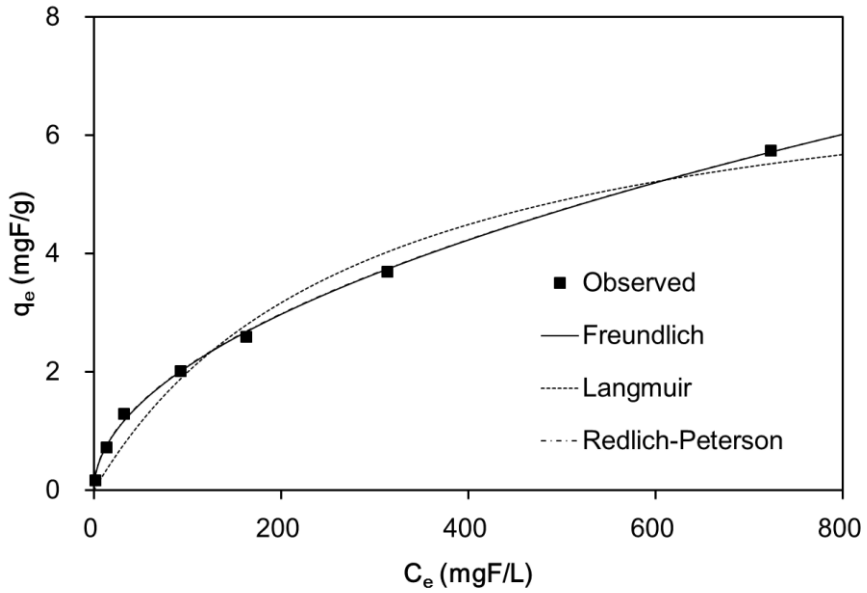
Figure 7.18 Equilibrium isotherm model fits for fluoride removal to quintinite: (a) Freundlich model; (b) Langmuir model; (c) Redlich-Peterson model.

Table 7.9 Equilibrium isotherm model parameters obtained from model fitting to phosphate sorption experimental data.

Freundlich model				
K_F (L/g)	$1/n$	R^2	χ^2	SAE
0.202	0.508	0.999	0.028	0.344

Langmuir model				
Q_m (mgF/g)	K_L (L/mgF)	R^2	χ^2	SAE
7.714	0.004	0.970	0.670	1.950

Redlich-Peterson model					
K_R (L/g)	a_R (L/mgF)	g	R^2	χ^2	SAE
3.643	17.724	0.495	0.999	0.026	0.340

Table 7.10 Maximum adsorption capacity of fluoride in hydrotalcite-like (HTL) or mixed metal oxide (MMO) particles reported in the literature (from the Langmuir isotherm analysis).

Adsorbent	Initial F concentration (mgF/L)	Adsorption capacity (mgF/g)	References
Quintinite	10 – 1000	7.71	This study
Mg/Al MMO	5 – 50	36.9	Cai *et al*., 2012
Li/Al MMO	50 – 500	128.2 – 158.7	Zhou *et al*., 2011
Mg/Al HTL	10 – 1000	416.7	Batistella *et al*., 2011
Mg/Al/Fe MMO	3 – 60	14.9	Ma *et al*., 2011
Zn/Al HTL	5.6 – 51.4	4.1	Mandal *et al*., 2009
Mg/Al MMO	3.5 – 500	213.2	Lv *et al*., 2007
Mg/Al HTL	5 – 2500	319.8[*]	Lv *et al*., 2007
Zn/Al MMO	2 – 60	13.4	Das *et al*., 2003

[*] Maximum adsorption capacity obtained from the Langmuir-Freundlich isotherm

7.2.6. Conclusions

In this chapter, the sorption of phosphate and fluoride to quintinte were examined using batch experiments.

The maximum adsorption capacity of phosphate to quintinite was 4.77 mgP/g. Kinetic model analysis showed that the pseudo second-order model was the most suitable for describing the kinetic data. Thermodynamic analysis indicated the spontaneous and endothermic nature of sorption process. Equilibrium isotherm model analysis demonstrated that both Freundlich and Redlich-Peterson models were suitable for describing the equilibrium data. In the pH experiments, the phosphate adsorption to quintinite was not varied at pH 3.0 – 7.1 but decreased considerably at the highly alkaline solution (pH 11.0). Results also indicated that phosphate removal in the stream water was lower than that in the synthetic solution, possibly due to the presence of anions in the stream water.

Results of fluoride removal experiments demonstrated that the maximum adsorption capacity of fluoride to quintinite was 7.71 mgF/g. The adsorption of fluoride to quintinite was not changed at pH 5 – 9 but decreased considerably at the highly acidic (pH < 3) and alkaline (pH > 11) solution conditions. Kinetic model analyses showed that the pseudo second-order model was the most suitable for describing the kinetic data, whereas both Freundlich and Redlich-Peterson models were suitable for describing the equilibrium data.

This study showed that quintinite could be applied as adsorbents for both phosphate and fluoride removal from aqueous solution.

Chapter 8 General Conclusions and Recommendations

8.1 General conclusions

This thesis was performed with four types of adsorbents in batch reactor, fixed bed, and pilot-scale adsorption tower. Iron oxide nanoparticle-chitosan composite, triamine-functionalized mesoporous silica-polymer composite, MgFe calcined LDH-PVAD/PVA composite, and quintinite were synthesized and applied as adsorbents for removal of phosphorous, chromium, and fluorine removal from water. The synthesized adsorbents were characterized by analytical techniques such as FESEM, TEM, nitrogen sorption, FTIR, EDS, and XPS. Batch experiments were performed at different adsorbent dose, reaction time, initial concentration, solution pH, and temperature. Column experiments were performed at different flow rate, initial concentration, bed depth. Adsorption tower experiment was performed at Seoho pilot plant located in Suwon, Korea for 33 days. Data were analyzed by kinetic adsorption model, kinetic diffusion model, isotherm model, and thermodynamic analysis.

1. In chapter 3, iron oxide nanoparticle-chitosan composites were prepared by entrapping powdered forms of iron oxide nanoparticles(ION) in chitosan hydrogel. The ION-chitosan composites could be easily synthesized and exhibited efficient adsorption capacity of phosphate. They were stable under natural environmental conditions. T-P concentration of effluent in adsorption tower experiment remained under 0.035 mg/L which can cause eutrophication for 33 days. Although

adsorbents in the adsorption tower had not been reached its full saturation, pilot-scale experiment was finished due to high pressure of adsorption tower. It is necessary to perform additional pilot-scale experiments including long-term sorption experiment and reuse of ION-chitosan composites. The results demonstrated that solution pH did not change significantly after adsorption. ION-chitosan composites could be considered as efficient and eco-friendly candidate for phosphate adsorbent.

2.   In chapter 4, The DAEAPTS-grafted SBA-15 was prepared via wet grafting technique. XPS analysis revealed that chromate reduced on the surface of the triamine functionalized mesoporous silica, accompanied with transformation of chromium. Mesoporous silicas have considerable differences in the structure such as framework structure, chemical properties of the wall surface. Further studies are needed for elucidating the origin of the differences between the framework structures appearing at the Cr(VI) adsorption. The effects of the silane coupling agents have more amino groups and chains of different length scales are also needed to study.

3.   In chapter 5, calcined Mg-Fe layered double hydroxide (LDH) was prepared by a co-precipitation method and calcination at 300 ℃. The phosphate removal by the calcined Mg-Fe LDH did not vary much at initial pH values of 3.0 – 9.1, but it decreased sharply at pH 11.0. The results demonstrated that the calcined Mg-Fe LDH could be used repeatedly as adsorbents

for phosphate removal through adsorption-desorption procedures.

4. In chapter 6, The maximum adsorption capacity of MgFe CLDH-PVDF/PVA composites was 33.06 mgP/g under the given experimental conditions (adsorbent dose = 0.1 g/L; initial P concentration = 1 − 20 mgP/L; reaction time = 24 h). The composites effectively removed phosphate from real stream water. Furthermore, the composites could be regenerated and used repeatedly. The composites had chemical stability and potential for phosphate removal as adsorbents.

5. In chapter 7, Quintinite was synthesized through a co-precipitation as adsorbents for phosphate and fluoride. The maximum phosphate adsorption capacity was 4.77 mgP/g. The phosphate adsorption to quintinite was not varied at pH 3.0 − 7.1 (1.50 − 1.55 mgP/g) but decreased considerably at a highly alkaline solution (0.70 mgP/g at pH 11.0). Experimental results showed that the maximum adsorption capacity of fluoride to quintinite was 7.71 mg/g. The adsorption of fluoride to quintinite was not changed at pH 5 − 9 but decreased considerably at the highly acidic (pH < 3) and alkaline (pH > 11) solution conditions.

In this study, we assessed the applicability of the inorganic functional materials and polymer composites was assessed for removal of anion contaminants such as phosphorous, chromium, and fluorine from water and wastewater. The polymer composites synthesized in this study could be applied as adsorbents for wastewater filtration system.

8.2. Recommendations

The following recommendations are made for the future researches on polymer composites as adsorbents for anion removal from water:

1. Ion-chitosan composites have good physical strength as well as high removal capacity for phosphate in real stream water. Ion-chitosan composites can be affordable for water treatment system. Further studies are necessary to perform to examine the changes of adsorption capacity in long operating time, to evaluate reusability, to design more economic synthesis procedure.

2. Mesoporous silicas have considerable differences in the structure such as framework structure, chemical properties of the wall surface. Further studies are needed for elucidating the origin of the differences between the framework structures appearing at the Cr(VI) adsorption. The effect of the silane coupling agents have more amino groups and chains of different length scales are also needed to study.

REFERENCES

Aguado, J; Arsuaga, JM; Arencibia, A; Lindo, M; Gascon, V. 2009. Aqueous heavy metals removal by adsorption on amine-functionalized mesoporous silica. *Journal of Hazardous Materials*, 163: 213–221.

Ahmed, IM; Gasser, MS. 2012. Adsorption study of anionic reactive dye from aqueous solution to Mg–Fe–CO_3 layered double hydroxide (LDH). *Applied Surface Science*, 259: 650-656.

Akskal, O; Ucun, H. 2010. Equilibrium, kinetic and thermodynamic studies of the biosorption of textile dye (Reactive Red 195) onto Pinus sylvestris L. *Journal of Hazardous Materials*, 181: 666-672.

Aksu, Z; Gönen, F; Demircan, Z. 2002. Biosorption of chromium(VI) ions by Mowital®B30H resin immobilized activated sludge in a packed bed: comparison with granular activated carbon. *Process Biochemistry*, 38: 175–186.

Aksu, Z; Kabasakal, E. 2004. Batch adsorption of 2,4-dichlorophenoxy-acetic acid (2,4-D) from aqueous solution by granular activated carbon. *Separation and Purification Technology*, 35: 223-240.

Ansari, R. 2006. Application of polyaniline and its composites for adsorption/recovery of chromium (VI) from aqueous solutions. *Acta Chimica Slovenica*. 53: 88-94.

APHA (American Public Health Association). 1995. Standard methods for the examination of water and wastewater. Washington, DC.

Ashekuzzaman, SM; Jiang, JQ. 2014. Study on the sorption–desorption–regeneration performance of Ca-, Mg- and CaMg-based layered double hydroxides for removing phosphate from water. *Chemical Engineering Journal*, 246: 97-105.

Ayoob, S and Gupta, AK. 2006. Fluoride in drinking water: a review on the status and stress effects. *Critical Reviews in Environmental Science and Technology*, 36: 433–487.

Bajpai, SK; Armo, MK. 2009. Equilibrium sorption of hexavalent chromium from aqueous solution using iron(III)-loaded chitosan-magnetite nanocomposites

as novel sorbent. *Journal of Macromolecular Science, Part A* 46: 510-520.

Barber, TM. 2002. Phosphate adsorption by mixed and reduced iron phases in static and dynamic systems. Master's Dissertation, Stanford University, California, United States of America.

Baroni, P; Vieira, RS; Meneghetti, E; Da Silva, MGC; Beppu, MM. 2008. Evaluation of batch adsorption of chromium ions on natural and crosslinked chitosan membranes. *Journal of Hazardous Materials*, 152: 1155-1163.

Batistella, L; Venquiaruto, LD; Luccio, MD; Oliveira, JV; Pergher, SBC; Mazutti, MA; Oliveira, DD; Mossi, AJ; Treichel, H; Dallago, R. 2011. Evaluation of acid activation under the adsorption capacity of double layered hydroxides of Mg-Al-CO3 type for fluoride removal from aqueous medium. *Industrial and Engineering Chemistry Research*, 50: 6871-6876.

Benhamou, A; Basly, JP; Baudu, M; Derriche, Z; Hamacha, R. 2013. Amino-functionalized MCM-41 and MCM-48 for the removal of chromate and arsenate. *Journal of Colloid and Interface Science*, 404: 135-139.

Bhatnagar, A; Kumar, E; Sillanpää, M. 2011. Fluoride removal from water by adsorption-a review. *Chemical Engineering Journal*, 171: 811-840.

Bleiman, N and Mishael, YG. 2010. Selenium removal from drinking water by adsorption to chitosan–clay composites and oxides: Batch and columns tests. *Journal of Hazardous Materials*, 183: 590-595.

Boddu, VM; Abburi, K; Talbott, JL; Smith, ED; Haasch, R. 2008. Removal of arsenic (III) and arsenic (V) from aqueous medium using chitosan-coated biosorbent. *Water Research*, 42: 633-642.

Boyer, C; Whittaker, MR; Bulmus, V; Liu, J; Davis, TP. 2010. The design and utility of polymer-stabilized iron-oxide nanoparticles for nanomedicine applications. *NPG Asia Materials*, 2: 23-30.

Bozorgpour, F; Ramandi, HF; Jafari, P; Samadi, S; Yazd, SS; Aliabadi, M. 2016. Removal of nitrate and phosphate using chitosan/Al_2O_3/Fe_3O_4 composite nanofibrous adsorbent: Comparison with chitosan/Al_2O_3/Fe_3O_4 beads. *International Journal of Biological Macromolecules*, 93: 557-565.

Cai, P; Zheng, H; Wang, C; Ma, H; Hu, J; Pu, Y; Liang, P. 2012. Competitive adsorption characteristics of fluoride and phosphate on calcined Mg–Al–CO3 layered double hydroxides. *Journal of Hazardous Materials*, 213-214: 100-108.

Carey, CC and Rydin E. 2011. Lake trophic status can be determined by the depth distribution of sediment phosphorus. *Association for the Sciences of Limnology and Oceanography*, 56: 2051-2063.

Cavani, F; Trifirò, F; Vaccari, A. 1991. Hydrotalcite-type anionic clays: preparation, properties and applications. *Catalysis Today*, 11: 173-301.

Chen, Q; Hills, CD; Yuan, M; Liu, H; Tyrer, M. 2008. Characterization of carbonated tricalcium silicate and its sorption capacity for heavy metals: A micron-scale composite adsorbent of active silicate gel and calcite. *Journal of Hazardous Materials*, 153: 775-783.

Chang, MY; Juang, RS. 2005. Equilibrium and kinetic studies on the adsorption of surfactant, organic acids and dyes from water onto natural biopolymers. *Colloids and Surfaces A: Physicochemical and Engineering Aspects*, 269: 35-46.

Chen, L; Zhao, X; Pan, B; Zhang, W; Hua, M; Lv, L. 2015. Preferable removal of phosphate from water using water using hydrous zircornium oxide-based nanocomposite of high stability. *Journal of Hazardous Materials*, 284: 35–42.

Cheng, X; Huang, X; Wang, X; Zhao, B; Chen, A; Sun, D. 2009. Phosphate adsorption from sewage sludge filtrate using zinc-aluminum layered double hydroxides. *Journal of Hazardous Materials*, 169: 958–964.

Cheung, WH; Szeto, YS; Mckay, G. 2007. Intraparticle diffusion processes during acid dye adsorption onto chitosan. *Bioresource Technology*, 98: 2897-2904.

Chitrakar, R; Tezuka, S; Hosokawa, J; Makita, Y; Sonoda, A; Ooi, K; Hirotsu, T. 2010. Uptake properties of phosphate on a novel Zr-modified MgFe-LDH (CO3). *Journal of Colloid and Interface Science*, 349: 314-320.

Chitrakar, R; Tezuka, S; Sonoda, A; Sakane, K; Ooi, K; Hirotsu, T. 2005. Adsorption of phosphate from seawater on calcined MgMn-layered double hydroxides. *Journal of Colloid and Interface Science*, 290: 45-51.

Chowdhury, SR; Yanful, EK. 2010. Arsenic and chromium removal by mixed magnetiteemaghemite nanoparticles and the effect of phosphate on removal. *Journal of Environmental Management*, 91: 2238-2247.

Conley, DJ; Paerl, HW; Howarth, RW; Boesch, DF; Seitzinger, SP; Havens, KE; Lancelot, C; Likens, GE. 2009. Controlling eutrophication: Nitrogen and

phosphorus. *Science*, 323: 1014-1015.

Daou, TJ; Begin-Colin, S; Grenèche, JM; Thomas, F; Derory, A; Bernhardt, P; Legaré, P; Pourroy, G. 2007. Phosphate adsorption properties of magnetite-based nanoparticles. *Chemistry of materials*, 19: 4494-4505.

Das, DP; Das, J; Parida, KM. 2003. Physicochemical characterization and adsorption behavior of calcined Zn/Al hydrotalcite-like compound (HTlc) towards removal of fluoride from aqueous solution. *Journal of Colloid and Interface Science*, 261: 213-220.

Das, J; Patra, BS; Baliarsingh, N; Parida, KM. 2006. Adsorption of phosphate by layered double hydroxides in aqueous solutions. *Applied Clay Science*, 32: 252-260.

Das, NN; Konar, J; Mohanta, MK; Srivastava, SC. 2004. Adsorption of Cr(VI) and Se(IV) from their aqueous solutions onto Zr4+-substituted ZnAl/MgAl-layered double hydroxides: effect of Zr4+ substitution in the layer. *Journal of Colloid and Interface Science*, 270: 1-8.

De Vicente, I; Merino-Martos, A; Cruz-Pizarro, L; De Vicente, J. 2010. On the use of magnetic nano and microparticles for lake restoration. *Journal of Hazardous Materials*, 181: 375-381.

Del Arco, M; Gutiérrez, S; Martín, C; Rives, V; Rocha, J. 2000. Effect of the Mg:Al ratio on borate (or silicate)/nitrate exchange in hydrotalcite. *Journal of Solid State Chemistry*, 151: 272-280.

Delorme, F; Seron, A; Gautier, A; Crouzet, C. 2007. Comparison of the fluoride, arsenate and nitrate anions water depollution potential of a calcined quintinite, a layered double hydroxide compound. *Journal of Materials Science*, 42: 5799-5804.

Dey, RK; Oliveira, FJVE; Airoldi, C. 2008. Mesoporous silica functionalized with diethylenetriamine moieties for metal removal and thermodynamics of cation-basic center interactions. *Colloids and Surfaces A: Physicochem. Eng. Aspects*, 324: 41-46.

Dias, AMGC; Marcos, AHAS; Roque, ACA. 2011. A biotechnological perspective on the application of iron oxide magnetic colloids modified with polysaccharides. *Biotechnology Advances*, 29: 142-155.

Diaz-Nava, C; Solache-Rios, M; Olguin, MT. 2003. A biotechnological perspective on the application of iron oxide magnetic colloids modified with

polysaccharides. *Separation Science and Technology*, 38: 131-147.

Dindar, MH; Yaftian, MR; Rostamnia, S. 2015. Potential of functionalized SBA-15 mesoporous materials for decontamination of water solutions from Cr(VI), As(V) and Hg(II) ions. *Journal of Environmental Chemical Engineering*, 3: 968-995.

Fan, HJ; Anderson, PR. 2005. Copper and cadmium removal by Mn oxide-coated granular activated carbon. *Separation and Purification Technology*, 45: 61-67.

Fernandez, JM; Ulibarri, MA; Labajos, FM; Rives, V. 1998. The effect of iron on the crystalline phases formed upon thermal decomposition of Mg–Al–Fe hydrotalcites. *Journal of Materials Chemistry*. 8: 2507-2514.

Ferreira, OP; Alves, OL; Gouveia, DX; Filho, AGS; de Paiva, JAC; Filho, JM. Thermal decomposition and structural reconstruction effect on Mg–Fe-based hydrotalcite compounds. *Journal of Solid State Chemistry*, 177: 3058-3069.

Foo, KY; Hameed, BH. 2010. Insights into the modeling of adsorption isotherm systems. *Chemical Engineering Journal*, 156: 2–10.

Gillman, GP. 2006. A simple technology for arsenic removal from drinking water using hydrotalcite. *Science of the Total Environment*, 366: 926-931.

Goh, KH; Lim, TT; Dong, Z. 2008. Application of layered double hydroxides for removal of oxyanions: A review. *Water Research*, 42: 1343-1368.

Goswami, A; Purkait, MK. 2011. Kinetic and equilibrium study for the fluoride adsorption using pyrophyllite. *Separation Science and Technology*, 46: 1797–1807.

Gupta, A; Chauhan, VS; Sankararamakrishnan. 2009. Preparation and evaluation of iron–chitosan composites for removal of As(III) and As(V) from arsenic contaminated real life groundwater. *Water Research*, 43: 3862-3870.

Gupta, SS; Bhattacharyya, KG. 2011. Kinetics of adsorption of metal ions on inorganic materials: a review. *Advances in Colloid and Interface Science*, 162: 39–58.

Halajnia, A; Oustan, S; Najafi, N; Khataee, AR; Lakzian, A. 2013. Adsorption–desorption characteristics of nitrate, phosphate and sulfate on Mg–Al layered double hydroxide. *Applied Clay Science*, 80/81: 305-312.

Han, R; Ding, D; Xu, Y; Zou, W; Wang, Y; Li, Y; Zou, L. 2008. Use of rice husk for the adsorption of congo red from aqueous solution in column mode. *Bioresource Technology*, 99: 2938-2946.

Han, YU; Lee, CG; Park, JA; Kang, JK; Lee, I; Kim, SB. 2012. Immobilization of layered double hydroxide into polyvinyl alcohol/alginate hydrogel beads for phosphate removal. *Environmental Engineering Research*, 17:133-138.

Han, YU; Lee, WS; Lee, CG; Park, SJ; Kim, KW; Kim, SB. 2011. Entrapment of Mg-Al layered double hydroxide in calcium alginate beads for phosphate removal from aqueous solution. *Desalination and Water Treatment*, 36: 178-186.

He, H; Kang, H; Ma, S; Bai, Y; Yang, X. 2010. High adsorption selectivity of ZnAl layered double hydroxides and the calcined materials toward phosphate. *Journal of Colloid and Interface Science*, 343: 225-231.

He, JW; Xu, X; Corneille, JS; Goodman, DW. 1992. X-ray photoelectron spectroscopic characterization of ultra-thin silicon oxide films on a Mo(100) surface. *Surface Science*, 279: 119-126.

He, S. Han, C; Wang, H; Zhu, W; He, S; He, D; Luo, Y. 2015. Uptake of arsenic(Ⅴ) using alumina functionalized highly ordered mesoporous SBA-15 (Alx-SBA-15) as an effective adsorbent. *Journal of Chemical and Engineering Data*, 60: 1300-1310.

Heidari, A; Younesi, H; Mehraban, Z. 2009. Removal of Ni(Ⅱ), Cd(Ⅱ), and Pb(Ⅱ) from a ternary aqueous solution by amino functionalized mesoporous and nano mesoporous silica. *Chemical Engineering Journal*, 153: 70-79.

Herzog, F; Prasuhn, V; Spiess, E; Richner, W. 2008. Environmental cross-compliance mitigates nitrogen and phosphorus pollution from Swiss agriculture. *Environmental Science & Policy II*, 11: 655-668.

Huang, X. 2004. Intersection of isotherms for phosphate adsorption on hematite. *Journal of Colloid and Interface Science*, 271: 296-307.

Hui, B; Zhang, Y; Ye, L. 2014. Preparation of PVA hydrogel beads and adsorption mechanism for advanced phosphate removal. *Chemical Engineering Journal*, 235: 207-214.

Idris, SA; Alotaibi, KM; Peshkur, TA; Anderson, P; Morris, M; Gibson, LT. 2013. Adsorption kinetic study: Effect of adsorbent pore size distribution on the

rate of Cr(VI) uptake. *Microporous and Mesoporous Materials*, 165: 99-105.

Islam, M; Patel, R. 2009. Nitrate sorption by thermally activated Mg/Al chloride hydrotalcite-like compound. *Journal of Hazardous Materials*, 169: 524-531.

Jal, PK; Patel, S; Mishra, BK. 2004. Chemical modification of silica surface by immobilization of functional groups for extractive concentration of metal ions. *Talanta*, 62: 1005-1028.

Jiang, Y; Gao, Q; Yu, H; Chen, H; Chen, Y; Deng, F. 2007. Intensively competitive adsorption for heavy metal ions by PAMAM-SBA-15 and EDTA-PAMAM-SBA-15 inorganic-organic hybrid materials. *Microporous and Mesoporous Materials*, 103: 316-324.

Jiang, JQ and Ashekuzzaman, SM. 2012. Development of novel inorganic adsorbent for water treatment. *Current Opinion in Chemical Engineering*, 1: 191-199.

Jiang, H; Chen, P; Luo, S; Tu, X. 2013. Synthesis of novel nanocomposite Fe_3O_4/ZrO_2/chitosan and its application for removal of nitrate and phosphate. *Applied Surface Science*, 284: 942-949.

Jing, C; Cui, J; Huang, Y; Li, A. 2012. Fabrication, characterization, and application of a composite adsorbent for simultaneous removal of arsenic and fluoride. *ACS Applied Materials and Interfaces*, 4: 714-720.

Kanezaki, E. 1998. Direct observation of a metastable solid phase of Mg/Al/CO_3-layered double hydroxide by means of high temperature in situ powder XRD and DTA/TG. *Inorganic Chemistry*, 37: 2588-2590.

Kim, JH; Lee, CG; Park, JA; Kang, JK; Yoon, SY; Kim, SB. 2013. Fluoride removal using calcined Mg/Al layered double hydroxides at high fluoride concentrations. *Water Science and Technology: Water Supply*, 13: 249-256.

Kim, MK; Sundaram, KS; Lyengar, GA; Lee, KP. 2015. A novel chitosan functional gel included with multiwall carbon nanotube and substituted polyaniline as adsorbent for efficient removal of chromium ion. *Chemical Engineering Journal*, 267: 51-64.

Koilraj, P; Kannan, S. 2010. Phosphate uptake behavior of ZnAlZr ternary layered double hydroxides through surface precipitation. *Journal of Colloid and Interface Science*, 341: 289-297.

Kovanda, F; Balek, V; Dornicak, V; Martinec, P; Maslan, M; Bilkova, L;

Kolousek, D; Bountsewa, M. 2003. Thermal behavior of synthetic pyroaurite-like anionic clay. *Journal of Thermal Analysis and Calorimetry*, 71: 727-737.

Kumar, ASK; Kalidhasan, S; Rajesh, V; Rajesh, N. 2012. Application of cellulose-clay composite biosorbent toward the effective adsorption and removal of chromium from industrial wastewater. *Industrial & Engineering Chemistry Research*, 51: 58-69.

Kumar, MNVR. 2000. A review of chitin and chitosan applications. *Reactive & Functional Polymers*, 46: 1-27.

Kumari, V; Sasidharan, M; Bhaumik, A. 2014. Mesoporous $BaTiO_3$@SBA-15 derived via solid state reaction and its excellent adsorption efficiency for the removal of hexavalent chromium from water. *Dalton Transactions*, 44: 1924-1932.

Kuzawa, K; Jung ,YJ; Kiso, Y; Yamada, T; Nagai, M; Lee, TG. 2006. Phosphate removal and recovery with a synthetic hydrotalcite as an adsorbent. *Chemosphere*, 62: 45-52.

Lam, KF; Yeung, KL; Mckay, G. 2007. Selective mesoporous adsorbents for $Cr_2O_7^{2-}$ and Cu^{2+} separation. *Microporous and Mesoporous Materials*, 100: 191-201.

Lazaridis, NK; Charalambous, C. 2005. Sorptive removal of trivalent and hexavalent chromium from binary aqueous solutions by composite alginate-goethite beads. *Water Research*, 39: 4385-4396.

Lee, CG. 2014. Synthesis and application of magnetic composites for contaminant removal in aqueous solutions. Ph. D. Dissertation, Seoul National University, Seoul, Korea.

Lee, CG; Park, JA; Kim, SB. 2012. Phosphate removal from aqueous solutions using slag microspheres. *Desalination and Water Treatment*, 44: 229-236.

Lee, I; Lee, CG; Park, JA; Kang, JK; Yoon SY; Kim, SB. 2013. Removal of Cr(VI) from aqueous solution using alginate/polyvinyl alcohol–hematite composite. *Desalination and Water Treatment*, 51: 3438-3444.

Li, F. 2013. Layer-by-layer loading iron onto mesoporous silica surfaces: synthesis, characterization and application for As(V) removal. *Microporous and Mesoporous Materials*, 171: 139-146.

Li, J; Qi, T; Wang, L; Liu, C; Zhang, Y. 2007. Synthesis and characterization of imidazole-functionalized SBA-15 as an adsorbent of hexavalent chromium. *Materials Letters*, 61: 3197-3200.

Li, J; Wang, L; Qi, T; Zhou, Y; Liu, C; Chu, J; Zhang, Y. 2008. Different N-containing functional groups modified mesoporous adsorbents for Cr(VI) sequestration: synthesis, characterization and comparison. *Microporous and Mesoporous Materials*, 110: 442-450.

Li, N; Xiao, C; An, S; Hu, X. 2010. Preparation and properties of PVDF/PVA hollow fiber membranes. *Desalination*, 250: 530-537.

Liu, JQ; Xu, ZL; Li, XH; Zhang, Y; Zhou, Y; Wang, ZX; Wang, XJ. 2007. An improved process to prepare high separation performance PA/PVDF hollow fiber composite nanofiltration membranes. *Separation and Purification Technology*, 58: 53-60.

Loganathan, P; Vigneswaran, S; Kandasamy, J; Bolan, NS. 2014. Removal and recovery of phosphate from water using sorption. *Critical Reviews in Environmental Science and Technology*, 44: 847-907.

Lv, L. 2007. Deflouridation of drinking water by calcined MgAl-CO3 layered double hydroxides. *Desalination*, 208: 125-133.

Lv, L; He, J; Wei, M; Evans, DG; Zhou, Z. 2007. Treatment of high fluoride concentration water by MgAl-CO$_3$ layered double hydroxides: kinetic and equilibrium studies. *Water Research*, 41: 1534-1542.

Lv, L; He, J; Wei, M; Evans, DG; Duan X. 2006. Factors influencing the removal of fluoride form aqueous solution by calcined Mg-Al- CO3 layered double hydroxides. *Journal of Hazardous Materials B*, 133: 119–128.

Lv, X; Jiang, G; Xue, X; Wu, D; Sheng, T; Sun, C; Xu, X. 2013. Fe0-Fe3O4 nanocomposites embedded polyvinyl alcohol/sodium alginate beads for chromium (VI) removal. *Journal of Hazardous Materials*, 262: 748-758.

Ma, W; Zhao, N; Yang, G; Tian, L; Wang, R. 2011. Removal of fluoride ions from aqueous solution by the calcination product of Mg-Al-Fe hydrotalcite-like compound. *Desalination*, 268: 20-26.

Madhu, R; Maheta, NM; Pasha, TY; Patel, S. 2013. Synthesis and Antitubercular Activity of Some Novel {1[(1phenylethylidene) amino] naphtho [2,1-B]furan-2- yl}4-substituted pyrimidin-2-amine Derivatives. *International Journal of Pharmaceutical Sciences Review and Research*, 23:

72-76.

Mal, NK; Bhaumik, A; Matsukata, M; Fujiwara, M. 2006. Syntheses of mesoporous hybrid iron oxophenyl phosphate, iron oxophosphate, and sulfonated oxophenyl phosphate. *Industrial & Engineering Chemistry Research*, 45: 7748-7751.

Mandal, S; Mayadevi, S. 2008. Adsorption of fluoride ions by Zn-Al layered double hydroxides. *Applied Clay Science*, 40: 54-62.

Mandal, S; Mayadevi, S. 2009. Defluoridation of water using as-synthesized Zn/Al/Cl anionic clay adsorbent: equilibrium and regeneration studies. *Journal of Hazardous Materials*, 167: 873–878.

Marschall, R; Sharifi, M; Wark, M. 2009. Proton conductivity of imidazole functionalized ordered mesoporous silica: Influence of type of anchorage, chain length and humidity. *Microporous and Mesoporous Materials*, 123: 21-29.

McHenry, ME and Laughlin, DE. 2000. Nano-scale materials development for future magnetic applications. *Acta Materialia*, 48: 223-238.

Meng, XR; Zhao, L; Wang, L; Huang, DX. 2012. Anti-pollution behavior analysis of PVDF UF membrane added different addition to filter the secondary treated water of Urban sewage. *Advanced Materials Research*, 374/377: 1076-1080.

Miretzky, P; Cirelli, AF. 2009. Hg(II) removal from water by chitosan and chitosan derivatives: A review. *Journal of Hazardous Materials*, 167: 10-23.

Mirji, SA; Halligudi, SB; Mathew, N; Jacob, N; Patil, KR; Gaikwad, AB. 2007. Adsorption of methanol on mesoporous SBA-15. *Materials Letters*, 61: 88-92.

Mittal, N; Samanta, A; Sarkar, P; Gupta, R. 2015. Postcombustion CO_2 capture using N-(3-trimethoxysilylpropyl)diethylenetriamine-grafted solid adsorbent. *Energy Science & Engineering*, 3: 207-220.

Mohai, M; Bertoti, I; Revesz, M. 1990. XPS study of the state of oxygen on a chemically treated glass surface. *Surface and Interface Analysis*, 15: 364-368.

Mohapatra, M; Anand, S; Mishra, BK; Giles, DE; Singh, P. 2009. Review of fluoride removal from drinking water. J*ournal of Environmental Management*,

91: 67-77.

Mohseni-Bandpi, A; Kakavandi, B; Kalantary, RR; Azari, A; Keramati, A. 2015. Development of a novel magnetite–chitosan composite for the removal of fluoride from drinking water: adsorption modeling and optimization. *Royan Society of Chemistry Advances*, 5: 73279-73289.

Morse, GK; Brett, SW; Guy, JA; Lester, JN. 1998. Review: Phosphorus removal and recovery technologies. *The Science of the Total Environment*, 212: 69-81.

Nayak, D; Banerjee, A; Roy, S; Lahiri, S. 2006. Speciation dependent studies on chromium absorption using calcium alginate and iron doped calcium alginate biopolymer. *Journal of Radioanalytical and Nuclear Chemistry*, 274: 219-224.

Nomanbhay, SM and Palanisamy, K. 2005. Removal of heavy metal from industrial wastewater using chitosan coated oil palm shell charcoal. *Electronic Journal of Biotechnology*, 8: 43-53.

OECD (Organization for Economic Co-operation and Development). 1982. Eutrophication of waters: Monitoring, assessment, and control. Paris, France.

Park, JA; Lee, CG; Kim, JH; Kang, JK; Lee, I; Kim, SB. 2011. Removal of bacteriophage MS2 from aqueous solution using Mg-Fe layered double hydroxides. *Journal of Environmental Science and Health, Part A*, 46: 1683-1689.

Police, AKR; Basavaraju, S; Valluri, D; Machiraju, S. 2015. Photocatalytic activity of Ce-modified SBA-15 for the degradation of isoproturon. 38: *Bulletin of Materials Science*, 38: 227-234.

Ren, Y; Yan, N; Wen, Q; Fan, Z; Wei, T; Zhang, M; Ma, J. 2011. Graphene/δ-MnO2 composite as adsorbent for the removal of nickel ions from wastewater. *Chemical Engineering Journal*, 175: 1-7.

Richard, FC and Bourg, ACM. 1991. Aqueous geochemistry of chromium: a review. *Water research*, 25: 807-816.

Saber-Samandari, S; Saber-Samandari, S; Nezafati, N; Yahya, K. 2014. Efficient removal of lead (II) ions and methylene blue from aqueous solution using chitosan/Fe-hydroxyapatite nanocomposite beads. *Journal of Environmental Management*, 146: 481-490.

Saleh, TA; Gupta, VK. 2012. Column with CNT/magnesium oxide composite for lead(II) removal from water. *Environmental Science and Pollution Research*, 19: 1224-1228.

Sasai, R; Norimatsu, W; Matsumoto, Y. 2012. Nitrate-ion-selective exchange ability of layered double hydroxide consisting of Mg^{II} and Fe^{III}. *Journal of Hazardous Materials*, 215-216: 311-314.

Sayari, A; Hamoudi, S; Yang, Y. 2005. Applications of pore-expanded mesoporous silica. 1. Removal of heavy metal cations and organic pollutants from wastewater. *Chemistry of Materials*, 17: 212-216.

Seida, Y; Nakano, Y. 2002. Removal of phosphate by layered double hydroxides containing iron. *Water Research*, 36: 1306-1312.

Shahbazi, A; Younesi, H; Badiei, A. 2011. Functionalized SBA-15 mesoporous silica by melamine-based dendrimer amines for adsorptive characteristics of Pb(II), Cu(II) and Cd(II) heavy metal ions in batch and fixed bed column. *Chemical Engineering Journal*, 168: 505-518.

Sharma, SK; Petrusevski, B; Amy, G. 2008, Chromium removal from water: a review. *Journal of Water Supply: Research and Technology-AQUA*, 57: 541-553.

Shi, ZL; Liu, F; Yao, S. 2011. Adsorptive removal of phosphate from aqueous solutions using activated carbon loaded with Fe(III) oxide. *New Carbon Materials*, 26: 299-306.

Srinivasan, R. 2011. Advances in application of Natural clay and its composites in removal of biological, organic, and inorganic contaminants from drinking water. *Advances in Materials Science and Engineering*, 2011: 1-17.

Stavropoulos, GG; Papadopoulou, M; Papadimitriou, K. 2016. A kinetic and thermodynamic study of cyanide adsorption in activated carbon. *Desalination and Water Treatment*, 57: 21939–21943.

Stegall, SL; Ashraf, KM; Moye JR; Higgins, DA; Collinson, MM. 2016. Separation of transition and heavy metals using stationary phase gradients and thin layer chromatography. *Journal of Chromatography A*, 1446: 141-148.

Sun, X; Peng, B; Ji, Y; Chen, J; Li, D. 2009. Chitosan(chitin)/cellulose composite biosorbents prepared using ionic liquid for heavy metal ions

adsorption. *American Institute of Chemical Engineers*, 55: 2062-2069.

Sun, Y; Yue, Q; Gao, B; Gao, Y; Li, Q; Wang, Y. 2013. Adsorption of hexavalent chromium on Arundo donax Linn activated carbon amine-crosslinked copolymer. *Chemical Engineering Journal*, 217: 240-247.

Taha, AA; Qiao, J; Li, F; Zhang, B. 2012. Preparation and application of amino functionalized mesoporous nanofiber membrane via electrospinning for adsorption of Cr^{3+} from aqueous solution. *Journal of Environmental Sciences*, 24: 610-616.

Tan, IAW; Hameed, BH; Ahmad, AL. 2007. Equilibrium and kinetic studies on basic dye adsorption by oil palm fibre activated carbon. *Chemical Engineering Journal*, 127: 111-119.

Triantafyllidis, KS; Peleka, EN; Komvokis, VG; Mavros, PP. 2010. Iron-modified hydrotalcite-like materials as highly efficient phosphate sorbents. *Journal of Colloid and Interface Science*, 342: 427-436.

Viswanathan, N; Sundaram, CS; Meenakshi, S. 2009. Removal of fluoride from aqueous solution using protonated chitosan beads. *Journal of Hazardous Materials*, 161: 423-430.

Wang, H; Chen, J; Cai, Y; Ji, J; Liu L; Teng HH. 2007. Defluoridation of drinking water by Mg/Al hydrotalcite-like compounds and their calcined products. *Applied Clay Science*, 35: 59-66.

Wang, L and Wang A. 2007. Adsorption characteristics of Congo Red onto the chitosan/montmorillonite nanocomposite. *Journal of Hazardous Materials*, 147: 979-985.

Wang, Y; Han, T; Xu, Z; Bao, G; Zhu, T. 2005. Optimization of phosphorus removal from secondary effluent using simplex method in Tianjin, China. *Journal of Hazardous Materials*, 212: 183-186.

Weber, WJ and Morris, JC. 1963. Kinetics of adsorption on carbon from solution. *Journal of the Sanitary Engineering Division*, 89: 31-60.

Wu, Q; You, R; Lv, Q; Xu, Y; You, W; Yu, Y. 2015. Efficient simultaneous removal of Cu(II) and $Cr_2O_7^{2-}$ from aqueous solution by a renewable amphoteric functionalized mesoporous silica. *Chemical Engineering Journal*, 281: 491-501.

Wu, Y; Zhou, J; Jin, Y; Cao, J; Yilihan, P; Wen, Y; Wu, Y. 2014. Mechanisms of

chromium and arsenite adsorption by amino-functionalized SBA-15. *Environmental Science and Pollution Research*, 21: 1859–1874.

Xiong, J; He, Z; Mahmmod, Q; Liu, D; Yang, X; Islam, E. 2008. Phosphate removal from solution using steel slag through magnetic separation. *Journal of Hazardous Materials*, 152: 211-215.

Xu, P; Zeng, GM; Huang, DL; Feng, CL; Hu, S; Zhao, MH; Lai, C; Wei, Z; Huang, C; Xie, GX; Liu, ZF. 2012. Use of iron oxide nanomaterials in wastewater treatment: A review. *Science of the Total Environment*, 424: 1-10.

Xu, X; Gao, B; Wang, W; Yue, Q, Wang, Y; Ni, S. 2009. Adsorption of phosphate from aqueous solutions onto modified wheat residue: characteristics, kinetic and column studies. *Colloids and Surfaces B: Biointerfaces*, 70: 46-52.

Yang, K; Yan, LG; Yang, YM; Yu, SJ; Shan, RR; Yu, HQ; Zhu, BC; Du, B. 2014. Adsorptive removal of phosphate by Mg-Al and Zn-Al layered double hydroxides: kinetics, isotherms and mechanisms. *Separation and Purification Technology*, 124: 36-42.

Yao, S; Li, J; Shi, Z. 2009. Phosphate ion removal from aqueous solution using an iron oxide-coated fly ash adsorbent. *Adsorption Science & Technology*, 27: 603:614.

Yoon, SY. 2014. Magnetic zeolite-polymer composites for Cu(II) and Cr(III) removal from aqueous solutions. Master's Dissertation, Seoul National University, Seoul, Korea.

Yoshitake, H; Yokoi, T; Tatsumi, T. 2002a. Capture of chromate and arsenate by amino groups in functionalised SBA-1. *Chemistry Letters*. 6: 586-587.

Yoshitake, H; Yokoi, T; Tatsumi, T. 2002b. Adsorption of chromate and arsenate by amino-functionalized MCM-41 and SBA-1. *Chemistry of Materials*, 14: 4603-4610.

Yoshitake, H; Yokoi, T; Tatsumi, T. 2003. Adsorption behavior of arsenate at transition metal cations captured by amino-functionalized mesoporous silicas. *Chemistry of Materials*, 15: 1713-1721.

Yoshitake, H; Koiso, E; Horie, H; Yoshimura, H. 2005. Polyamine-functionalized mesoporous silicas: Preparation, structural analysis and oxyanion adsorption. *Microporous and Mesoporous Materials*, 85: 183-194.

Yu, CH; Al-Saadi, A; Shih, SJ; Qiu, L; Tam, KY; Tsang, SC. 2009. Immobilization

of BSA on silica-coated magnetic iron oxide nanoparticle. *The Journal of Physical Chemistry C*, 113: 537-543.

Yu, Y; Y, L; Chen, P. 2015. Adsorption of fluoride by Fe-Mg-La triple-metal composite: absorbent preparation, illustration of performance and study of mechanisms. *Chemical Engineering Journal*, 262: 839-846.

Zhang, L; Hong, S; He, J; Gan, F; Ho, YS. 2011. Adsorption characteristic studies of phosphorus onto laterite. *Desalination and Water Treatment*, 25: 98-105.

Zhang, L; Yu, C; Zhao, W; Hua, Z; Chen, H; Li, L; Shi. J. 2007. Preparation of multi-amine-grafted mesoporous silicas and their application to heavy metal ions adsorption. *Journal of Non-Crystalline Solids*, 353: 4055-4061.

Zhang, M; Gao, B; Yao, Y; Inyang, M. 2013. Phosphate removal ability of biochar/MgAl-LDH ultra-fine composites prepared by liquid-phase deposition. *Chemosphere*, 92: 1042-1047.

Zhang, X; Wang, Y; Liu, Y; Xu, J; Han, Y; Xu, X. 2014. Preparation, performances of PVDF/ZnO hybrid membranes and their applications in the removal of copper ions. *Applied Surface Science*, 316: 333-340.

Zhao, D; Huo, Q; Feng, J; Chmelka, BF; Stucky, GD. 1998. Nonionic triblock and star diblock copolymer and oligomeric surfactant syntheses of highly ordered, hydrothermally stable, mesoporous silica structures. *Journal of the American Chemical Society*, 120: 6024-6036.

Zhao, XS; Lu, GQ; Whittaker, AK; Millar, GJ; Zhu, HY. 1997. Comprehensive study of surface chemistry of MCM-41 using Si CP/MAS NMR, FTIR, Pyridine-TPD, and TGA. *The Journal of Physical Chemistry B*, 101: 6525–6531.

Zheng, YM; Zou, SW; Nanayakkara, KGN; Matsuura, T; Chen, JP. 2011. Adsorptive removal of arsenic from aqueous solution by a PVDF/zirconia blend flat sheet membrane. *Journal of Membrane Science*, 374: 1-11.

Zhou, J; Cheng, Y; Yu, J; Liu, G. 2011. Hierarchically porous calcined lithium/aluminum layered double hydroxides: Facile synthesis and enhanced adsorption towards fluoride in water. *Journal of Materials Chemistry*, 21: 19353-19361.

Zhu, Z; Zeng, H; Zhu, Y; Yang, F; Zhu, H; Qin, H; Wei, W. 2013. Kinetics and thermodynamic study of phosphate adsorption on the porous biomorph-

genetic composite of a-Fe_2O_3/Fe_3O_4/C with eucalyptus wood microstructure. *Separation and Purification Technology*, 117: 124-130.

Zouboulis, AI and Katsoyiannis, IA. 2002. Arsenic removal using iron oxide loaded alginate beads. *Industrial & Engineering Chemistry Research*, 41: 6149-6155.

국문 초록

본 논문에서는 기능성 무기소재 및 고분자 복합체를 제조하여 특성을 분석하는 한편, 인, 크롬, 불소 등 수중 음이온 오염물질에 대한 제거능을 평가하고 흡착제로서 적용 가능성을 살펴보고자 하였다. 제조된 기능성 무기소재 및 고분자 복합체는 전계방사형 주사전자현미경 (FESEM), 에너지 분산형 X-선 분광기 (EDS), 투과전자현미경 (TEM), 푸리에 변환 적외선 분광기 (FT-IR), X-선 회절 분석기 (XRD), 그리고 X-선 광전자 분광기 (XPS) 등 다양한 분석기술을 통해 분석하였다.

ION-chitosan 복합체는 철산화물 나노입자 (Iron oxide nanoparticle, ION)를 합성하고 이를 친환경적 고분자인 키토산에 첨가하여 제조하였다. 현장원수를 이용한 실내에서의 배치실험 및 칼럼실험을 수행하여 수중 인 제거 특성을 평가하였으며, 재이용 실험을 통해 6회의 재이용 시에도 인 흡착능이 꾸준히 유지되는 것을 확인하였다. 파일럿 규모의 흡착탑을 이용한 현장실험을 통해 부영양화 기준농도인 0.035 mg/L 이하로 수중 인을 제거할 수 있음을 확인하였으며, 33일 동안 흡착능을 유지하면서 수중 환경 변화에는 영향을 거의 미치지 않음을 확인하였다. 이를 통해 인 흡착제로서 현장 적용 가능성을 확인하였다.

259

Triamine-functionalized 메조다공성 실리카 복합체는 먼저 메조다공성 실리카 SBA-15를 합성하고, 트리아민을 이용하여 표면을 기능화한 뒤 PVA 및 alginate를 지지체로 하여 제조하였다. 표면을 개질한 메조다공성 실리카는 수중의 6가 크롬을 빠르게 제거하였으며, 330.88 mg/g의 최대흡착능을 나타내었다. 또한 도금폐수를 이용한 실험을 수행하여 크롬에 대한 제거능과 복합체의 안정성을 확인하였으며, 이를 통해 실제 공장폐수에 대한 triamine-functionalized 메조다공성 실리카 복합체의 적용 가능성을 확인하였다.

Mg-Fe CLDH는 공침전법으로 Mg-Fe 층상이중수산화물(layered double hydroxide, LDH)을 합성한 뒤 300 ℃로 열처리하여 제조하였으며, 배치실험과 모델 분석을 수행하여 수중 인 제거 특성을 평가하였다. 또한 0.1M NaOH 용액을 이용하여 인을 탈착시킴으로써 재이용이 가능함을 확인하였다.

MgFe CLDH 고분자 복합체는 Mg-Fe CLDH와 화학적, 열적 안정성이 우수한 PVDF 및 친수성이 뛰어난 PVA를 이용하여 제조하였으며, 현장원수를 이용한 배치실험과 칼럼실험을 수행하여 인 흡착능을 평가하였다. MgFe CLDH 고분자 복합체는 산성 및 염기성의 pH 조건에서도 흡착능이 유지되었으며, 재이용 실험을 통해 3회의 재이용 시에도 흡착능을 유지함을 확인하였다.

층상이중수산화물 계열의 일종인 퀸티나이트 (quintinite)는 공침법을 이용하여 합성하였으며, 흡착제로서 수중 인과 불소에 대한 제거능을 평가하였다. 인에 대해서는 4.77 mg/g의 최대흡착능을 나타내었으며, pH 11의 염기성 조건에서 흡착능이 감소하였다. 또한 현장원수를 이용한 실험에서는 공존하는 음이온과의 경쟁으로 인해 인에 대한 흡착능이 감소하였다. 불소에 대해서는 7.71 mg/g의 최대흡착능을 나타내었고 pH 3 이하의 산성 조건과 pH 9 이상의 염기성 조건에서 흡착능이 감소함을 확인하였다.

본 연구에서는 다양한 실험들을 통해 기능성 무기소재 및 고분자 복합체들의 수중 음이온 오염물질 제거특성을 평가하였다. 또한 개발된 고분자 복합체들의 수처리 시스템에 대한 적용 가능성을 확인할 수 있었다. 본 연구 결과를 통해 기능성 고분자 복합체의 제조 및 이를 활용한 수처리 분야에서의 연구를 위한 기초 자료를 제공할 수 있을 것으로 기대된다.